BRNO UNIVERSITY OF TECHNOLOGY

VYSOKÉ UČENÍ TECHNICKÉ V BRNĚ

FACULTY OF MECHANICAL ENGINEERING

FAKULTA STROJNÍHO INŽENÝRSTVÍ

INSTITUTE OF MATERIALS SCIENCE AND ENGINEERING

ÚSTAV MATERIÁLOVÝCH VĚD A INŽENÝRSTVÍ

TENSION – COMPRESSION ASYMMETRY NON-FEROUS ALLOYS

ASYMETRICKÁ ODEZVA NA TAHOVÉ A TLAKOVÉ ZATĚŽOVÁNÍ NEŽELEZNÝCH KOVŮ

BACHELOR'S THESIS

BAKALÁŘSKÁ PRÁCE

AUTHOR — Martin Čavojec

AUTOR PRÁCE

SUPERVISOR — Ing. Josef Zapletal, Ph.D.

VEDOUCÍ PRÁCE

BRNO 2020

BRNO UNIVERSITY OF TECHNOLOGY
FACULTY OF MECHANICAL ENGINEERING

Specification Bachelor's Thesis

Department:	Institute of Materials Science and Engineering
Student:	**Martin Čavojec**
Study programme:	Applied Sciences in Engineering
Study branch:	Materials Engineering
Supervisor:	**Ing. Josef Zapletal, Ph.D.**
Academic year:	2019/20

Pursuant to Act no. 111/1998 concerning universities and the BUT study and examination rules, you have been assigned the following topic by the institute director Bachelor's Thesis:

Tension – compression asymetry non–ferous alloys

Concise characteristic of the task:

For a comprehensive understanding of the properties of materials, it is necessary to determine the response of materials to compressive loading and use the appropriate parameters to relate it to the tensile response (TCA parameter), or describe it as a function of the orientation of texture of the test specimens. Significant difference in response can be expected in materials with significant directionality of the structure (forming, bimodality in ECAP, extrusion).

Goals Bachelor's Thesis:

1. Basic principles.
2. A literature review of experimental determination of response to tensile and compressive loading.
3. A literature review of possible description of tension–compression asymmetry as a function of orientation and texture.
4. Experimental determination of tensile and compressive response on specific non–ferrous alloy and determination of tension–compression asymmetry as a function of directionality of the structure.

Recommended bibliography:

ČSN EN ISO 6892-1. Kovové materiály - Zkoušení tahem - Část 1: Zkušební metoda za pokojové teploty. Praha: ÚNMZ, 2017.

ASTM E9-89. Standard Test Methods of Compression Testing of Metallic Materials at Room Temperature. ASTM International, West Conshohocken, PA, 2000.

TONG, L. B., M. Y. ZHENG, X. S. HU, K. WU, S. W. XU, S. KAMADO and Y. KOJIMA. Influence of ECAP routes on microstructure and mechanical properties of Mg–Zn–Ca alloy. Materials Science and Engineering: A [online]. 2010, 527(16-17), 4250-4256 [cit. 2018-11-14]. DOI: 10.1016/j.msea.2010.03.062. ISSN 09215093. Dostupné z: http://linkinghub.elsevier.com/retrieve/pii/S0921509310003369

XU, S., T. LIU, H. CHEN, Z. MIAO, Z. ZHANG and W. ZENG. Reducing the tension–compression yield asymmetry in a hot-rolled Mg–3Al–1Zn alloy via multidirectional pre-compression. Materials Science and Engineering: A [online]. 2013, 565, 96-101 [cit. 2018-11-14]. DOI: 10.1016/j.msea.2012.11.127. ISSN 09215093. Dostupné z: https://linkinghub.elsevier.com/retrieve/pii/S0921509312017182

YIN, D. L., J. T. WANG, J. Q. LIU and X. ZHAO. On tension–compression yield asymmetry in an extruded Mg–3Al–1Zn alloy. Journal of Alloys and Compounds [online]. 2009, 478(1-2), 789-795 [cit. 2018-11-14]. DOI: 10.1016/j.jallcom.2008.12.033. ISSN 09258388. Dostupné z: http://linkinghub.elsevier.com/retrieve/pii/S0925838808022056

Deadline for submission Bachelor's Thesis is given by the Schedule of the Academic year 2019/20

In Brno,

L. S.

prof. Ing. Ivo Dlouhý, CSc.
Director of the Institute

doc. Ing. Jaroslav Katolický, Ph.D.
FME dean

ABSTRACT

The Bachelor thesis focuses on asymmetric response to tensile and compressive loading of nonferrous metals, namely magnesium alloys. It describes basic principles of tensile and compressive testing; it expands on experimental determination of asymmetric response to tensile and compressive loading, influence of various parameters on tension-compression asymmetry, and possible description of asymmetry as a function of orientation and texture

Towards the end, this thesis describes experimental determination and evaluation of asymmetric response to tensile and compressive loading of magnesium alloy AZ61, with metallographic analysis of this alloy.

KEYWORDS

nonferrous metals, magnesium alloys, extruded materials, tension testing, compression testing, stress-strain curve, tension-compression asymmetry, tension-compression asymmetry parameter, CYS/TYS, grain size, texture, load direction

ABSTRAKT

Bakalářská práce se zabývá asymetrickou odezvou na tahové a tlakové zatěžování neželezných kovů, jmenovitě hořčíkových slitin. Popisuje základní problematiku zkoušek tahem a tlakem, experimentální stanovením asymetrické odezvy, vliv rozličných parametrů na asymetrickou odezvu na tahové a tlakové zatěžování, a také možný popis asymetrie jako funkci orientace a textury.

Na závěr práce popisuje experimentální stanovení a vyhodnocení asymetrické odezvy na tlakové a tahové zatěžování hořčíkové slitiny AZ61, s metalografickou analýzu tyto slitiny.

KLÍČOVÁ SLOVA

neželezné kovy, hořčíkové slitiny, extrudované materiály, zkouška tahem, zkouška tlakem, tahový diagram, tahová-tlaková asymetrie, parametr tahové-tlakové asymetrie, CYS/TYS, velikost zrna, textura, směr zatěžování

ROSŠÍŘENÝ ABSTRAKT

Slitiny neželezných kovů, co znamená všechny slitiny neobsahující železo ve značné míře jako přísadový prvek, jsou navzdory vyšší ceně přípravy a produkce široce vyhledávány a používaný v technické a industriální praxi díky svým příznivým specifickým vlastnostem. Jako například nízká hustota (hliník), vyšší elektrická a tepelná vodivost (měď, stříbro a zlato), relativně výhodný podíl hmotnosti a pevnosti (hořčík), odolnost vůči korozi (zinek) atd. I když celosvětová produkce a spotřeba slitin neželezných kovů činí jen 5 %, slitiny na bázi železa činí zbylých 95 %, využití, technologické a industriální aplikace slitin neželezných kovů jsou nesmírně důležité.

Hořčík, kov s hustotou jen ρ=1,740 g/cm^3 krystalizuje při teplotě 650 °C do HCP mřížky, která je častou příčinou anizotropie některých mechanických a fyzikálních vlastností u čistého hořčíku. Proto se především v technické and konstrukční praxi používají hořčíkové slitiny. Nejčastější legující prvky jsou hliník, zinek, mangan, zirkonium a křemík. Výhodou použití hořčíkových slitin jsou jejich nízká hustota, vysoká specifická pevnost, dobrá obrobitelnost a dobrá schopnost tlumení vibrací. Naopak nevýhodou jsou nízká tvářitelnost při nízkých teplotách, nízká difuzivita při tepelném zpracování, náročnější a tím pádem i nákladnější příprava a výroba, z důvodu vysoké reaktivity hořčíku při zvýšených teplotách. Jelikož hořčíkové slitiny mají malou tvářitelnost, slitiny pro lití jsou upřednostňovány oproti tvářeným litinám. Avšak žádný významný rozdíl mezi chemickým složením litých a tvářených slitin neexistuje.

Zkouška tahem jako jedna z nejzákladnějších mechanických zkoušek, dokáže pomocí destruktivního zkoušení určit mez kluzu, mez pevnosti v tahu, modul pružnosti, tažnost jakéhokoli zkoušeného materiálu. Pro provádění zkoušek jsou používány dva typy strojů, a to mechanické a hydraulické. Samotný princip zkoušky a zkoušecích zařízení zůstává nezměněn.

Zkouška je založena na principu zaznamenávání tahového diagramu, jakou funkci odporu zkoušených vzorků proti deformaci a poškození. Výsledky zkoušky bývají zaznamenávány do skutečného tahového diagram, který se používá při výpočtech pevnostních charakteristik součástek, zatímco smluvní diagram se používá pro odhad chování materiálu při zatížení, a pro zjišťování pevnostních charakteristik materiálů.

První část diagramu je lineární, elastická deformace, a podléhá Hookovu zákonu, z kterého se zjišťuje modul pružnosti. Další část diagramu tuto linearitu ztrácí, z důvodu rovnoměrné plastické deformace, až do bodu meze pevnosti. Od tohoto bodu se těleso začne deformovat nerovnoměrně, tvoří se krček, a klesá napětí. Toto je zakončeno přetržením testovacího tělesa.

Napěťové charakteristiky, které zjišťujeme z tahového digramu jsou modul pružnosti, mez úměrnosti, mez pružnosti, mez kluzu, mez pevnosti a napětí při porušení zkušebního tělesa. Další specifická napěťová charakteristika je smluvní mez kluzu, která se určuje z důvodu možné nepřesnosti při měření meze kluzu. Za hodnotu smluvní meze kluzu se považuje napětí, při kterém se dosáhne plastické deformace $\varepsilon = 0{,}002$.

Deformační charakteristiky, které se zjišťují ze zkoušky jsou tažnost a kontrakce. Deformační charakteristiky se určují z rozměrů zkušebních těles pře a po provedení zkoušky v nezatíženém stavu. Výskyt největší tažnosti v houževnatých materiálech je v oblasti krčku, který se začne tvoři na mezi pevnosti až do porušení.

Zkušební tělesa, jejich geometrie, rozměry a povrchová úprava, jsou zpravidla normalizované. Mají svůj charakteristický průřez s obsahem S_0 a charakteristickou délkou L_0. Tělesa se většinou získávají obráběním součásti, komponentu, nebo odlitku určeného pro testování. Využívaní miniaturních vzorků při zkoušce umožňuje použití co nejmenšího množství materiál ze součástí a komponentů, které jsou pořád používány, avšak jejich použití sebou přináší řadu komplikací. Nicméně geometrie ani rozměry miniaturních zkušebních těles nebyli prozatím normalizovány.

Tlaková zkouška je založena na podobných principech jako zkouška tahová, ale liší se ve smyslu působící síly. Používá stejné zkoušecí zařízení jako u tahové zkoušky, ale upínací čelisti jsou vyměněny za podložky. Jako zkušební tělesa se používají jednoduché válečky s normalizovanými rozměry S_0 plocha průřezu zkušebního tělesa a H_0 výška zkušebního tělesa, a přesně definovaným poměrem mezi S_0 a H_0. Podobně jako u zkoušky tahem deformace zkušebních těles se měří přesnými tensometry. Výsledkem podobně jako u tahové zkoušky je diagram závislosti napětí a deformace.

Bauschingerův efekt popisuje fenomén, při kterém materiál vykazuje značnou asymetrickou odezvu při kombinované tahovém a tlakovém zatěžování. Je popsán a definován třemi parametry, napěťovým, deformačním a energetickým. Mechanismy Bauschingerova efektu jsou založeny na dvou základních teoriích. A to teorie vnitřního napětí a Orowanova teorie (backstress theory) také známa pod názvem teorie dislokací.

Druhý úsek rešeršní části se zabývá asymetrickou odezvou na tahové a tlakové zatěžování u hořčíkových slitin. Jelikož přítomnost asymetrické odezvy na tahové a tlakové zatěžování v hořčíkových slitinách byla v minulosti už důkladně studována a řady výzkumů a studií se snažili objasnili příčinu vzniku asymetrické odezvy a její možné odstranění, práce se proto zabývá těmato studiemi a jejími výsledky a poznatky.

Přítomnost asymetrické odezvy je hlavně způsobená komplikovaným deformačním chováním HCP mřížky. Přítomnost řady deformačních textur, zejména dvojčat při ztěžování má za následek změnu odezvy na tahové nebo tlakové zatěžování. Asymetrická odezva je popsaná poměrem CYS/TYS, co je poměr mezi mezí kluzu v tlaku (CYS) a mezí kluzu v tahu (TYS), známy taky pod názvem TCA parametr. Tento parametr popisuje rozsah asymetrické odezvy. Jestli se TCA parametr rovná jedné, asymetrie v materiálu není přítomná.

Z vyšetřování vlivu orientace a směrovosti zrna, které bylo zkoumáno pomocí změny úhlů zatěžování pro 0°, 45° 90°, při konstantní velikosti zrna, vyplynulo že geometrické podmínky a proces dvojčatění mají velký vliv na přítomnost a rozsah asymetrické odezvy. To bylo potvrzeno metalografickou analýzou, která potvrdila závislost změny struktury a dvojčatění na směru zatěžování. Dále byla potvrzena závislost rozsahu asymetrické odezvy na velikosti zrna, která byla zkoumána pomocí vzorků s různými rozměry zrn. Nakonec zkoumáním, jak přispívá dvojčatění k asymetrické odezvě ukázalo, že kombinovaný efekt směru zatěžování a velikosti zrna má podstatný vliv na odezvu v tlakovém zatěžování.

Vyšetřování vlivu různých protlačovacích procesů na rozsah asymetrické odezvy poukázalo na velký rozdíl v asymetrické odezvě na tahové a tlakové zatěžování pro nepřímé a hydrostatické extrudování. Hydrostatické extrudování dosáhlo rozdíl mezi mezí kluzu v tlaku a tahu, jen ~12 MPa, zatímco nepřímé extrudování dosáhlo rozdílu ~100MPa. Co bylo pravděpodobně zapříčiněno potlačením příspěvku dvojčatění jako deformační

struktury pomocí jemnozrnné struktury v případě hydrostaticky extrudovaných vzorků. Testy taky dále naznačili, že nejen velikost zrna ale i precipitace intermetalických fázi, zejména $Mg_{17}Al_{12}$, má vliv na proces dvojčatění.

Zkoumání efektu více směrové před-deformace na hořčíkové slitiny odhalilo, že před-deformované a nežíhané vzorky vykazovali velké množství tahové-tlakové asymetrie na rozdíl od vzorků, které byli před-deformované a vyžíhané. Což dokazuje, že před-deformace s následným žíháním dokáže do jisté míry zmenšit asymetrickou odezvu. Analýza metalografických vzorků odhalila přítomnost prodlužovacího dvojčatění v před-deformovaných a žíhaných vzorcích.

Zkoumáni vlivu teploty zkoušení a stupně zatěžování na přítomnost a rozsah asymetrické odezvy odhalilo výskyt asymetrie, která je citlivá na teplotu zkoušení i stupeň zatěžování a taktéž i na většinu jejich kombinací. Metalografická analýza dále odhalila že při kritické teplotě $\sim 250°C$ se objevují $\{1\ 0\ \bar{1}\ 2\}$ dvojčata v kombinací s bazálním skluzem v tahu a $\{1\ 0\ \bar{1}\ 2\}$ dvojčata v tlaku, co způsobuje značně rozdílnou mikrostrukturu. Tyto deformační mechanismy způsobují významnou asymetrickou odezvu pod kritickou teplotou $\sim 250°C$, ztímco nad touto teplotou proběhly značné rekrystalizační procesy, které asymetrickou odezvu téměř úplně odstranili.

V experimentální části se pak dále zkoumala přítomnost asymetrické odezvy na tahové a tlakové zatěžování v hořčíkové slitině AZ61, extrudované při teplotě 300°C. Podezření na přítomnost asymetrické odezvy se potvrdilo, s hodnotou TCA parametru CYS/TYS=0,69, co se dá považovat za značnou asymetrickou odezvu. Metalografický analýza dále odhalila rozdílnou velikost zrna na okraji a ve středu vzorku. Směrovost byla do jisté míry patrná z makroskopického uspořádání a rozložení zrna a precipitátů, ale tvar samotných zrn žádnou směrovost nenaznačoval. Další určovaní směrovosti textury by se mohlo uskutečnit pomocí EBSD analýzy, avšak kvůli nepředvídaným komplikacím a současné situaci to nebylo uskutečněno. Přítomnost asymetrické odezvy v AZ61 hořčíkové slitině mohla být zapříčiněna rozdílnou velikostí zrna, přítomností precipitátů na hranicích zrn a procesem dvojčatění aktivovaném během zatěžování.

Bibliographic citation

ČAVOJEC, Martin. *Asymetrická odezva na tahové a tlakové zatěžování neželezných kovů.* Brno, 2020. Dostupné také z: https://www.vutbr.cz/studenti/zav-prace/detail/121470. Bakalářská práce. Vysoké učení technické v Brně, Fakulta strojního inženýrství, Ústav materiálových věd a inženýrství. Vedoucí práce Josef Zapletal.

DECLARATION

I declare that the bachelor's thesis Tension-compression asymmetry of non-ferrous alloys was written on my own, according to the goals set by the supervisor Ing. Josef Zapletal, Ph.D., using literature sources listed in references.

26.06.2020 in Brno Čavojec Martin

AKNOWLEGMENT

I would like to thank my supervisor Ing. Josef Zapletal, Ph.D. for his advice, supervision and patience while writing this thesis. Furthermore, I would like to thank Ing. Roman Štěpánek, Ph.D. for his help in preparation of metallographic samples.

Contents

1 Introduction 1

2 Non-ferrous metals 2

2.1 Magnesium 2

2.1.1 Magnesium alloys 3

3 Tensile testing 5

3.1 Tensile testing machines 5

3.2 Stress-strain diagram 5

3.3 Stress characteristics 7

3.4 Strain characteristics 9

3.5 Strain rate 10

3.6 Strain hardening 11

3.7 Test specimens 12

3.7.1 Standardized dimensions 13

3.7.2 Miniature test specimens 14

4 Compressive testing 15

4.1 Test specimens 16

4.2 Stability and buckling 17

5 Tension-compression asymmetry 19

5.1 Bauschinger effect 19

5.1.1 Bauschinger effect parameters 19

5.1.1.1 Stress parameter 19

5.1.1.2 Strain parameter 20

5.1.1.3 Energy parameter 20

5.1.2 Causes of the Bauschinger effect 20

5.1.2.1 Internal stress theory 21

5.1.2.2 Orowan theory 21

5.2 Tension-compression asymmetry in magnesium alloys 22

5.3 The influence of grain size and load direction twinning and subsequently tension-compression asymmetry in AZ31 23

5.4 The effect of different extrusion processes on tension-compression asymmetry of AZ series alloys 27

5.5 The effect of multidirectional pre-compression on tension-compression asymmetry of hot rolled AZ31 29

5.6 Influence of temperature and strain rate on tension-compression asymmetry of extruded AM30 magnesium alloy 33

5.6.1 Influence of temperature 35
5.6.2 Influence of strain rate 35
5.7 The effects of equal channel angular pressing on grain refinement 38
5.7.1 Principles of equal channel angular pressing (ECAP) 38
5.7.2 Experimental determination of effects of the ECAP on magnesium alloy 39
6 Experimental determination of tension-compression asymmetry, results, and discussion 41
6.1 Metallographic examination 41
6.2 Tensile and compressive testing 47
7 Discussion 51
8 Conclusions 52
References 53
Symbols and Abbreviations 57

1 Introduction

Magnesium alloys, thanks to their favourable properties such as low density and relatively high strength are very popular for technological and industrial application (automobile and aerospace industries). However due to the nature of HCP structure and limited slip systems, deformation behaviour of magnesium alloys is rather complicated. Basal and prismatic slips are the only four independent slip systems however, to adhere to plastic deformation another deformation mechanism has to be employed. Second order pyramidal slip or deformation twinning are those possible mechanisms. The result of twinning is a substantial change in crystallographic texture. Twinning as a polar mechanism (unidirectional) can activate in different grains during compressive and tensile loading as opposed to dislocation slip. The activation of specific slip system during deformation strongly depend on mutual orientation of loading direction, slip plane, and slip direction, which is further influenced by twinning. [41, 47]

All of this in combination with variety of deformation textures that are produced during plastic deformation contribute to the anisotropy and asymmetrical response to tensile and compressive loading. Tension-compression asymmetry or TCA can be described by a CYS/TYS, a ratio that describes the extent of tension-compression yield asymmetry between compression yield stress (CYS) and tension yield stress (TYS), sometimes also referred to as TCA parameter (or TYS/CYS, preferred value of CYS/TYS is slightly less than 1). [47]

Tension-compression asymmetry limits the technological and structural applications of magnesium alloys for components subjected to tension and compression simultaneously. As previously stated, twinning as a significant deformation mechanism in magnesium alloys (mostly $\{10\bar{1}2\}$ twinning) has a substantial influence on the occurrence of tension-compression asymmetry. Therefore, grain refinement, texture tailoring and precipitation were proven to reduce tension-compression asymmetry.[47]

2 Non-ferrous metals

Non-ferrous metals are defined as metals that do not have any substantial amount of iron in their chemical composition. Generally non-ferrous alloys have iron content of less than one weight percent. The criterium for classification of non-ferrous metals with similar properties is melting point, while other properties such as chemical stability and density have to be taken into the account as well. Non-ferrous metals therefore can be categorized like this: [1]

1. Low melting point metals (Bi, Sn, Cd, Pb, Zn, Sb)
2. Lightweight metals (Mg, Al, Be, Ti)
3. Medium melting point metals (Cu, Ni, Co, Mn)
4. Noble metals (Au, Ag, Pt, Pd, Rh, Ir)
5. High melting point metals (Zr, Cr, V, Nb, Mo, Ta, W)

Non-ferrous metals and their alloys, while more costly that ferrous alloys, are highly desirable for industrial and technological application due to favourable properties of specific metals and their alloys such as light weight (Al, Mg), higher conductivity (Cu, Ag), corrosion resistance (Zn, Cr) etc.

Metal	Melting point [°C]	Density [kg/m^3]
	Low melting point metals	
Bismuth	271	9800
Lead	327	11340
Zinc	419	7132
	Lightweight metals	
Magnesium	650	1740
Aluminium	660	2669
Titan	1660	4510
	Medium melting point metals	
Copper	1083	8940
Nickel	1453	8900
Cobalt	1493	8900
	Noble metals	
Silver	960	10490
Gold	1063	19320
Platinum	1769	21450
	High melting point metals	
Zirconium	1855	6510
Chrome	1875	7190
Vanadium	1950	6110

Table 1 Table of some non-ferrous metals, their melting points and density [1]

2.1 Magnesium

Magnesium is a chemical element with the atomic number 12. It is silvery-white metal which belongs to alkaline earth metal group. Elemental magnesium is lightweight metal with density of just ρ=1,740 g/cm^3, compared to density of another lightweight metal, aluminium ρ=2,70 g/cm^3. Magnesium crystalizes to a hexagonal close-packet (HCP) crystal at the temperature 650°C (923 K). Hexagonal structure is the cause of significant anisotropy in some mechanical and physical properties of pure magnesium, which makes it unsuitable for industrial use.

Elemental magnesium is primarily obtained by electrolysis of $MgCl_2$ in a fused salt electrolyte. For technological applications, pure magnesium is alloyed with a wide number of different alloying components.

2.1.1 Magnesium alloys

Since mechanical properties of pure magnesium are unsuitable for technological applications, magnesium must be alloyed with other elements in order to create a magnesium alloy with much more appropriate properties and characteristics. Most commonly used elements in magnesium alloys are: [1, 2, 3]

- **Aluminium** is most commonly use element in magnesium alloys. The maximum solubility of aluminium in magnesium is 12.7 wt.%, however more often Aluminium content in magnesium alloys varies around 3 to 9 wt.%. At values above 6 wt.% of aluminium content, alloys achieve ideal ratio of strength and ductility. Heat treatment of magnesium alloys is also possible at these values. [3]
- **Zinc** is mostly used in combination with aluminium. In Mg-Al alloys it mostly dissolves in magnesium and becomes a component of precipitation phase. It suppresses effects of iron, increases strength in alloys and increases possibility of the formation of micropores. [2]
- **Manganese** is mostly used in combination with other alloying components, mostly aluminium with which it forms compounds $MnAl, MnAl_4, MnAl_6$. Its maximal content is 1.2 to 2 wt.%. Manganese increases yield strength, corrosion resistance in salt water and decreases solubility of iron in the alloy. [2, 3]
- **Calcium** forms with magnesium creep resistant alloys. It may act as a deoxidant in the melt or during subsequent heat treatment. The corrosion resistance decreases if the calcium content exceeds 2 wt.%. [2, 3]
- **Zirconium** is added to magnesium alloys for grain refinement. It can be used with zinc or rare earth metals. However, alloys cannot contain aluminium or manganese as they would form stable compounds, which would supress grain refinement. [2]
- **Rare earth metals** are used improve mechanical properties at higher temperatures and increase creep resistance. These metals are used in alloys in very small amounts, in hundredths or tenths of percent. Yttrium sometimes falls into this category as well, as it is used to increase creep resistance up to 300°C. [2, 3]
- **Silicon** is used to increase the flowability of molten alloys. It however reduces the corrosion resistance in the presence of iron. [2, 3]

The alloying elements help with improvement of the mechanical properties of magnesium thanks to one or more of the following mechanisms:

- Solid solution hardening
- Precipitation hardening
- Dispersion hardening
- Grain size control

The advantages of magnesium alloys include low density, specific strength comparable to similar characteristics of aluminium and some steels, high vibration damping and very good machinability.
The disadvantages, on the other hand, are low formability at lower temperatures, low rate of diffusion processes during heat treatment and more difficult and therefore more expensive production and processing than aluminium alloys, due to the high reactivity of magnesium at higher temperatures. The adverse features of magnesium alloys are also low shear strength (R_{ms}=120 to 150 MPa), low notch toughness (K= 1.2 to 1.4 J), low hardness and wear resistance and low Young's modulus of elasticity (E= 42 to 44 GPa).

Cast magnesium alloys are preferred to wrought magnesium alloys in production, due to their low formability. However, there is no significant difference between the chemical composition of cast and wrought magnesium alloys. Wrought magnesium alloys crystalize in HCP and at a room temperature have active only one slip system. By raising a temperature above 225°C additional slip systems activate, and recrystallization processes are applied. The forming temperatures of wrought magnesium alloys range from 200°C to 300°C for forging, from 300°C to 400°C for extrusion and from 400°C to 500°C for rolling. Wrought magnesium alloys have finer grain and more homogeneous structure compared to the cast alloys, therefore they have slightly better mechanical properties. The most common wrought alloys are: AZ31, AZ61, AZ80, ZK60, etc.

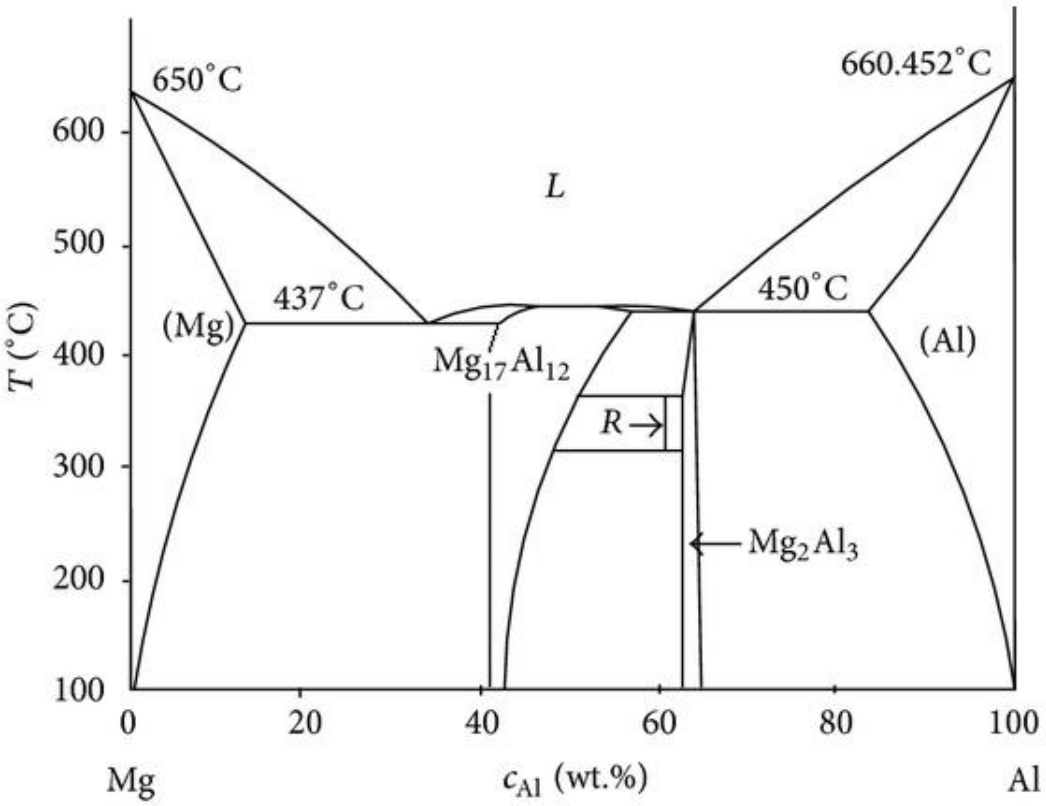

Figure 1 Binary phase diagram Mg-Al [8, 9]

3 Tensile testing

The tensile testing is one of the most basic mechanical tests, which thanks to its practicality and simplicity is one of the most widespread and established testing methods to assess mechanical properties of predominantly metal materials. Tensile testing is a destructive testing method that can determine yield strength, ultimate tensile strength, ductility, modulus of elasticity etc. of any material. The test consists of a simply shaped smooth testing specimen, mostly with circular or rectangular cross-section, attached to the jaws of the testing machine. The test determines the dependence of the applied force on elongation of a specimen or the dependence of the stress on the deformation until the specimen breaks using an extensometer mounted on the specimen. The output of the test is therefore a graph of this dependence as well as values of stress and strain of the tested specimen. [11, 16]

3.1 Tensile testing machines

Tensile testing machines or tension test machines are testing machines specially configured to evaluate the tensile characteristics of specimens. Their task is to determine yield strength, ultimate tensile strength, elongation. They are part of the basic equipment of any mechanical testing laboratory. They are designed to accommodate number of different specimens either by size or clamping method. There are 2 variants of these machines, vertical and horizontal, depending on the position of the loading axis of a test specimen. Additionally, according to the load type and drive they can be divided into two categories, mechanical and hydraulic. [Figure 2] In addition to basic configuration there are also universal testing machines, which are also designed for compression and bending tests. Regardless of the fact that these machines were being produced since the end of the last century, the very principle of the testing machines remains unchanged. [11, 16]

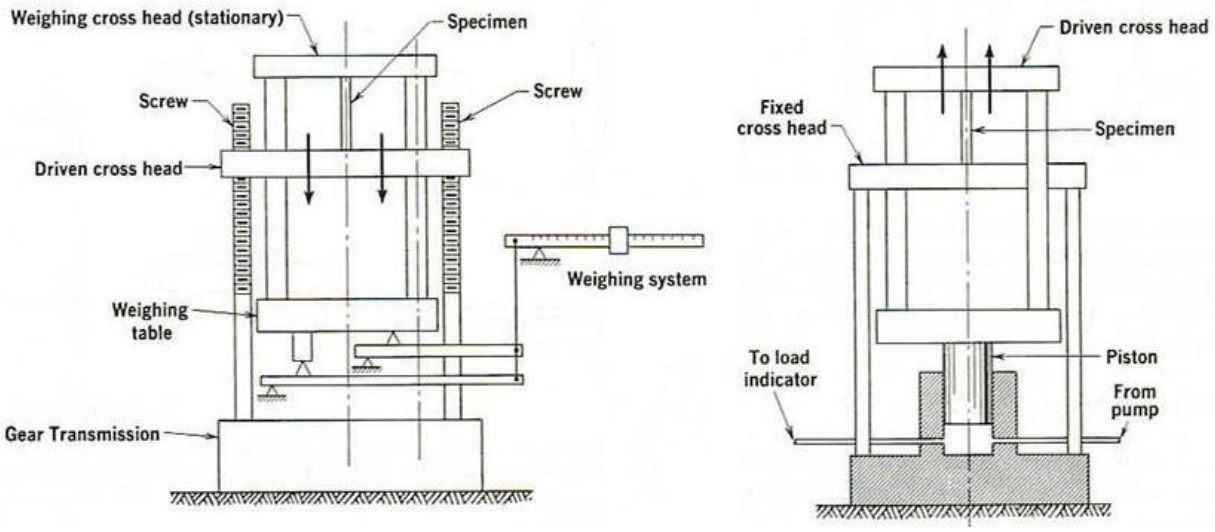

Figure 2 Schematic representation of a mechanical and hydraulic tensile testing machines [25]

3.2 Stress-strain diagram

Testing machines record stress-strain diagram as a function of the resistance of the testing specimen against deformation and fracture, and there are three types of coordinate value system into which it can be plotted: [16]

- Absolute quantitative variables F-L (Force – Elongation)
- Proportional engineering quantitative variables (R-ε)
- Proportional true quantitative variables (σ-$\overline{\varepsilon}$)

Due to similarities in shape of diagrams of true and engineering variables, the absolute variables force-elongation $(F - \Delta L)$ can be converted to proportional engineering variables stress-strain $(E - \varepsilon)$ according to the following formulas:

$$R = \frac{F}{S_0}\ [MPa]$$

$$\varepsilon = \frac{L - L_0}{L_0}\ [-]\ or\ \varepsilon = \frac{L - L_0}{L_0} \cdot 100\ [\%]$$

Where F is force applied on the specimen [N], S_0 is original cross-section of a test specimen [m^2], L_0 is original length of a test specimen [m], $(L - L_0)$ represents increase in length [m]. [11]

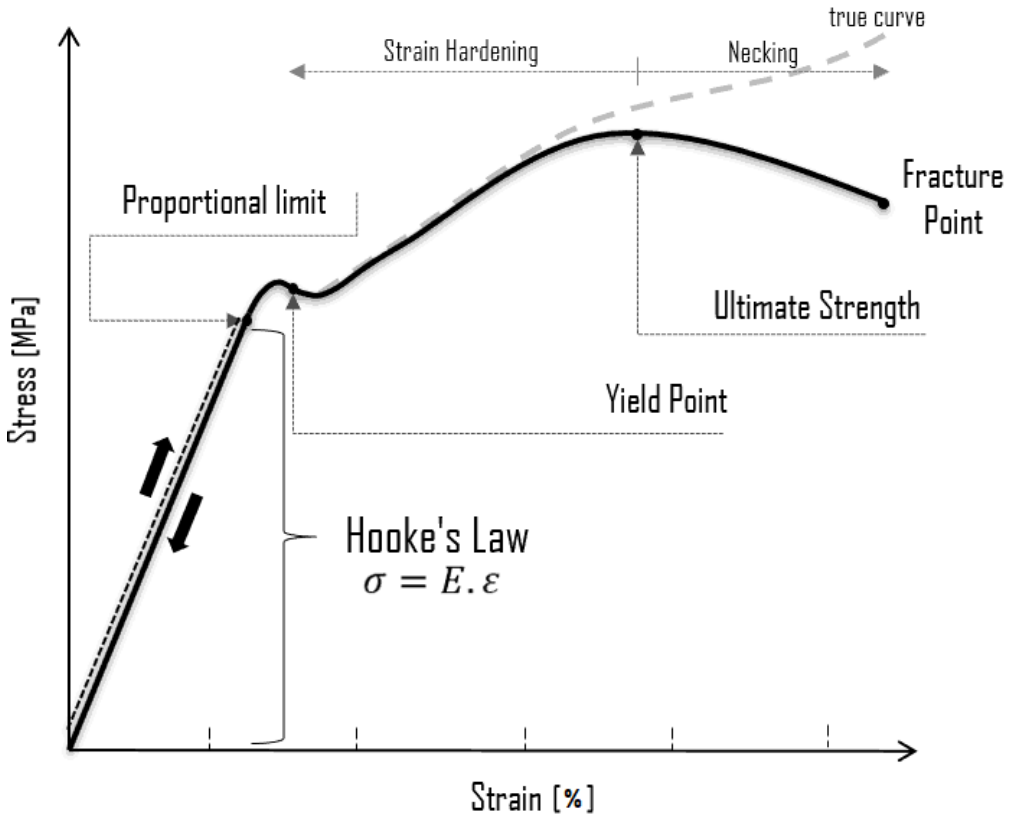

Figure 3 Engineering stress-strain diagram of a ductile material [24]

Initial section of the stress-strain diagram is a straight line and corresponds with elastic deformation. This line can be described by Hook 's law: [Figure 3]

$$R = E \cdot \varepsilon\ [MPa]$$

Where E is modulus of elasticity or Young's modulus of a test specimen and ε is deformation.

In next section of the stress-strain diagram, linear dependence deviates due to plastic deformation, increment of stress as a function of deformation then gradually reaches zero. Up until that point the test specimen deforms uniformly. Further deformation is accompanied by decrease of stress and necking of the specimen, which then ends with a fracture of the specimen. [11]

Formulas for conversion of engineering stress and strain to true stress and strain are:

$$\sigma = \frac{F}{S} = R \cdot \frac{S_0}{S} = R \cdot (1 + \varepsilon)\ [MPa]$$

$$\overline{\varepsilon} = ln\frac{L}{L_0} = ln\frac{S_0}{S} = ln(1 + \varepsilon)\ [-]$$

Where S is true cross-section of a test specimen. [11, 16] These formulas (Hollomon's and Ramberg-Osgood's equation) are used as a general description of a true stress-strain diagram:

$$\sigma = K \cdot \overline{\varepsilon}_{pl}{}^{n}\ [MPa]$$

$$\overline{\varepsilon}_c = \overline{\varepsilon}_{el} + \overline{\varepsilon}_{pl} = \frac{\sigma}{E} + \left(\frac{\sigma}{K}\right)^{\frac{1}{n}}\ [-]$$

Where K is strain hardening coefficient, $\overline{\varepsilon}_{pl}$ is true plastic deformation, n is strain hardening exponent, $\overline{\varepsilon}_c$ is true total deformation, $\overline{\varepsilon}_{el}$ is true elastic deformation and E is modulus of elasticity of a test specimen. [11, 13]

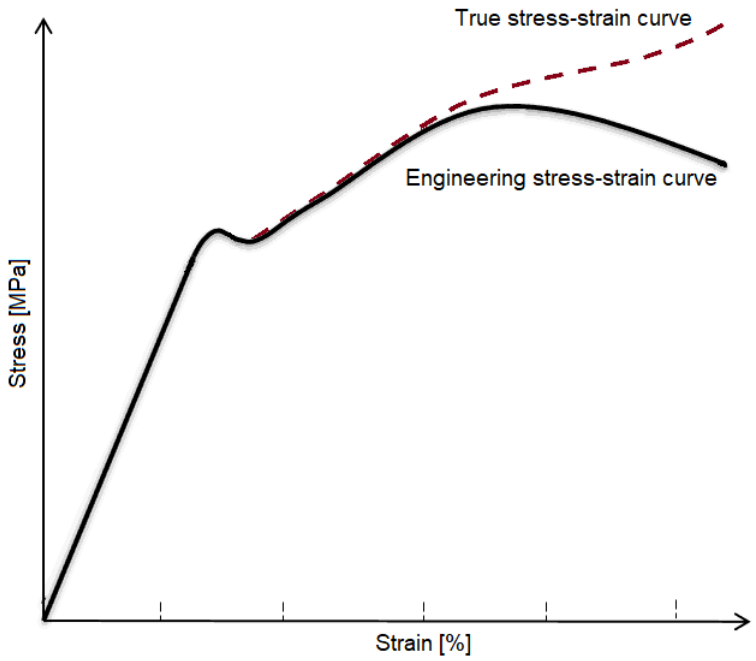

Figure 4 Difference between engineering and true stress-strain diagram

Engineering stress-strain diagram serves to estimate behaviour of the tested material in technical applications and determine stress and strain characteristics of materials. Essentially it can be only used in case of small deformations and small changes in shape of the test specimen. [Figure 4] [11, 16]

3.3 Stress characteristics

In terms of deformation, stress-strain diagram consists of two deformation areas – elastic and plastic-elastic. While the elastic areas represent an elongation of the specimen, that reverts back to its original state after unloading (reversible deformation), in the plastic-elastic area there is a proportion of permanent (irreversible) deformation that remains, even after unloading.

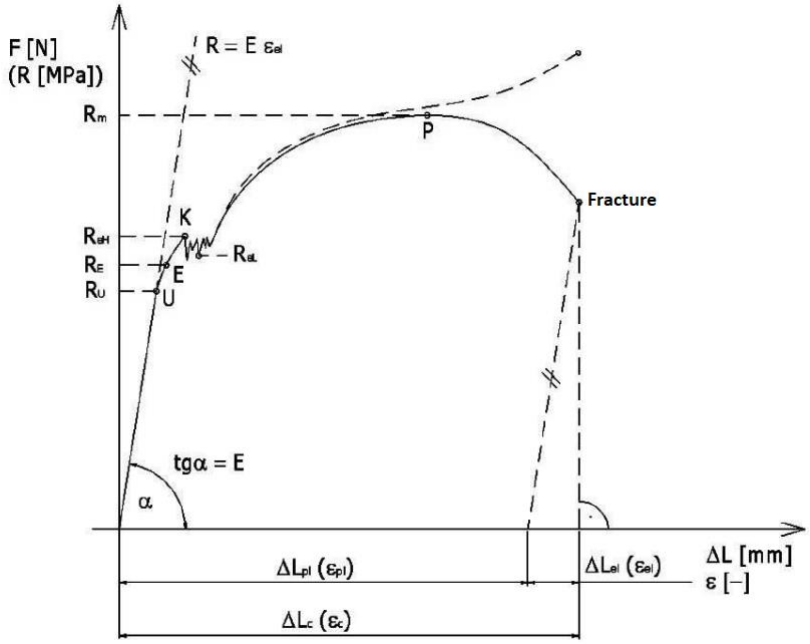

Figure 5 Engineering stress-strain diagram with marked stress characteristics [12]

Stress characteristics of the stress-strain diagram are: [Figure 5] [11, 12, 13]

- Modulus of elasticity - E
- Proportional limit - R_U
- Elasticity limit - R_E
- Yield strength – R_e
- Ultimate tensile strength - R_m
- Fracture strength – R_f

Modulus of elasticity E (Young's modulus of elasticity) measures object's resistance to being deformed elastically. It is determined in linear section of stress-strain diagram, as a slope of a stress-strain curve in this section.

$$E = tg\ \alpha = \frac{R}{\varepsilon} \quad [MPa]$$

Where α is angle formed by the line drawn by this part of the diagram and the axis of strain ε. [Figure 5] [11, 16]

The highest stress at which Hooke's law still applies is called proportional limit R_U. It is the stress at which the curve in the elastic section of the diagram stops being linear. Determination of proportional limit R_U and elasticity limit R_E heavily depends on sensitivity of the extensometer, therefore these parameters are not usually measured.

Tensile yield strength is defined as stress at which plastic deformation occurs. Although value of yield strength can depend on sensitivity of sensors as well. Therefore, offset yield strength $R_{p0.2}$ is introduced. It is defined as a stress, which causes permanent plastic deformation of $\varepsilon_{pl} = 0.002$ (0.2%). Thus, total deformation ε_c under stress $R_{p0.2}$ is:

$$\varepsilon_c = \varepsilon_{pl} + \varepsilon_{el} = \varepsilon_{pl} + \frac{R_{p0.2}}{E} \quad [-]$$

Offset yield strength is often used to determine the maximum load of mechanical components, since it represents the upper limit at which permanent deformation has still yet to occur. [11]

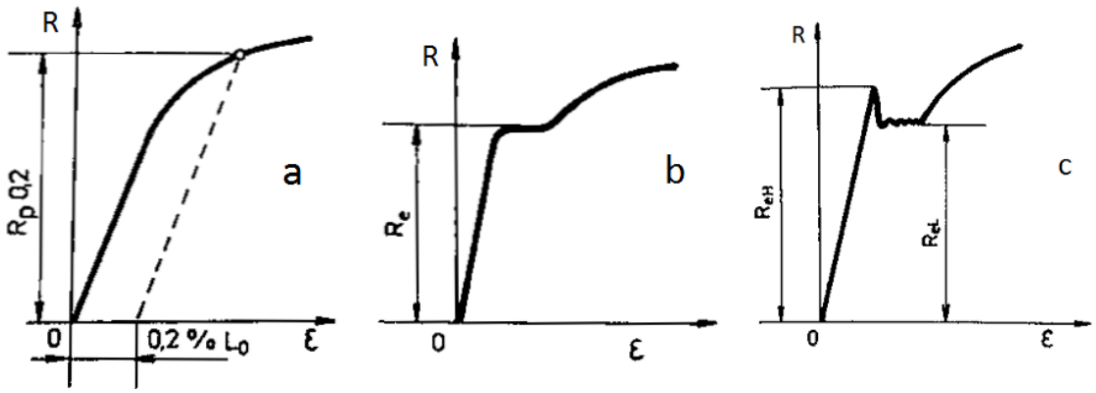

Figure 6 a) Offset yield strength, b) Pronounced yield strength c) Pronounced yield strength with Lüders deformation [16]

Specific cases are the materials that show a very heterogeneous process of creation of plastic deformation, thanks to the atoms of nitrogen or carbon, acting as an anchor points for dislocations. These types of materials, due to formations of plastic deformation, create very characteristically shaped stress-strain diagram in the section of yield strength, shown in the Fig 5c. The first value, R_{eH} (upper yield point), marks the end of the of the linear section of the diagram followed by significant decrease in stress. The decrease is accompanied by expansion of the plastic deformation across the entire cross-section along the specific length of the test specimen. The value at which stress drops is called lower yield point R_{eL}. The slip strips gradually extend along the entire specific length of the test specimen. The deformation at constant value of this stress is called Lüders deformation.

Ultimate tensile strength R_m is the maximal stress achieved in engineering stress-strain diagram, which is ratio of maximal force achieved in the test (F_{max}) to the original cross-section of the testing specimen (S_0).

$$R_m = \frac{F_{max}}{S_0}\ [MPa]$$

In case of ductile material, ultimate tensile strength is given by the value of engineering stress at which process of necking starts on the test specimen. The fracture occurs at the engineering stress R_f (fracture stress). In case of brittle materials, it is possible that the fracture occurs when maximal stress is reached, and so the resulting plastic deformation is non-existent, or it is very small. If fracture occurs after small or no plastic deformation, then the value R_m corresponds to the value of stress at the moment of fracture R_f(fracture stress). [11]

3.4 Strain characteristics

The strain characteristics are determined on the basis of the dimensions (and change of dimensions) of the specific part of the test specimen before and after testing. The strain characteristics are determined on unloaded specimens, so they are dependent only on plastic deformation of a tested material. The greatest elongation in ductile materials occur in the area of the neck, which starts forming at ultimate tensile strength up until fracture occurs, and its shape depends on the cross-section of the specimen. Consequently, different types of elongations are measured along the testing process. [Figure 7] [11, 12]

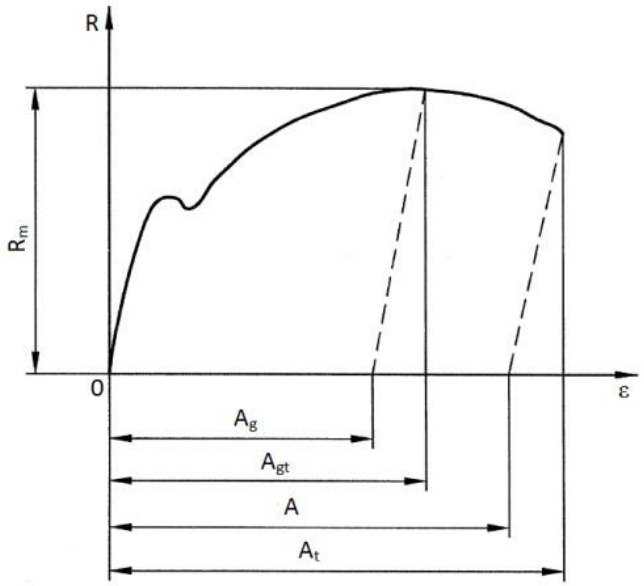

Figure 7 Diagram representing different stages of elongation along the stress-strain curve (A_g – plastic elongation at maximum force, A_{gt} – total elongation at maximum force, A – elongation after fracture, A_t – total elongation at fracture)

Elongation A and reduction of area Z are determined as: [11, 16]

$$A = \frac{L_u - L_0}{L_0} \cdot 100 = \frac{\Delta L}{L_0} \cdot 100 \quad [\%],$$

$$Z = \frac{S_0 - S_u}{S_0} \cdot 100 = \frac{\Delta S}{S_0} \cdot 100 \quad [\%],$$

Where L_0 is original gauge length [m], L_u is final gauge length after fracture [m], S_0 is initial cross-section of the tested area [m^2], S_u is minimal cross-section after fracture [m^2]. Furthermore, for a test specimen with circular cross-section applies: [11, 16]

$$Z = \frac{{d_0}^2 - {d_u}^2}{{d_0}^2} \cdot 100 \quad [\%],$$

where d_0 is original diameter of the specimen and d_u is diameter of the specimen after fracture.

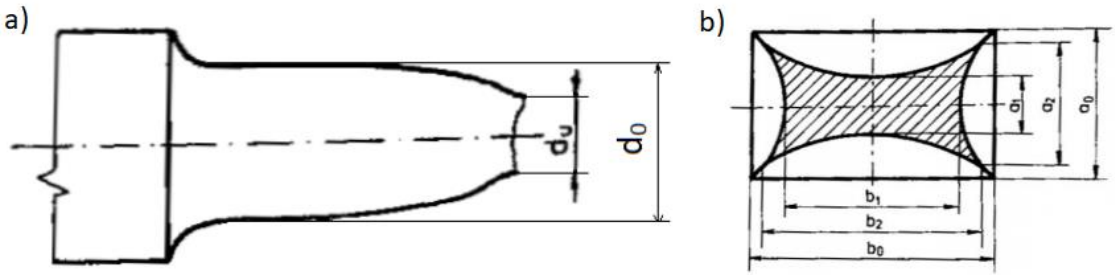

Figure 8 Reduction of a cross-section area of specimens for a) circular specimen, b) rectangular specimen [16]

3.5 Strain rate

Strain rate is speed or rate at which material deforms under applied stress, with respect to time. Most materials display different strength and strain characteristics at different speeds, which means that straining rate has a considerable impact on the shape of the stress-strain diagram.

Strain rate is defined as: [12, 13]

$$\dot{\varepsilon} = \frac{d\varepsilon}{d\tau} \quad [s^{-1}],$$

Where $\frac{d\varepsilon}{d\tau}$ represents strain change in time. Yield strength and deformation stress at lower values of plastic deformation are more influenced by the straining rate that ultimate tensile strength. If the crosshead separation rate of the testing machine is:

$$v = \frac{dL}{d\tau} \quad [m \cdot s^{-1}],$$

Then the straining rate described with the engineering strain is:

$$\dot{\varepsilon} = \frac{d\varepsilon}{d\tau} = \frac{\frac{d(L - L_0)}{L_0}}{d\tau} = \frac{1}{L}\frac{dL}{d\tau} = \frac{v}{L_0} \quad [s^{-1}]$$

Engineering strain rate is proportional to the crosshead separation rate, the true strain rate is defined as:

$$\dot{\varepsilon}_s = \frac{d\varepsilon_s}{d\tau} = \frac{d\left[ln\left(\frac{L}{L_0}\right)\right]}{d\tau} = \frac{1}{L}\frac{dL}{d\tau} = \frac{v}{L} \quad [s^{-1}]$$

Which shows that at constant crosshead separation rate, the true strain rate will decrease with elongation of the specimen, or reduction of its cross-section area. Tensile tests performed at a constant true strain rate require monitoring with feedback to alter the crosshead separation rate with changing cross-section. True straining rate relates to engineering strain rate:

$$\dot{\varepsilon}_s = \frac{v}{L} = \frac{L_0}{L}\frac{d\varepsilon}{d\tau} = \frac{1}{1+\varepsilon}\frac{d\varepsilon}{d\tau} = \frac{\varepsilon}{1+\varepsilon} \quad [s^{-1}],$$

Strain rates generally utilized in tensile tests range from 10^{-5} to 10^{-1} s^{-1}. [12, 13]

3.6 Strain hardening

In polycrystal metallic materials, plastic deformation is created by a constant increase in stress. Strain hardening is determined by the movement, interactions, and multiplication of dislocations, while the amount of dislocations increase parabolically. These dislocations interact with each other or with other crystallographic defects such as grain boundaries. Even if transition to an adjacent grain is possible, movement of the dislocations usually ceases at the grain boundary. Dislocations accumulate at the grain boundary, thus forming clusters of dislocations. As this accumulation of dislocations continue, a back stress develops preventing further movement of dislocations, producing mechanical strengthening. This section of a stress-strain diagram, the section of uniform plastic deformation, at which parabolic strain hardening occurs is described by the Hollomon's equation: [11,13]

$$\sigma = K \cdot \bar{\varepsilon}^{\,n} \quad [MPa],$$

Where σ is stress applied on material, K is strength coefficient (material constant), $\bar{\varepsilon}$ is strain, and n is strain hardening exponent (material constant). The value of strain hardening exponent ranges between 0 and 1, where 0 means that material is perfectly plastic and 1 means that material is perfectly elastic. The value of strain hardening exponent for most metal materials ranges between 0.1 to 0.6. Simple modification of Hollomon's equation describes linear

dependence in logarithmic coordinates of the true stress-true strain ($\ln\sigma - \ln\varepsilon$), where n indicates slope of this curve:

$$\ln\sigma = \ln K + n \cdot \ln\varepsilon$$

The shape of a stress-strain curve beyond the yield point depends on the degree of strain hardening h, which is determined by ultimate tensile strength Rm and yield strength Re:

$$h = \frac{R_m}{R_e} \quad [-]$$

Values higher than 1.4 represent high degree of strain hardening, while values below 1.2 represent low degree of strain hardening. [13]

3.7 Test specimens

Geometry and dimension are standardized by various norms (ČSN EN ISO 6892-1), but in the end shape and dimensions of test specimens usually depend on the shape and dimensions of a part or a component the specimens are taken from. Test specimen is usually obtained by machining a specimen from a part, component, or a cast, although components with symmetrical cross-section (wires, bars, profiles) can be tested without having to be machined. Cross-section of a test specimen can be circular, square, rectangular, annular, in special cases even different shapes. [Figure 9] [12, 16]

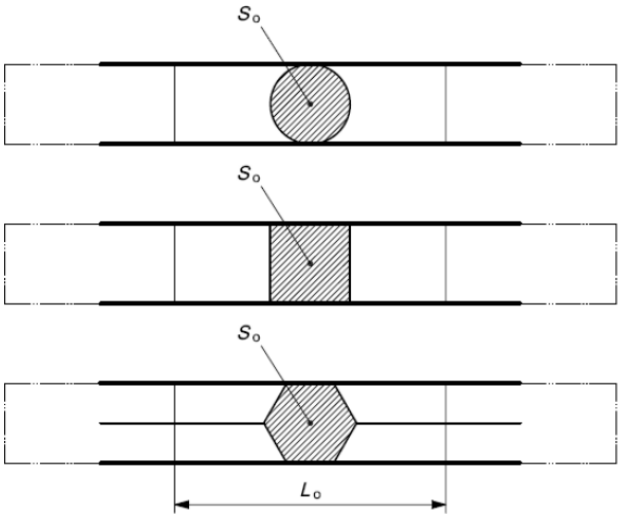

Figure 9 Example of cross-sections of test specimens (S_0 - initial cross-section of the tested area, L_0 - original gauge length)

The most commonly used test specimens have direct correlation between original gauge length L_0 and initial cross-section of the tested area S_0, and they are called proportional test specimens, defined by the equation: [12]

$$L_0 = k\sqrt{S_0}$$

Where k is coefficient of proportionality. Normally used coefficient of proportionality k is 5.56 (mostly for shorter test specimens), with minimal required original gauge length L_0 = 15mm. However, higher value of coefficient (predominantly k=11.3, for longer test specimens), or non-proportional test specimens can be used, in case when cross-section area is too small to fulfil these requirements.

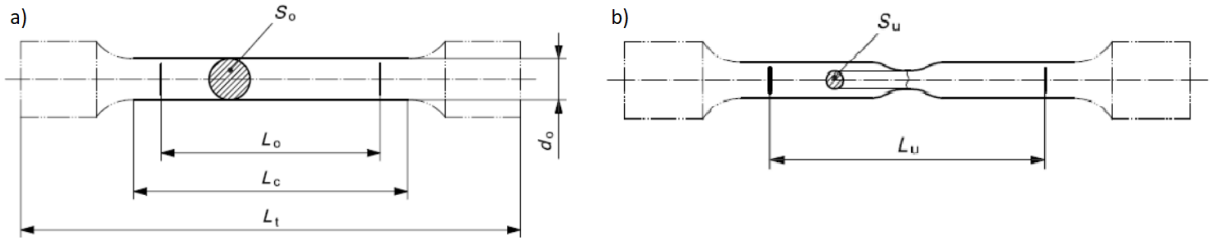

Figure 10 Example of a test specimen with circular cross-section a) before and b) after testing, with essential dimensions (L_t – overall length of a test specimen, L_c – parallel length, L_0 – original gauge length, S_0 – initial cross-section of the tested area, d_0 – initial diameter of a parallel length, L_u – final gauge length after fracture, S_u – minimal cross-section after fracture) [12]

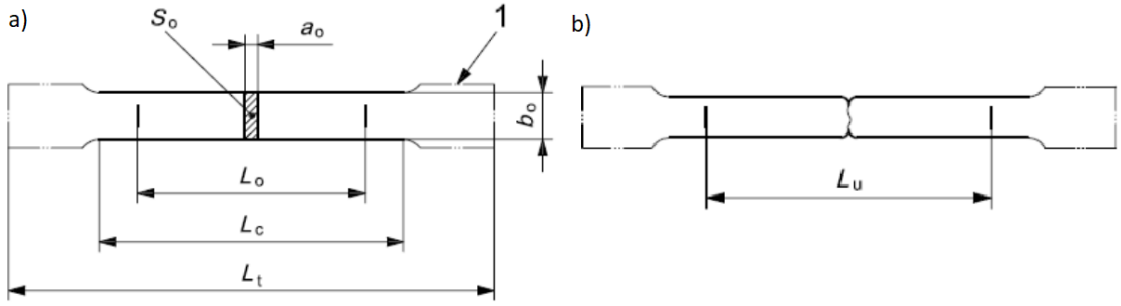

Figure 11 Example of a flat test specimen with rectangular cross-section a) before and b) after testing, with essential dimensions (L_t – overall length of a test specimen, L_c – parallel length, L_0 – original gauge length, S_0 – initial cross-section of the tested area, a_0 – initial thickness of a flat test specimen, a_0 – initial width of parallel length of a flat test specimen, L_u – final gauge length after fracture) [12]

3.7.1 Standardized dimensions

Dimensions, geometry, and surface finish of test specimens are standardized according to ČSN EN ISO 6892-1: [Table 2, 3]

Coefficient of proportionality k	Diameter d_0 [mm]	Original gauge length $L_0 = k\sqrt{S_0}$ [mm]	Minimum parallel length L_c [mm]
5.65	20	100	110
	14	70	77
	10	50	55
	5	25	28

Table 2 Table of proportional dimensions for cylindrical test specimens [12]

Width b_0 [mm]	Diameter d_0 [mm]	Minimum parallel length L_c [mm]	Approximately total length L_t [mm]
40 ± 0.7	200	220	450
25 ± 0.7	200	212.5	450
20 ± 0.5	80	90	300

Table 3 Table of typical dimensions for flat test specimens [12]

3.7.2 Miniature test specimens

Primary reason behind use of miniature specimens is development of new materials, while secondary reason is to use the least amount of material out of parts and components still in service, to create test specimens. While dimensions and geometry of regular sized specimens are standardized by various norms, miniature specimens have yet to be standardized. The smallest specimen to be considered, according to ČSN EN ISO 6892-1, is specimen with circular cross-section and original diameter d_0=5mm. Assuming that proportionality of the test specimens is observed, specimens with d_0=4mm would be considered miniature, which is supported by German norm DIN 50125 as well. According to the American norm ASTM E8(M) all specimens with d_0=9 mm and lower are considered small, while all test specimens with d_0=2.5 mm would be considered miniature. [8]

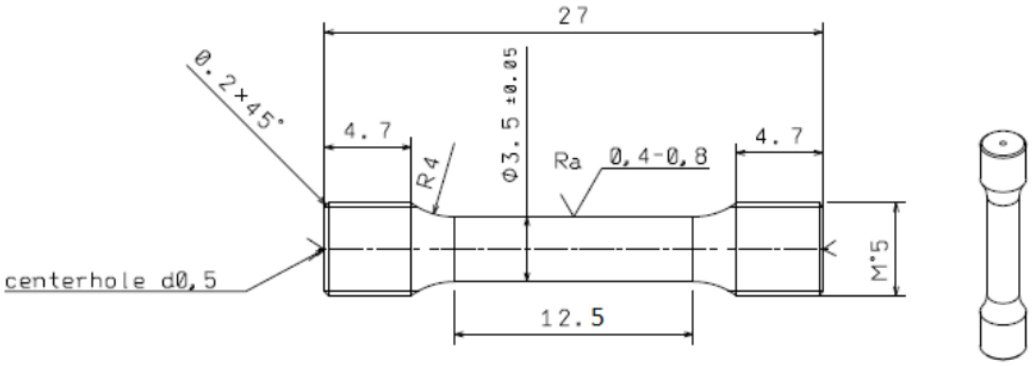

Figure 12 Example of what could be considered miniature test specimen with d_0=3.5mm [23]

As use of miniature specimens is not yet standardized for anything other than thin foil testing materials according to ASTM E345-93. Use of miniature testing specimens has a considerable potential to provide data representative of macro-behaviour of material during tensile tests. However, miniaturization of test specimens comes with a number of potential issues that may affect the results of the testing, such as “scaling effect”, which characterizes the impact of dimensions and geometry of the miniature test specimens on the behaviour of materials during tensile testing. There are also a number of other potential issues concerning specimen geometry, preparations methods of specimens, microstructural changes, ductility, etc. [14] Following issues concerning miniature test specimens should be considered:

- Test specimens can vary in the type of preparation methods used (grinding, polishing, EDM), therefore any damage or irregularity caused by the number preparation methods may add up, which could affect the testing results. The flow stress and ductility can be considerably affected by micro-structural features such as grain size and shape, orientation, texture, distribution, and size of precipitates relative to the dimensions of the specimens. [14]
- Miniature-sized specimens limit the use of standard extensometers, as well as displacement data obtained from the movement of the cross-head may be inaccurate, or with a large amount of scatter. Therefore, different techniques of strain measurement have to be utilized, such as LVDT, capacitance gauges, line scan cameras, laser interferometry, digital image correlation, electrical resistance-based transducers etc. [14]
- Repeatability, verifiability, and validity of testing procedures. For testing results to be valid and comparable, some basic similarity between test specimens, testing conditions, methods of preparations of specimens etc. have to be met. [14]

4 Compressive testing

Compressive testing is important mainly for the evaluation of brittle materials, and materials subjected to compressive loading (building materials, bearing metals, cast iron etc.) In the compressive testing, the force is applied in the axis of the test specimen, similarly to the tensile testing, but with the opposite direction. The stress-strain diagram in compression of tough materials is similar to the stress-strain diagram in tension, except the values of stress and strain are inverted. [Figure 13] [11]

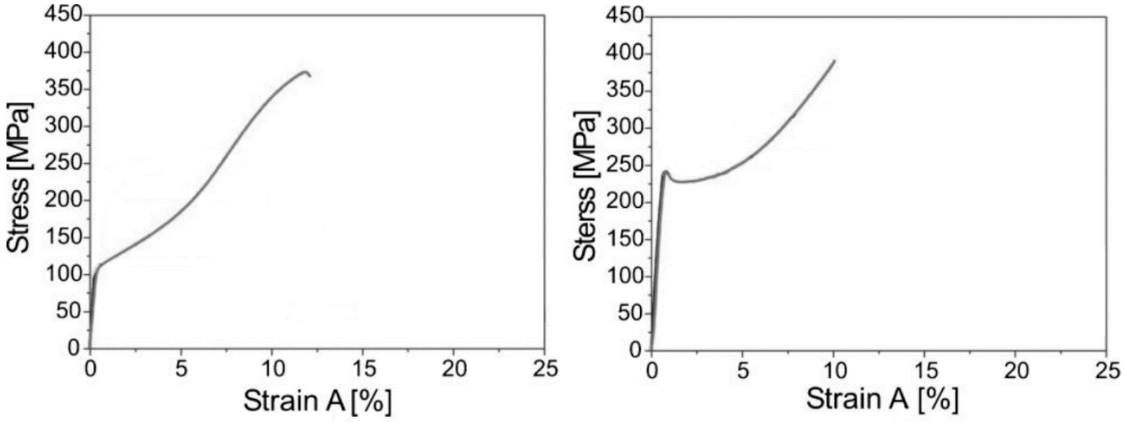

Figure 13 Stress-strain compressive diagram for a) indirectly extruded at 300°C and b) hydrostatically extruded at 100°C AZ31 magnesium alloy [39]

Up until the yield strength, the compressive deformation is elastic and after unloading, the test specimen reverts back to its original shape and size. These elastic deformations are similar to the elastic deformation of the tensile test specimens, and they are measured by precise tensometers. Up until the proportional limit, the Hook's law applies, from which the modulus of elasticity in compression can be determined. After exceeding the compressive yield strength, the increase in resistance to compression occurs, due to hardening caused by the plastic deformation. This increase is reflected in stress-strain curve. For soft and malleable materials, the hardening is negligible, and the test specimen is therefore compressed to flat disk. However, in such cases it is impossible to determine the moment when the failure occurred. For such materials, the test is performed until the values of stress slightly exceeds the value of yield strength in compression.

Ultimate compressive strength is defined as:

$$R_{Pd} = \frac{F_{max}}{S_0} \quad [MPa]$$

where F_{max} is the amount of force at the time of failure [N], and S_0 is initial cross-section [m^2]. [11]

While tensile tests are more commonly used to determine the mechanical properties of ductile materials, compressive tests are used to evaluate volume formability of these materials. Similarly, to the tensile tests, in compressive tests the dependence of true stress on true compressive strain is determined.

Compressive tests are performed using same apparatus or machines as tensile tests. However gripping jaws are replaced by anvils and movement of the crosshead is inverted (crosshead moves towards stationary grip rather than away from it). [Figure 14]

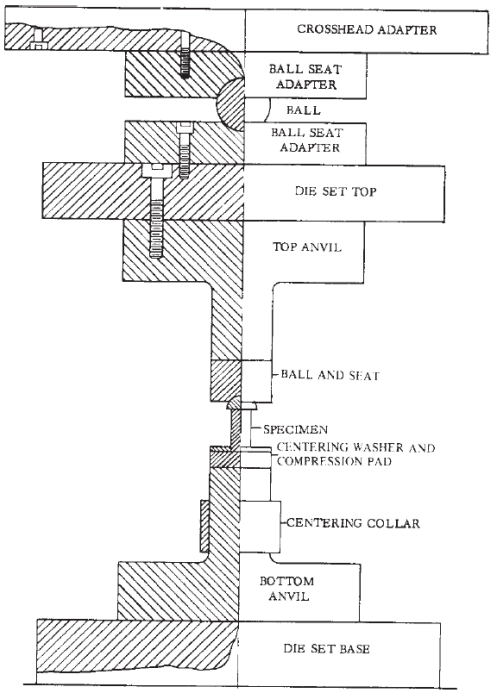

Figure 14 Example of compressive testing apparatus according to ASTM E9-89a[17]

4.1 Test specimens

Test specimens meant for compression testing have simple solid circular cylinder shape, in some cases specimens can be rectangular as well. Their size is determined by H_0 the original length and S_0 the original diameter. Their dimensions and geometry are standardized by ASTM E9-89a: [Table 4]

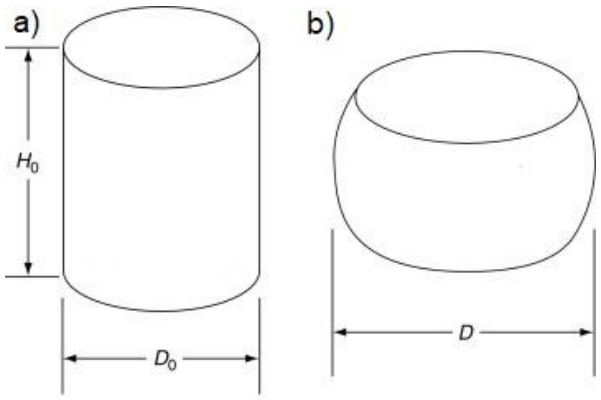

Figure 15 Compression test specimen a) before and b) after loading [18]

Specimens	Diameter		Length		Approximate L/D Ratio
	in.	Mm	In.	mm	
Short	1.12 ± 0.01	30.0 ± 0.2	1.00 ± 0.05	25.0 ± 1.0	0.8
	0.50 ± 0.01	13.0 ± 0.2	1.00 ± 0.05	25.0 ± 1.0	2.0
Medium	0.50 ± 0.01	13.0 ± 0.2	1.50 ± 0.05	38.0 ± 1.0	3.0
	0.80 ± 0.01	20.0 ± 0.2	2.38 ± 0.12	60.0 ± 3.0	3.0
	1.00 ± 0.01	25.0 ± 0.2	3.00 ± 0.12	75.0 ± 3.0	3.0
	1.12 ± 0.01	30.0 ± 0.2	3.38 ± 0.12	85.0 ± 3.0	3.0
Long	0.80 ± 0.01	20.0 ± 0.2	6.38 ± 0.12	160.0 ± 3.0	8.0
	1.25 ± 0.01	32.0 ± 0.2	12.50 min	320.0 min	10.0

Table 4 Dimensions of compressive test specimens according to ASTM E9-89a [17]

Short test specimens are usually used for determination of mechanical properties in compression of bearing metals, which are typically used in a form of small, or thin components designed to carry loads perpendicular to the surface. Medium-length test specimens are used for general determination of mechanical properties in compression of most metals. Long specimens are used to determine the modulus of elasticity in compression of metals. For determination of compressive strength of high-strength metals, the specimens with L/D ratio of 1.5 and 2.0 are most appropriate. [17]

Different modes of deformation can occur in compressive tests: [26]

- Buckling occurs when L/D > 5
- Shearing occurs when L/D > 2.5
- Double barrelling occurs when L/D > 2.0 and friction is present at the contact surfaces
- Barrelling occurs when L/D < 2.0 and friction is present at the contact surfaces
- Homogenous compression occurs when L/D < 2.0 and no friction is present at the contact surfaces
- Compressive instability occurs due to work-softening

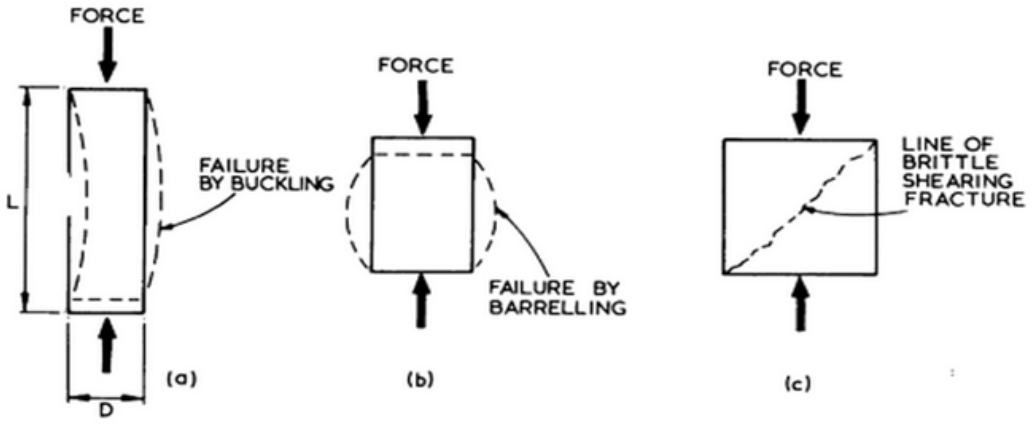

Figure 16 More comprehensive view of the modes of failure of compressive test specimens a) buckling, b) barrelling (unfavourable modes of deformation) and c) brittle shearing fracture [26]

4.2 Stability and buckling

If the axial compressive load is applied to a slender column, at certain value of the load, the column will bow, or buckle in an undetermined direction. Therefore, this load is plainly the buckling load of the column. The buckling direction implies a degree of asymmetry in the column, caused by the geometrical or material imperfection. [22]

If compressive load caused the column to buckle, the compressive load P achieved the critical value P_{cr} defined as:

$$P_{cr} = \frac{n^2 \pi^2 E J_{min}}{l^2} \quad [MPa],$$

where P_{cr} is critical value of force applied to the column, E is modulus of elasticity, J_{min} is minimal value of the second moment of area, l is length of the specimen and n is buckling load (the most important is the first case, n=1). [21, 22]

Further critical stress σ_{cr} corresponds to P_{cr}:

$$\sigma_{cr} = \frac{\pi^2 E}{(l/r)^2} \quad [MPa]$$

where r is radius of gyration of the cross-sectional area of the column and l/r is considered slenderness ration of the column. That is however only applicable until the yield point of the material is reached. [21, 22]

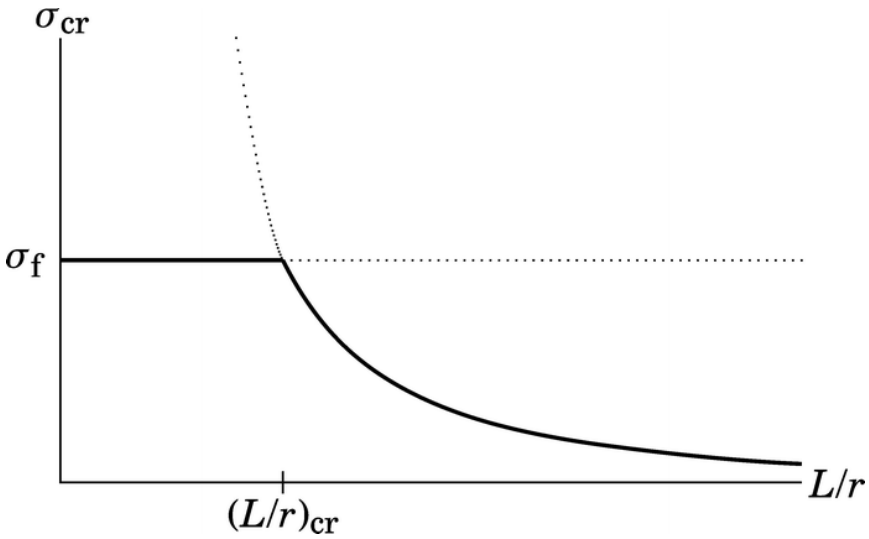

Figure 17 Column curve (critical stress against slenderness ratio), general case [21]

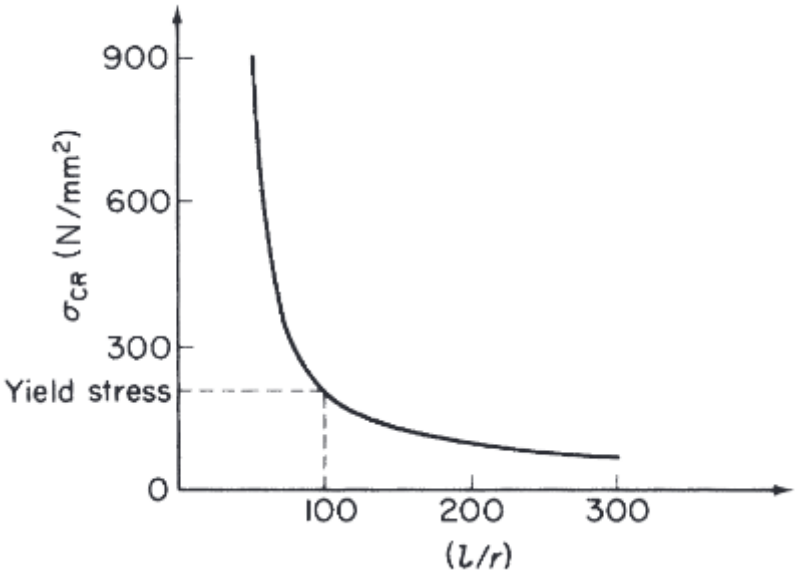

Figure 18 Column curve (critical stress against slenderness ratio) for mild steel [22]

5 Tension-compression asymmetry

5.1 Bauschinger effect

Bauschinger effect, named after German mathematician and professor of engineering mechanics in 1881, describes phenomenon where yield stress of polycrystalline metal specimens is reduced following pre-strain in the opposite load direction. [27]

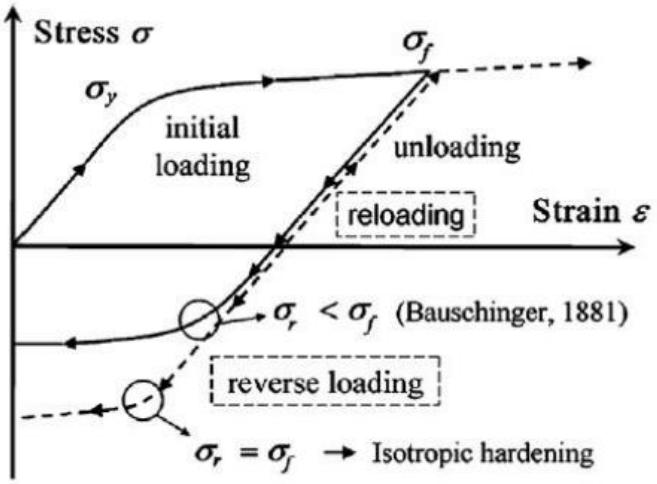

Figure 19 Stress-strain curve, showing the impact of the Bauschinger effect on metal alloys [32, 33]

5.1.1 Bauschinger effect parameters

The absolute value of Bauschinger effect can be described by three set parameters: stress, strain, and energy parameters.

5.1.1.1 Stress parameter

Bauschinger effect described by the stress parameter $\beta_{\sigma 1}$, is relative decrease of yield stress observed during forward to reverse deformation. Witch results in stress parameter being dependent on pre-stress: [27]

$$\beta_{\sigma 1} = \frac{\sigma_p - \sigma_r}{\sigma_p}$$

Where σ_p is maximal pre-stress [MPa] and σ_r is yield stress in the direction of reverse strain [MPa]. The higher the value of β_σ is, the higher the impact Bauschinger effect has on the specimens.

Besides stress parameter $\beta_{\sigma 1}$, Bauschinger effect can be described by three other stress parameters, which are associated with different points on forward-reverse stress-strain curve. The parameters $\beta_{\sigma 2}$, $\beta_{\sigma 3}$ and $\beta_{\sigma 4}$ are calculated using stress values at 0.2 % and 0.5 % of reverse strain. The parameters show the rate of property restoration during reverse straining after the yield drop:

$$\beta_{\sigma 2} = \frac{\sigma_p - \sigma_{r0.2}}{\sigma_p}, \beta_{\sigma 3} = \frac{\sigma_p - \sigma_{r0.5}}{\sigma_p}, \beta_{\sigma 4} = \frac{\sigma_{r0.5}}{\sigma_p}$$

Where $\sigma_{r0.2}$ and $\sigma_{r0.5}$ are stresses at 0.2 % and 0.5 % of reverse strain [MPa].

While stress parameter $\beta_{\sigma 1}$ describes the "short range" work-softening, stress parameters $\beta_{\sigma 2}$, $\beta_{\sigma 3}$ and $\beta_{\sigma 4}$ represent "long range" work-softening and portray how permanent the Bauschinger effect is when deformation is changed in the reverse direction. [27]

5.1.1.2 Strain parameter

Bauschinger effect described by the strain parameter β_{ε}, is amount of deformation in opposite load direction, needed in order to reach pre-stress level of stress: [27]

$$\beta_{\varepsilon} = \frac{\varepsilon_r}{\varepsilon_p}$$

Where ε_p is plastic pre-strain [-] and ε_r is value of plastic strain in opposite load direction of equal value of stress to the pre-stress [-].

5.1.1.3 *Energy parameter*

During deformation, the energy in the specimen is stored in the form of dislocation, point defects etc. Part of this stored energy is changing with the percentual portion of deformation.

Bauschinger effect described by the energy parameter β_E is energy needed during the reverse deformation in order to reach the pre-stress level of stress: [27]

$$\beta_E = \frac{E_s}{E_p}$$

Where E_p is energy used up during pre-strain [J] and E_s is energy saved during reverse straining [J]. Energy parameter describes relation between kinematic and isotropic hardening, which can be observed during straining. Furthermore, it can assess how much anisotropy occurs in material during reverse stress. [27]

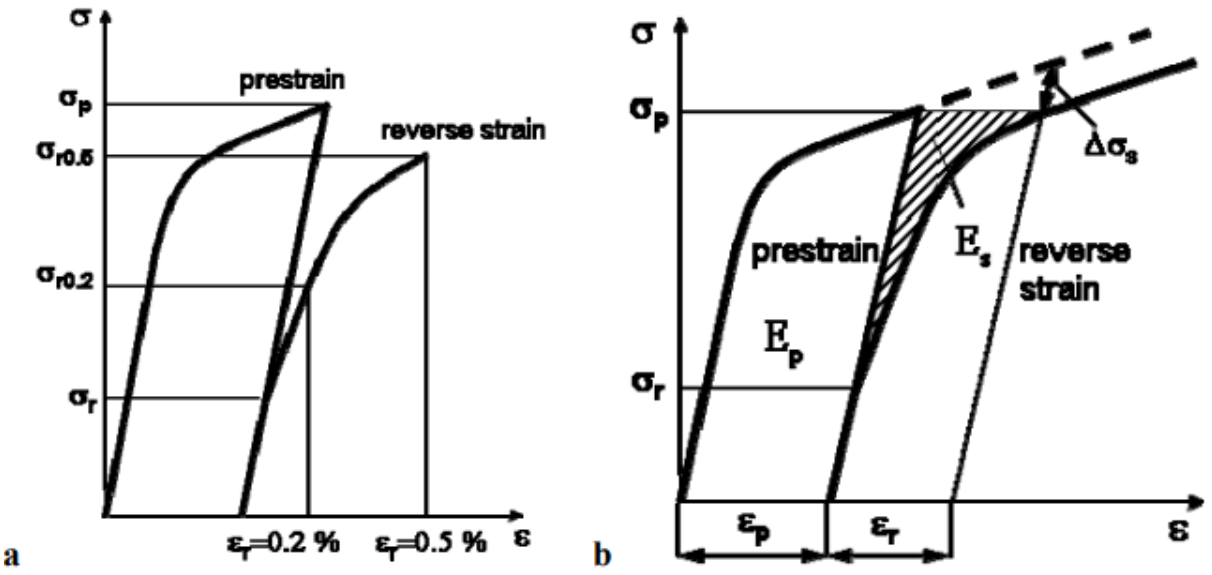

Figure 20 Stress-strain curves for a) Stress parameters of Bauschinger effect and b) strain and energy parameters of Bauschinger effect [27]

5.1.2 Causes of the Bauschinger effect

The mechanisms of the Bauschinger effect are based on two primary theories, internal stress theory and Orowan (back stress) theory.

5.1.2.1 *Internal stress theory*

Internal stress theory is established on 3 assumptions:

- The material consists of particles of very small volume, with ideal stress-strain curve
- Yield strength of individual particles is not equal
- The absolute value of yield strength of any particle does not depend on load direction during neither compression nor tension

According to these assumptions the theory says that the original stress-strain curve changes at the boundary of the elastic-plastic deformation. While the deformation during the loading is homogeneous, in case of the plastic deformation the stress distribution is not equal. Therefore, residual stresses occur after unloading, which are responsible for the decrease in yield strength during reverse loading. The result of these stresses is the reduction of the fatigue life. [27, 30]

5.1.2.2 *Orowan theory*

Dislocations, moving during forward loading, interact with other crystallographic defects (precipitates, other dislocations, grain boundaries, twin boundaries etc.), preventing their further spread. These interactions generate back stress which is contained in the area of contact and oppose further spread of other similarly oriented dislocations. During reverse loading this generated back stress repels dislocations from the crystallographic defects in the direction of reverse loading. Therefore, back stress helps to move dislocation in the direction of reverse loading which decreases yield stress by the value of the back stress. In line with the Orowan theory, increase in density of dislocations increases the number of locations where dislocations could interact, which increases the amount of back stress. Therefore, the impact of the Bauschinger effect should be higher in the materials with higher density of dislocations, but with the increase in density of dislocation, the amount of moving dislocations can decrease. This happens due to build-up of moving dislocations and their subsequent immobilization. Concentrations of stress in the area around dislocations causes plastic deformations crossing the slip planes. Moving dislocations interact on these planes with clusters of dislocations, forming Lomer-Cotrell junctions (stationary dislocation, which restricts movement of other dislocations in respective planes). This prevents accumulated dislocations moving back after unloading. Even with increase in density of dislocations it is possible to expect a maximum in the Bauschinger effect and then subsequent decrease after some level of pre-stress. [27, 31]

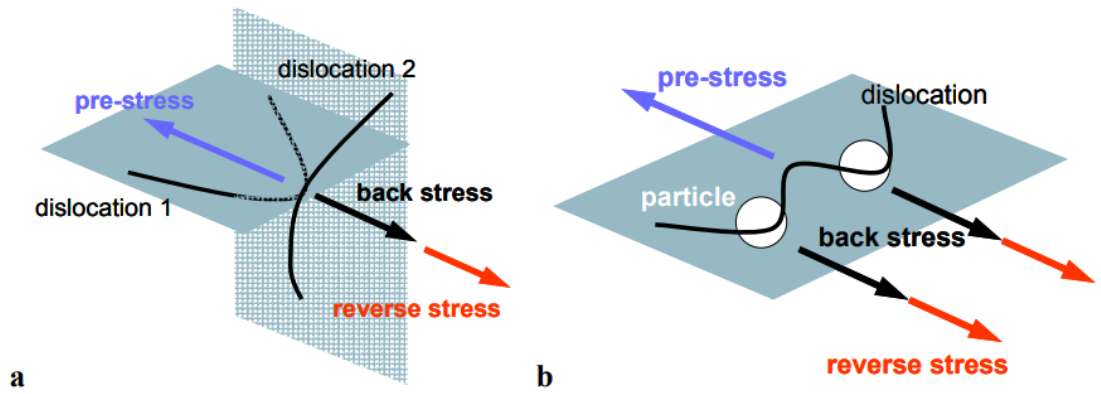

Figure 21 Interaction between a) two dislocations, b) dislocation and particles [27]

5.2 Tension-compression asymmetry in magnesium alloys

Magnesium alloys, due to their low asymmetry, produce number of deformation textures during plastic deformation process (fibre texture in extruded Mg alloys and plate texture in rolled Mg alloys). The occurrence of these deformation textures in magnesium alloys often leads to tension-compression asymmetry, which causes compression yield stress to be only half or three quarters of the tensile yield stress along the extrusion (ED) or rolling direction (RD). To describe the extend of the tension-compression asymmetry a CYS/TYS or TCA parameter is used. It describes the ratio between compression yield stress (CYS) and tension yield stress (TYS). [34]

Extensive studies on this topic showed that high frequency of twinning under basal texture, which occurs in magnesium alloy at low strain level, and load direction are the main reasons behind tension-compression asymmetry. Kleiner and Uggowitzer observed this tension-compression asymmetry in extruded AZ61 alloy [35]. Barnet et al. observed the difference of yield stress and twinning activity in rolled AZ31 alloy by channel die compression tests along different load directions, and also observed that strain hardening rate, compression yield stress and twinned grain fraction change significantly with grain size [36]. Wang et al. observed the origin of tension-compression asymmetry in different twinned grain fractions at various grain sizes, by conducting uniaxial tension and compression test on AZ31 alloy of various grain sizes prepared by ECAP processing method, followed by conventional extrusion and annealing [37]. Grain size and load direction are therefore two main elements influencing the tension-compression asymmetry, which are needed to be examined. [34]

Although, texture and grain size are usually affected simultaneously during plastic processing (forming process, extrusion etc.), it is necessary to investigate them separately to clarify the nature of tension-compression asymmetry in processed magnesium alloys. By subjecting test specimens to tension-compression deformation along different load directions, the effect that orientation of the texture has on tension-compression yield asymmetry can be investigated without interference of grain size. [34]

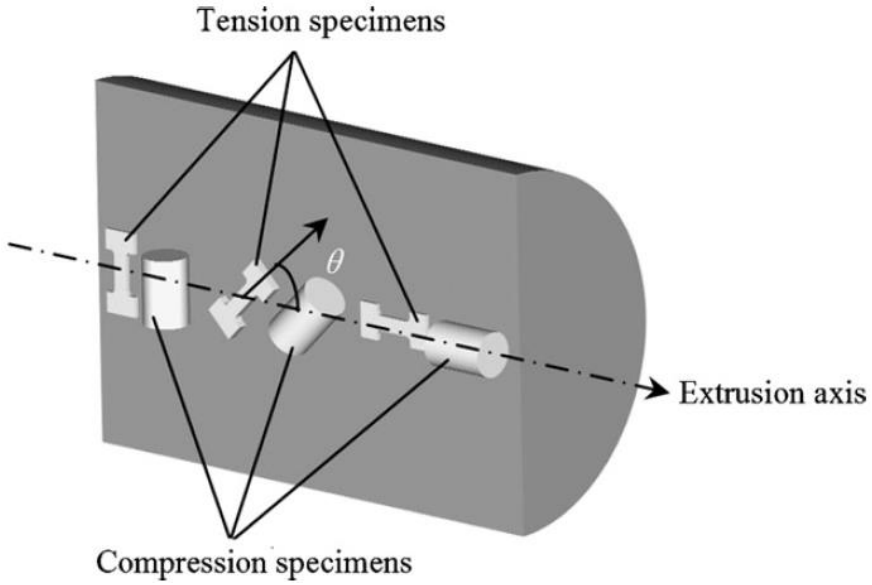

Figure 22 Scheme of test specimens taken from rolled or extruded bar, under different load angles [34]

5.3 The influence of grain size and load direction twinning and subsequently tension-compression asymmetry in AZ31

Previously conducted studies and experiment on the topic of tension-compression asymmetry (by D.L. Yin et al.) came up with specific methods for the examination of tension-compression asymmetry. It is necessary to separate the two main factors, which are responsible for the existence of twinning in magnesium alloys, texture, and grain size, to properly examine the effects on twinning process. The examination of the effects of texture on extruded magnesium alloy with predetermined grain size can be carried out by changing load direction relative to extrusion direction, thus avoiding the effects of varying grain size entirely. Therefore, compression and tension test specimens are prepared from extruded bar along three angle 0°, 45°, 90° relative to the extrusion axis. [Figure 22] Basal texture of wrought Magnesium alloys does not change after annealing at temperatures lower than 450°C. Therefore, the effects of grain size on tension-compression asymmetry can be examined using test specimens prepared along the extrusion axis and annealed to different grain size. [34]

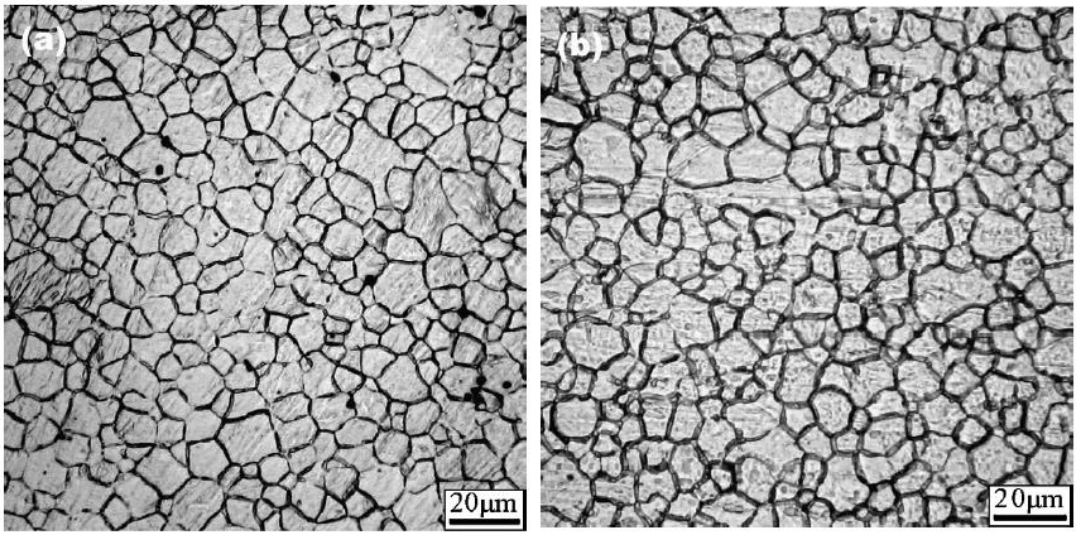

Figure 23 Microstructure of a) transverse section and b) longitudinal section of extruded AZ31 magnesium allot [34]

Tests concluded by D.L. Yin et al. on extruded magnesium alloy AZ31 show clear findings. Examination of test specimens with angle, between load direction and extrusion axis, $\theta = 0°$, parallel to the extrusion axis, brings up expected result, tension yield stress is greater that compression yield stress, thus CYS/TYS in this case equals to 0.84, which could be considered typical for extruded magnesium alloy. With the change of the angle to $\theta = 45°$, CYS/TYS in this case increases to 1.02, with tension-compression asymmetry almost disappearing. With increase of the angle to $\theta = 90°$, perpendicular to the extrusion axis, compression yield stress and tension yield stress follow this trend and switch places, with compression yield stress being far greater compare to the tension yield stress. That is indicated by the CYS/TYS, which in this case equals to 1.28. The change of CYS/TYS with the load direction show notable dependence of macro-yield properties on load direction. [Figure 24] Therefore, with consideration to the basal texture of the extruded alloy AZ31, the geometry condition and the polarity of twinning is essentially responsible for the tension-compression yield asymmetry. [34] This is supported by the change of microstructure and twinning in dependence to the load direction. Hence the dependence of twinning activity on load direction is fairly similar to that of tension and compression stresses and subsequently tension-compression asymmetry. Therefore, the notion that the dependence of the tension-compression asymmetry on the load direction is closely connected to the difference of twinning activity in characteristic basal texture of extruded AZ31 magnesium alloy is heavily supported. [Figure 24, 25]

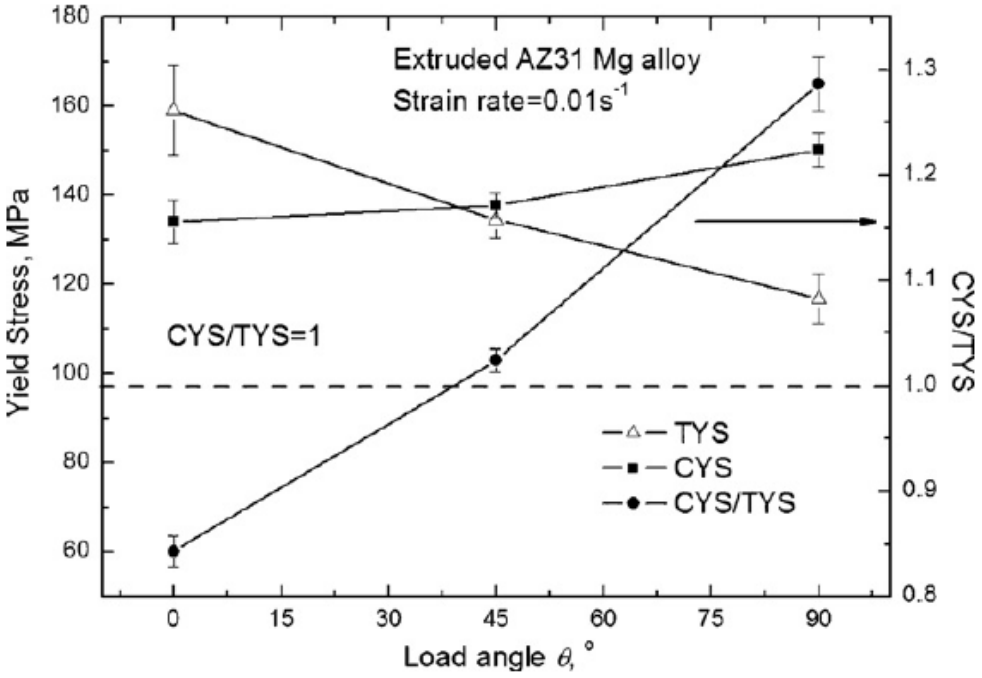

Figure 24 Diagram showing tension and compression yield stress and CYS/TYS along different load directions with constant grain size [34]

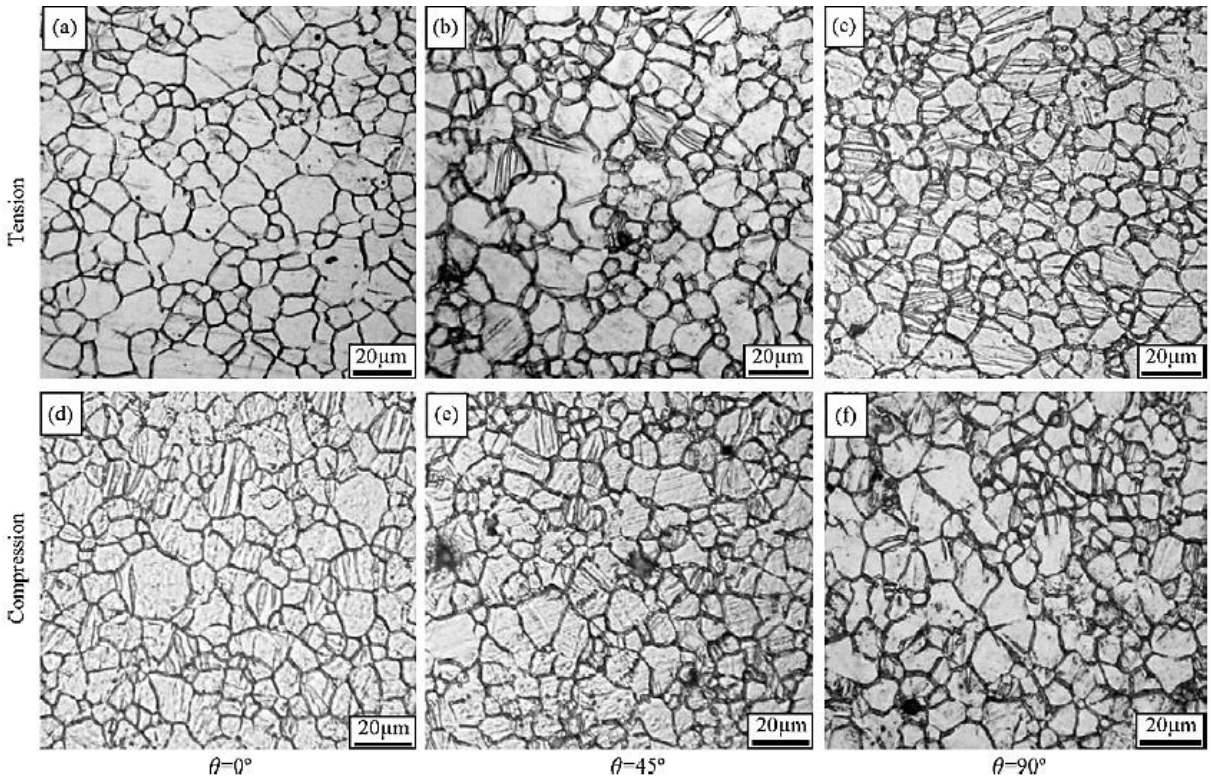

Figure 25 Difference of twinning activity in dependence on load direction [34]

Experiments exploring the dependence of the twinning stresses on different crystallographic structure proved that the twinning process has greater grain size dependence than the stress required for slip activation, which means that Hall-Petch slope of twinning k_T is greater than Hall-Petch slope of slip k_S. It is more difficult for twining process to activate at

smaller grain sizes, therefore test specimens with various grain sizes have to be prepared to investigate the effect, grain size has on tension-compression asymmetry. Tests are carried out using these specimens along the extrusion axis ($\theta = 0°$). It is proven that both compressive yield stress and tension yield stress increase with the decrease of grain size displaying obvious fine-grain strengthening.

However, the decreasing rate of compression yield stress with increasing grain size is faster than that of the tension yield stress, which is in line with the higher Hall-Petch slope of twining process than that of slip. As expected, the CYS/TYS increases with the decrease of the grain size, slightly amplifying the tension-compression asymmetry. This however could be considered rather insignificant compared to the effect of the load direction on TCA. [Figure 26] [34]

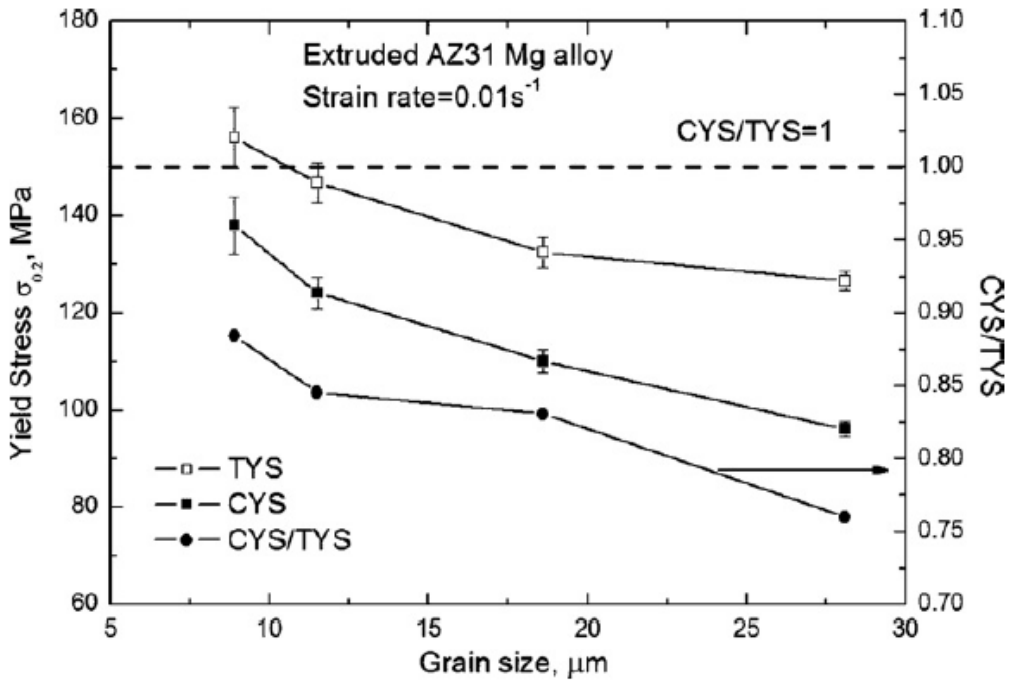

Figure 26 Diagram showing change of tension yield stress, compression yield stress and CYS/TYS with grain size [34]

Investigation of microstructure after compressive and tensile yield deformation shows that twinning rarely occurs in tension along the extrusion axis particularly at smaller grain sizes [Figure 27a], but with the increase in grain size number of twinned grains increase and exhibit the effect of grain coarsening. Whereas in compression, the twinned grain fraction and parallel twin lamellas in twinned grain notably increase with increasing grain size. However, for grain size range of 8.9 to 28 μm, obtained results point out that increase of twinning stress with decrease of grain size is most likely not enough for the transition of deformation mechanism from twinning to slip. Thus, twinning will still most likely occur across all grain sizes. It is implied that load direction has far greater influence on tension-compression asymmetry that grain size.

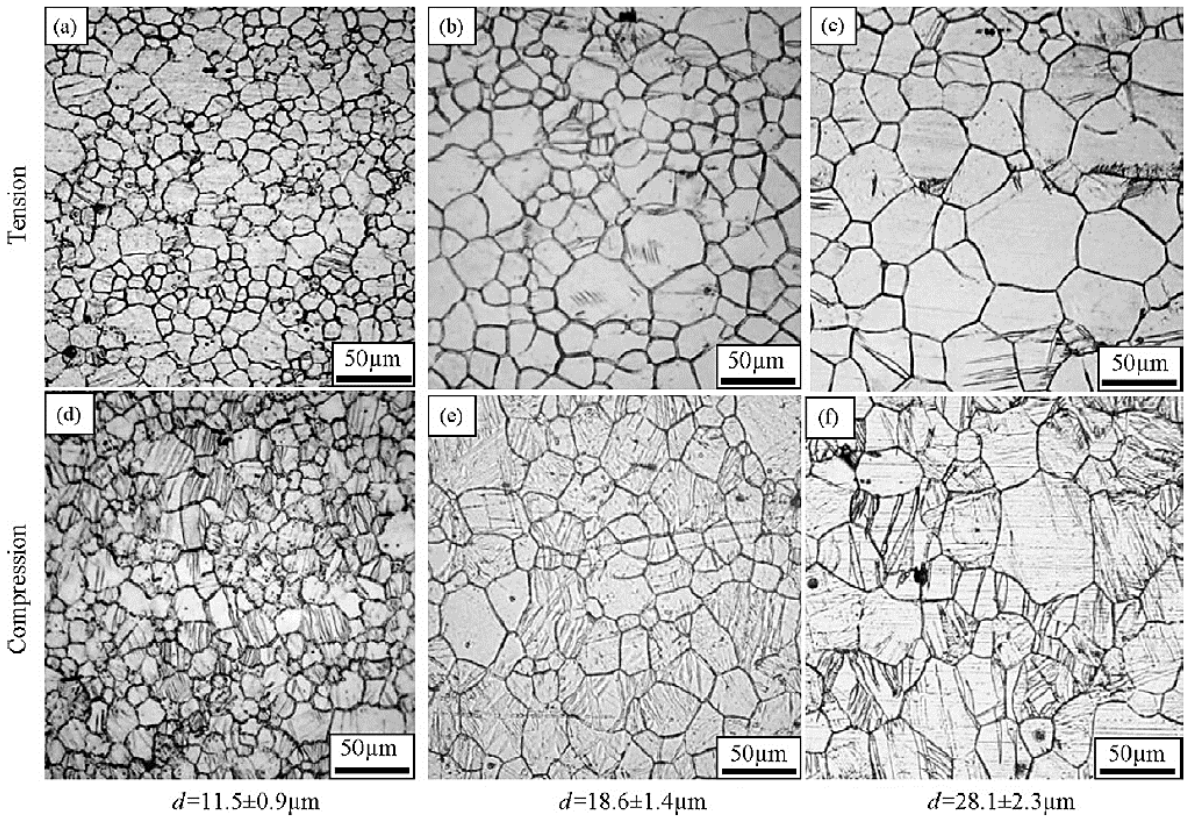

Figure 27 Microstructure of AZ31 alloy after compression and tension yield deformation at various grain sizes [34]

Furthermore, the importance of twinning during the yielding needs to be evaluated, which means that the contribution of twinning needs to be determined using quantitative statistic of twin area fraction after yielding. It was determined that twin area fractions increase with the increasing grain size for both tension and compression deformation, but at different rate. [Figure 28a] The increase in tension is quite significant compared to the compression, which demonstrates the combined effect of load direction and grain size in compression. For quantitative evaluation of the role of twinning in yielding the Brown and Agnew equation is used:

$$\varepsilon_{twin} = s\bar{m}v \quad [-]$$

where ε_{twin} is macroscopic strain accommodated by twinning along load direction, s is shear amount of $\{1\ 0\ \bar{1}\ 2\}$ twinning, $\bar{m}$ is average orientation factor of $\{1\ 0\ \bar{1}\ 2\}$ twinning system, and v is the twin volume fraction. [34, 38] In this case $\bar{m}$ of $\{1\ 0\ \bar{1}\ 2\}$ twining was determined by orientation distribution function test (ODF) to be 0.25 and replaced approximately with twin area fraction. For $\{1\ 0\ \bar{1}\ 2\}$ twinning, s is 0.13. The average orientation factor $\bar{m}$ remains constant, while ignoring the texture change during annealing. The strain applied was 2%, therefore the contribution of twining to total strain in this case is determined as:

$$f_{twin} = \frac{0.13 \times 0.25 \times v}{0.02}$$

The calculated results for various grain sizes [Figure 28b] indicate the increase of twinning contribution with grain size in both tension and compression deformation. For static grain size, the contribution of twinning in compression is far greater than in tension, and the difference increases with bigger grain size. This difference once again indicates the combined effect of load direction and grain size on twinning in compression. The twin area fraction ration is far

greater than CYS/TYS ratio, which implies a complicated relation between twin area fraction and tension-compression asymmetry, that requires further research and study. [34]

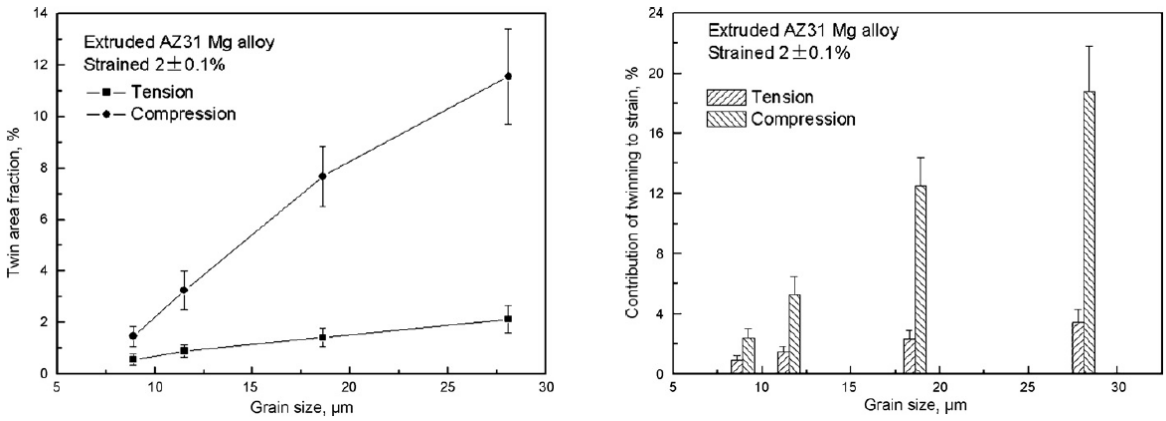

Figure 28 Diagrams showing a) change of twin area fractions with grain size and b) twinning contribution to strain at various grain sizes [34]

5.4 The effect of different extrusion processes on tension-compression asymmetry of AZ series alloys

D. Letzig et.al investigated different parameters and types of extrusion on microstructure, mechanical properties, and subsequently tension-compression asymmetry of AZ magnesium alloys. Investigated alloys with chemical composition stated in Table 5, were processed using indirect and hydrostatic process of extrusion. [Figure 29]

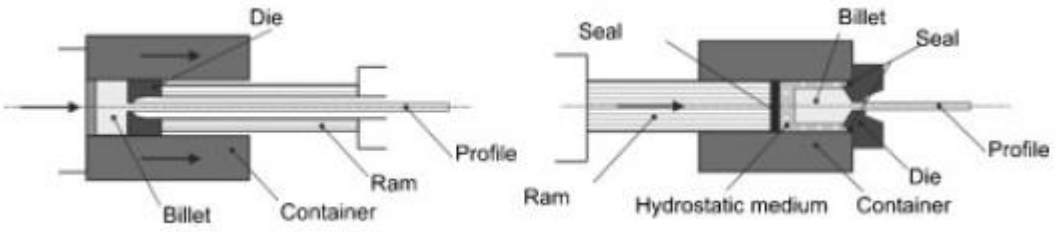

Figure 29 Schematic representation of (left) indirect extrusion process and (right) hydrostatic extrusion process [39]

Alloy	Chemical composition [wt.%]
AZ31	Mg - 2.9Al - 0.98Zn - 0.29Mn
AZ61	Mg – 6.5Al - 0.99Zn - 0.20Mn
AZ80	Mg – 8.5Al - 0.51Zn - 0.31Mn

Table 5 Table of chemical compositions of AZ magnesium alloys investigated by D. Letzig et. Al [39]

The investigation of microstructure [Figure 30] indicated that indirect extrusion process lead to average grain size of $\sim 22\mu m$ for AZ31 and $\sim 12\mu m$ for AZ61, AZ80, which suggests that higher Al content helps with the homogeneity in terms of grain size. However, processing of alloys using hydrostatic extrusion process resulted in far finer grain microstructure. With average grain size of $2 - 4\mu m$ for AZ31 and AZ61 and $6 - 7\mu m$ for AZ80. The occurrence of such fine grain microstructure could be explained by lower temperature rise in specimens during the processing. It should be noted that the grain size achieved in AZ31 and AZ61 is comparable with the grain size obtained from ECAP process. [39]

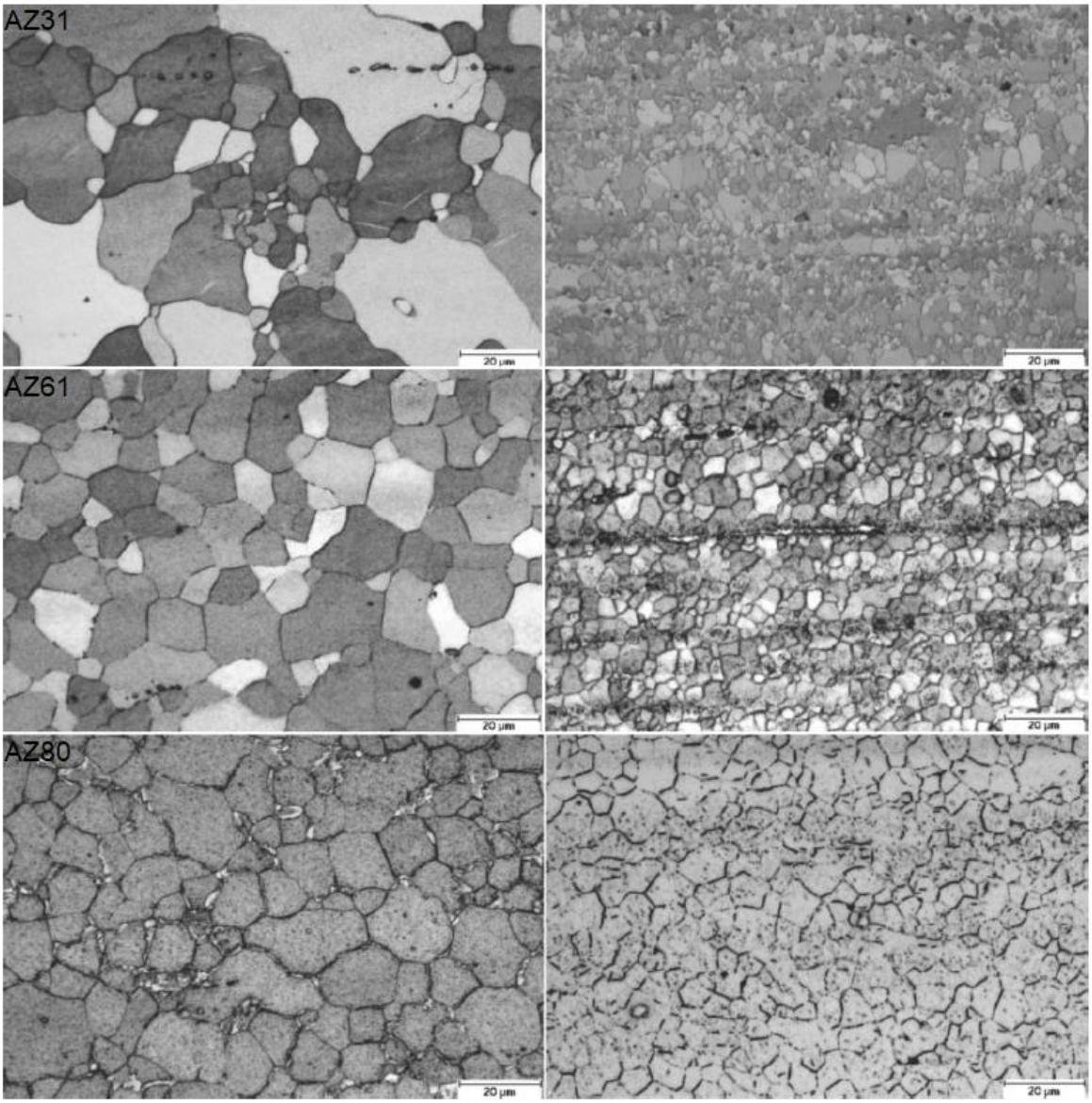

Figure 30 Microstructure of AZ magnesium alloys AZ31 (top), AZ61 (middle), AZ80 (bottom) after indirect extrusion (left) and hydrostatic extrusion (right) [39]

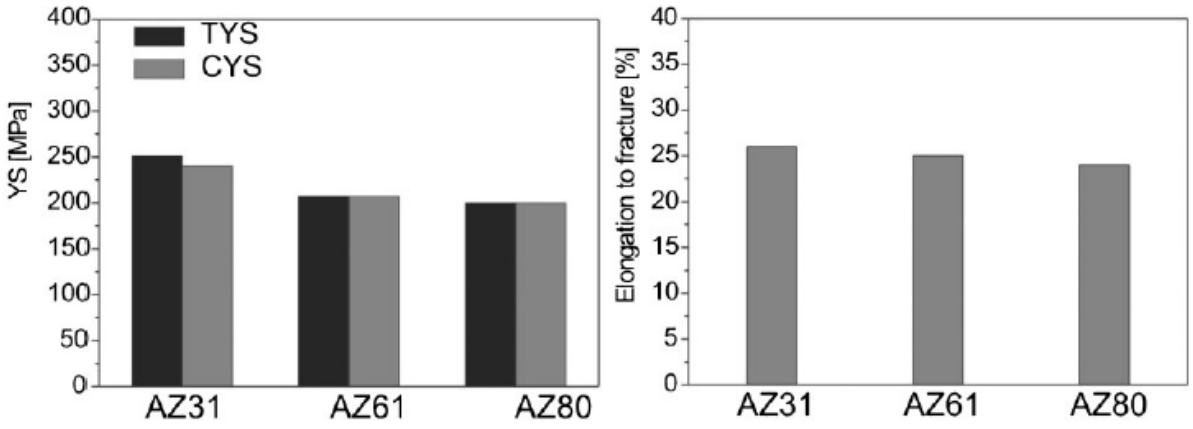

Figure 31 Tensile and compression yield strengths, and fracture elongations of AZ magnesium alloys processed using hydrostatic extrusion [39]

Tension and compression tests of AZ magnesium alloys prepared by hydrostatic extrusion, performed at room temperature, revealed that values of tensile yield strength (TYS) are very similar or just slightly higher than the values of compression yield strength (CYS). [Figure 31] Further tests investigating the influence of microstructure on asymmetry between CYS and TYS were concluded.

The stress-strain curves in tension and compression of AZ31 [Figure 32] demonstrate a significant discrepancy between AZ31 alloys extruded indirectly and hydrostatically. In this case the difference between tensile and compressive yield strength $\Delta\sigma$ of indirectly extruded AZ31 at 300°C corresponds to $\sim 100MPa$, compared to the difference of $\sim 12MPa$ for the hydrostatically extruded alloy at 100°C. This may be attributed to the suppression of the contribution of the twinning as a deformation mode in fine grained microstructures.[39]

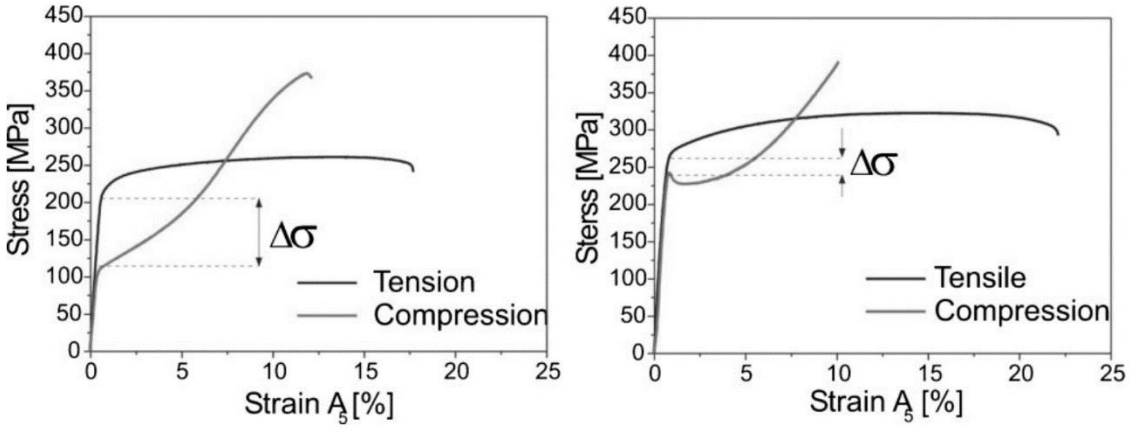

Figure 32 Stress-strain curves in tension and compression of AZ31 magnesium alloy processed by (on the left) indirect extrusion, and (on the right) hydrostatic extrusion [39]

In case of indirectly extruded AZ61 and AZ80, they discovered that the value of $\Delta\sigma$ is significantly lower than for the AZ31, thanks to the higher Al content. Comparatively hydrostatically extruded AZ61 and AZ80 exhibit the lowest values of $\Delta\sigma$ from all tested alloys. This suggests that not only grain size, but also the precipitation of $Mg_{17}Al_{12}$ may have similar effect on twinning process.[39]

5.5 The effect of multidirectional pre-compression on tension-compression asymmetry of hot rolled AZ31

S. Xu et al investigated the effect of multidirectional pre-compression on tension-compression asymmetry of hot rolled magnesium alloy AZ31. The tested material used in the experiment was AZ31 alloy sheet with a thickness of 31.5mm. From there specimens with dimension 30 x 30 x31.5 mm were prepared. The multidirectional pre-compression was performed along three direction, the rolling direction (RD), the transverse direction (TD) and the normal direction (ND). The pre-compression specimens were loaded to 100 MPa along the RD, 180 MPa along the TD and 144 MPa along the ND. After pre-compression completed, the specimens for tension and compression test were prepared from these blocks and some of them were annealed at 175°C for 14 hours in order to remove the dislocations without losing created twin structures. Specimens that were not annealed were denoted as MP (multi-directionally pre-compressed), and annealed specimens were denoted as MPA (multi-directionally pre-compressed and annealed). [40]

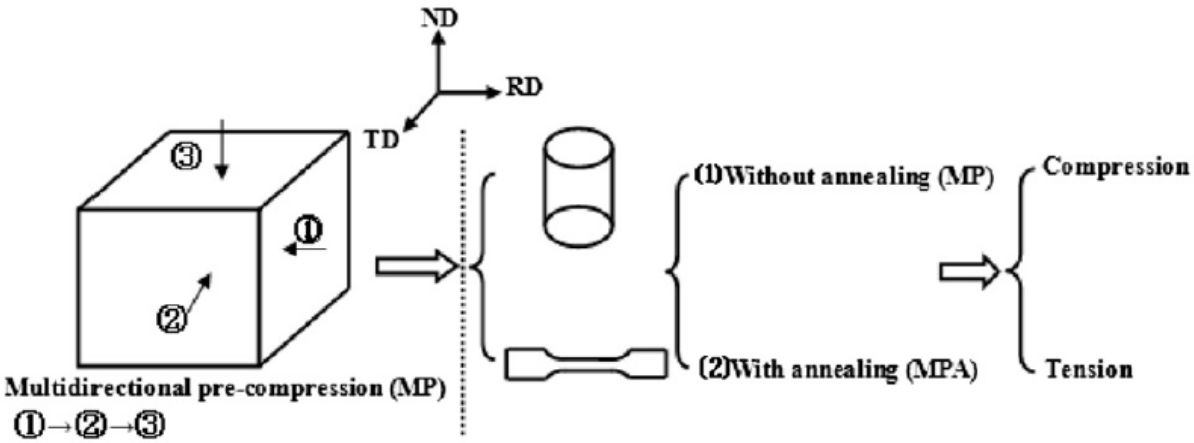

Figure 33 Schematic representation of preparation process of tensile and compressive specimens [40]

Tension and compression tests indicate that extension twinning is present when tension is parallel to c-axis or when compression is perpendicular to c-axis. It is implied by the presence of yield plateau, which is typical feature of extension twinning, in both tension and compression. [Figure 34]

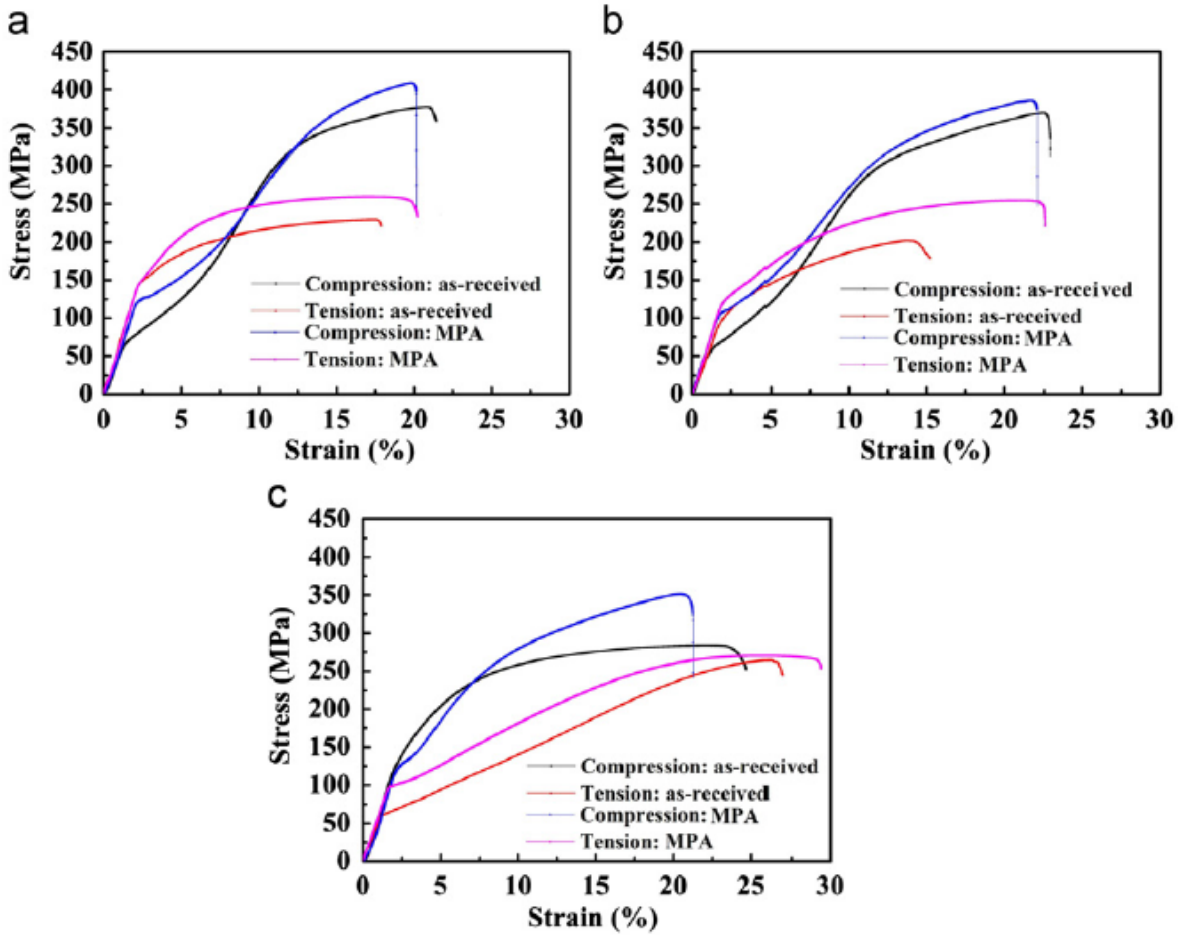

Figure 34 Stress-strain diagrams of as-received and MPA samples in compression and tension along a) RD, b) TD, c) ND [40]

The response of MPA specimens on tension and compression loading is significantly different. While the compressive yield strength of as-received specimens is low 60 MPa and 55 MPa along RD and TD, it increases to 125 MPa and 100 MPa, respectively for MPA specimens. However, the compressive yield strength along the ND is 140 MPa, it decreases to 125 MPa for MPA specimens.

While as-received specimens display large tension-compression asymmetry, for MPA specimens this asymmetry is significantly reduced. Therefore, it is shown that multidirectional pre-compression with annealing can to certain degree mitigate tension-compression asymmetry in AZ series magnesium alloys. [Figure 34] [40]

Specimen	Rolling direction			
	As-received		MPA	
	Yield stress	Ultimate stress	Yield stress	Ultimate stress
Tension	60	375	125	405
Compression	150	220	155	250
CYS/TYS	0.4	-	0.81	-
Specimen	**Transverse direction**			
	As-received		MPA	
	Yield stress	Ultimate stress	Yield stress	Ultimate stress
Tension	55	370	100	400
Compression	105	200	128	250
CYS/TYS	0.52	-	0.78	-
Specimen	**Normal direction**			
	As-received		MPA	
	Yield stress	Ultimate stress	Yield stress	Ultimate stress
Tension	140	275	125	350
Compression	55	250	96	265
CYS/TYS	0.39	-	0.77	-

Table 6 Table depicting values from stress-strain diagrams [Figure 33] for all three directions [40]

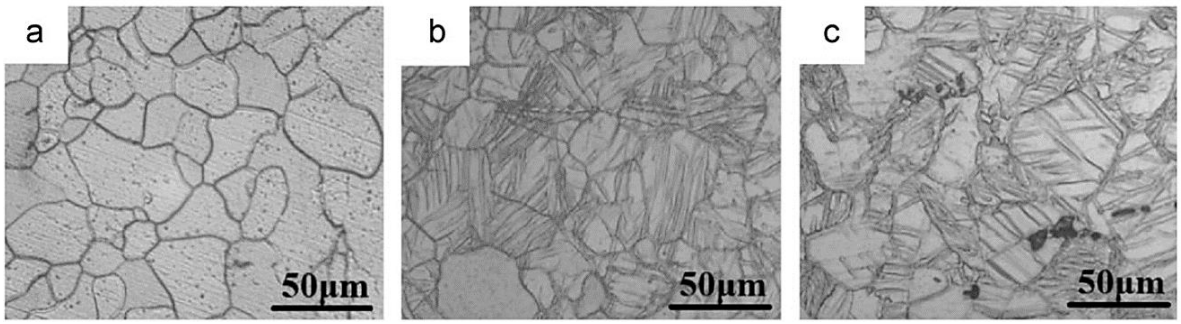

Figure 35 Microstructure of a) as-received specimen, b) MP specimen, and c) MPA specimen [40]

Further investigation of MPA specimens through EBSD revealed the presence of $\{1\ 0\ \bar{1}\ 2\}$ extension twinning proving the assumption made from the shape of the stress-strain diagrams. It was observed in RD [Figure 36e] that twin lamellae created during first compression were twinned again, as they were in favourable orientation during recompression.

Therefore, twins (T_{RD}, T_{TD}, and $T_{RD\text{-}TD}$) created during multidirectional pre-compression further modify the behaviour of the specimens during further deformation. Analysis of the in situ EBSD show that $\{1\ 0\ \bar{1}\ 2\} - \{1\ 0\ \bar{1}\ 2\}$ double twins can be created in previously formed $\{1\ 0\ \bar{1}\ 2\}$ twins and already existing $\{1\ 0\ \bar{1}\ 2\} - \{1\ 0\ \bar{1}\ 2\}$ double twins could be de-twined back to $\{1\ 0\ \bar{1}\ 2\}$ twins under better and more favourable orientation [Figure 36, 37]. [40]

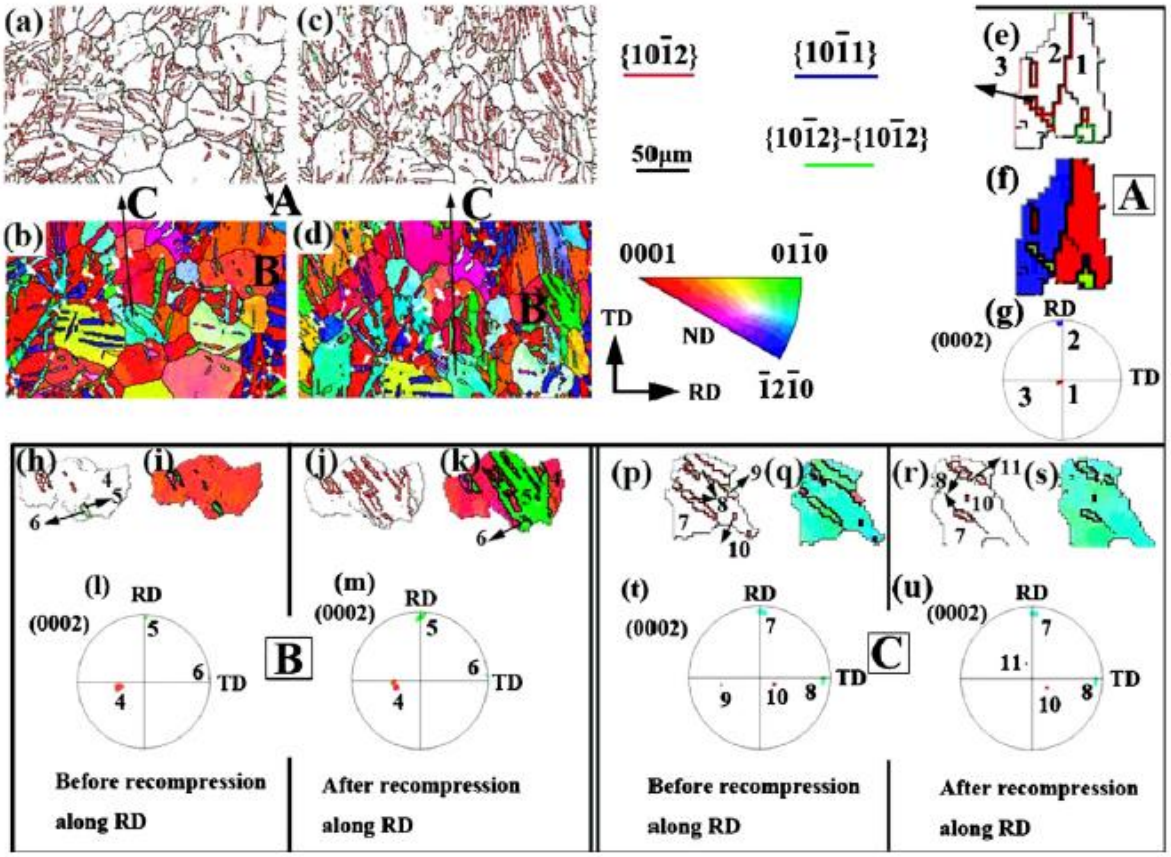

Figure 36 In situ EBSD observation of MPA specimen a) and b) before recompression along RD and, c) and d) after recompression along RD [40]

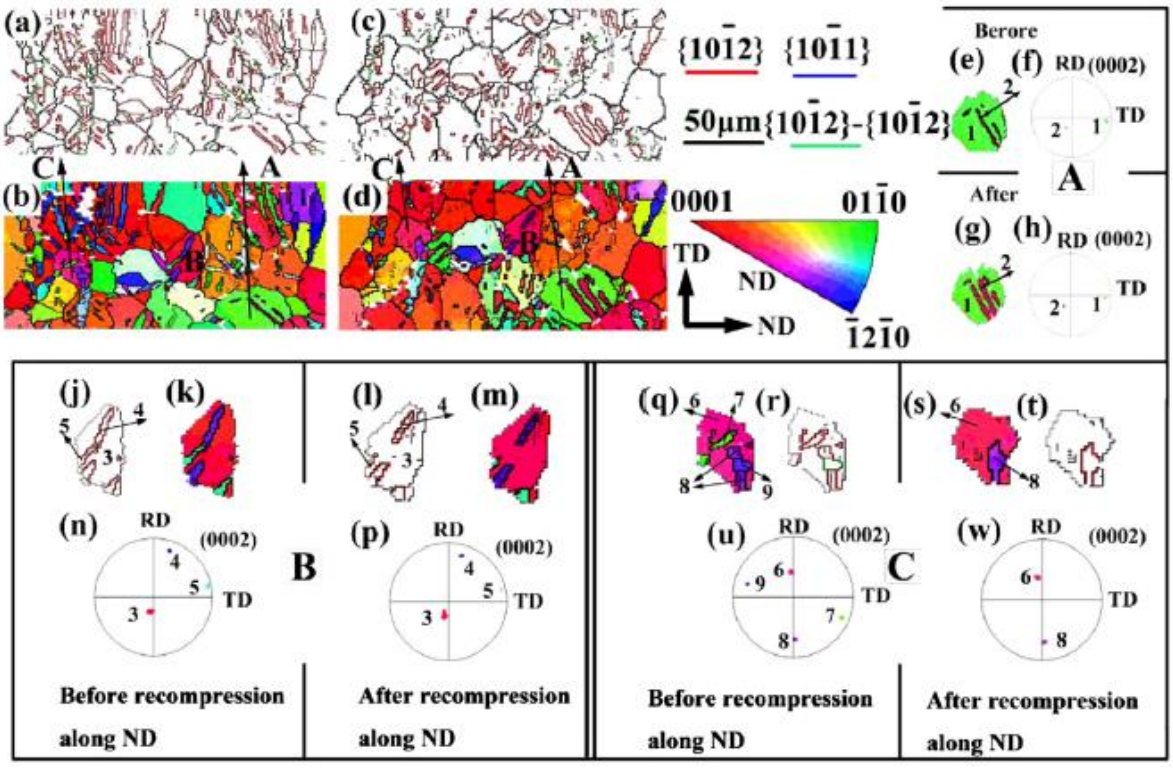

Figure 37 In situ EBSD observation of MPA specimen a) and b) before recompression along ND and, c) and d) after recompression along ND [40]

5.6 Influence of temperature and strain rate on tension-compression asymmetry of extruded AM30 magnesium alloy

Z. Zachriah et.al investigated the effect of temperature and strain rate on tension-compression asymmetry of wrought AM30 magnesium alloy. The tests were performed for various temperatures T ranging from 25°C to 400°C, and for various strain rates $\dot{\varepsilon}$ ranging from $10^{-2}s^{-1}$ to $10s^{-1}$. [41]

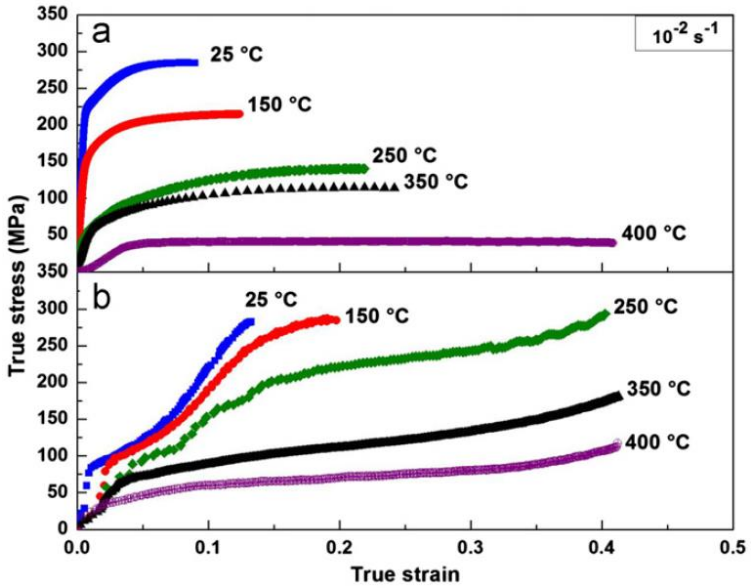

Figure 38 True stress-strain curves in a) tension and b) compression of extruded AM30 alloy at various temperatures, but at fixed strain rate $10^{-2}s^{-1}$ [41]

Temperature	Strain rate	Tension				Compression
		$\sigma_{y,t}$ [MPa]	n [-]	ε_f [%]	$\sigma_{u,t}$ [MPa]	$\sigma_{y,c}$ [MPa]
25°C	10^{-2} s^{-1}	210.2	0.04	9.4	274.1	104.6
	10^{-1} s^{-1}	222.2	0.01	8.9	284.5	116.4
	10^{0} s^{-1}	236.7	0.12	12.8	317.9	116.9
	10^{1} s^{-1}	246.6	0.2	13.6	339.02	116.03
150°C	10^{-2} s^{-1}	145.8	0.02	14.1	214.3	89.1
	10^{-1} s^{-1}	158.2	0.01	12.3	214.7	92.7
	10^{0} s^{-1}	179.7	0.13	10.6	243.9	90.9
	10^{1} s^{-1}	194.6	0.13	10.5	243.8	101.3
250°C	10^{-2} s^{-1}	75.1	0.3	12.4	183.3	66.9
	10^{-1} s^{-1}	70.2	0.01	21.8	140.5	65.8
	10^{0} s^{-1}	101.8	0.1	16.7	156.5	89.6
	10^{1} s^{-1}	139.1	0.04	15.4	183.2	90.3
350°C	10^{-2} s^{-1}	60.3	0.1	24.4	107.1	60.3
	10^{-1} s^{-1}	64.7	0.02	24.4	114.7	62.3
	10^{0} s^{-1}	65.6	0.14	17.5	97.4	64.9
	10^{1} s^{-1}	78.0	0.14	18.1	124.7	76.5
400°C	10^{-2} s^{-1}	40.4	0.01		42.6	39.0
	10^{-1} s^{-1}	53.9	0.06		77.2	51.1
	10^{0} s^{-1}	61.0	0.4	37	103.3	53.5
	10^{1} s^{-1}	63.6	0.2	37	104.7	53.8

Table 7 Table of mechanical properties from tension and compression tests at various temperatures and strain rates [41]

Results of tension and compression tests at various temperatures with fixed strain rate, $\dot{\varepsilon} = 10^{-2}\ s^{-1}$, are depicted in Figure 37 and values from all remaining tests for various strain rates and temperatures of mechanical properties are listed in Table 7.

From the stress-strain diagrams and listed mechanical properties it is obvious that with rising temperature the tensile yield strength $\sigma_{y,t}$, and work hardening exponent n decreases, while strain to fracture ε_f increases. While tension stress-strain diagrams have concave-downward shape as expected for any ductile material, stress strain diagrams in compression have concave-upward shape. This occurrence of concave-upward shape has been reported and attributed to the $\{1\ 0\ \bar{1}\ 2\}$ twinning deformation.[41]

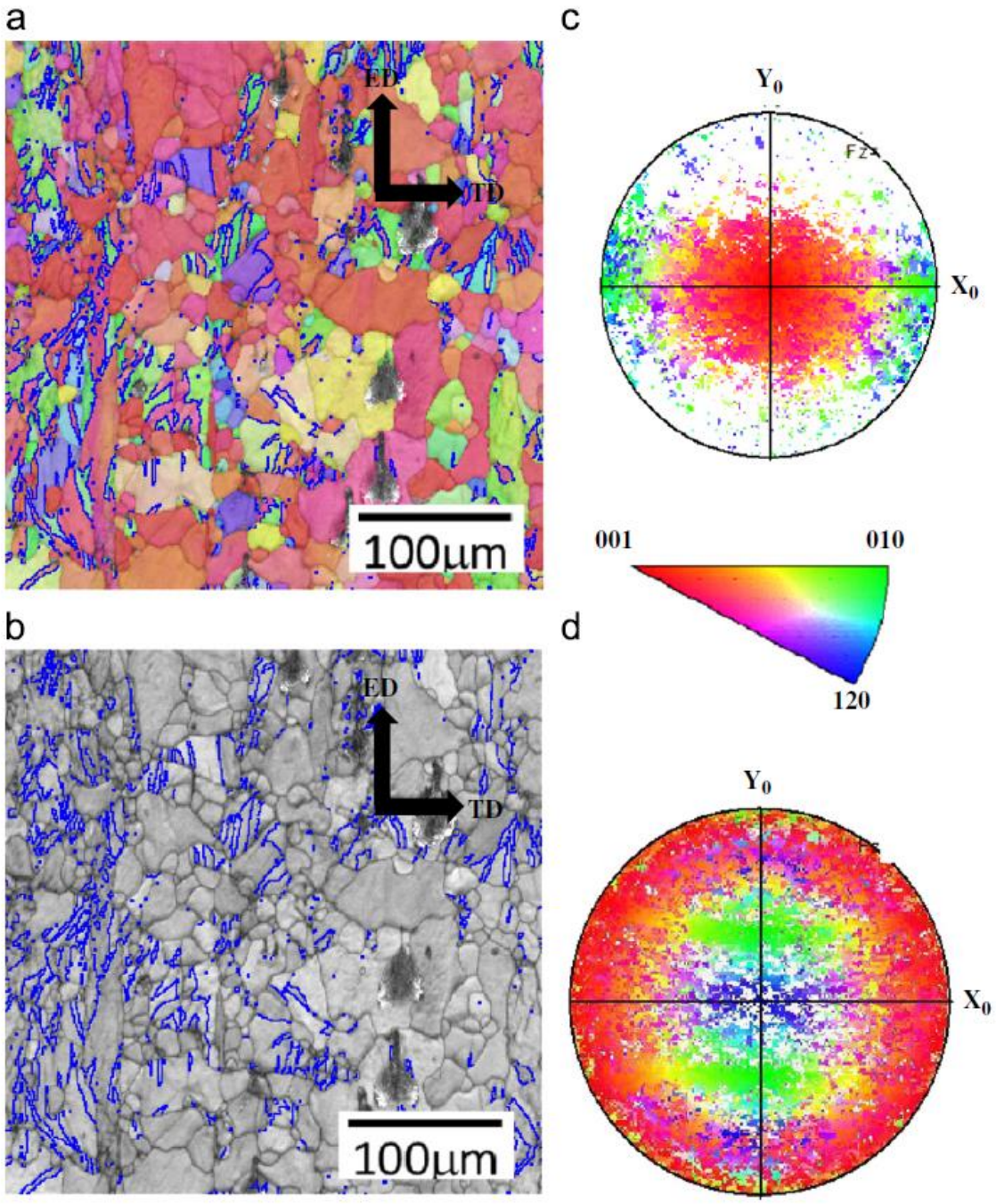

Figure 39 a) Inverse pole figure map, b) image quality map, and c) {0001} pole figure of alloy is as-received state. ED - extrusion direction, and TD - transverse direction [41]

5.6.1 Influence of temperature

Furthermore, changes of tensile yield strength $\sigma_{y,t}$ and compressive yield strength $\sigma_{y,c}$ with changing temperature for all four strain rate depicted in Figure 40a, reveal noticeable decrease in $\sigma_{y,t}$ with increasing temperature compared to the minor decrease of compressive yield strength $\sigma_{y,c}$ with increasing temperature. However, values of $\sigma_{y,t}$ and $\sigma_{y,c}$ are approximately similar at $T \geq 250°C$. The extent of tension-compression asymmetry, depicted as $\sigma_{y,t}/\sigma_{y,c}$ (TYS/CYS), as a function of temperature is portrayed in Figure 40b. The highest value of tension-compression asymmetry is at room temperature, whilst for the most case TCA almost completely disappears at $T = 350°C$. [41]

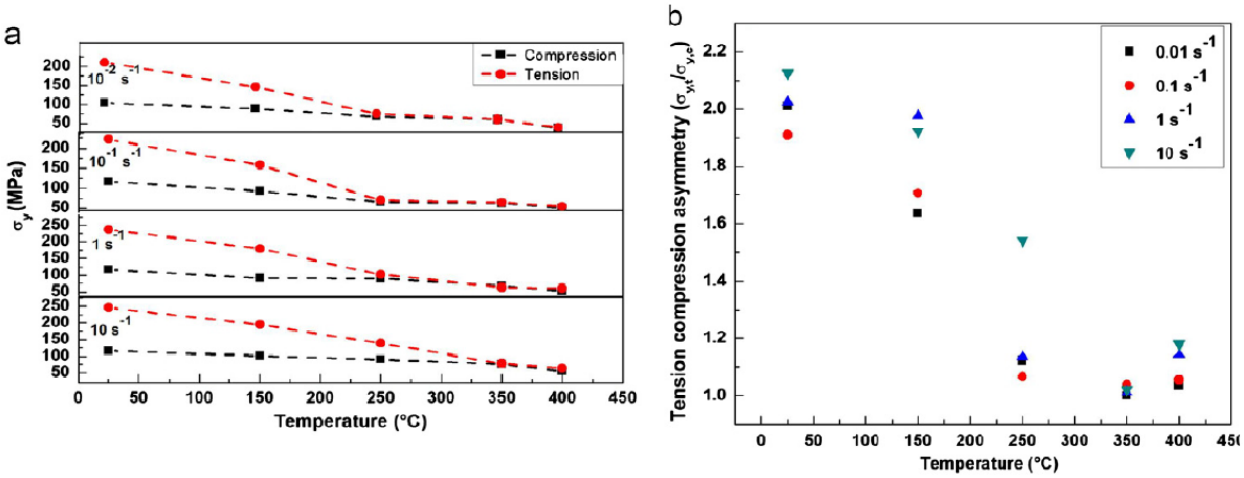

Figure 40 a) Change of tensile and compressive yield strengths with temperature for various strain rates, and b) Tension-compression yield asymmetry (TYS/CYS) as a function of temperature [41]

5.6.2 Influence of strain rate

Changes of tensile yield strength $\sigma_{y,t}$ and compressive yield strength $\sigma_{y,c}$ with changing strain rate for all testing temperatures does not seem to be overly significant, as depicted in Figure 41a. With the exception of strain rate $\dot{\varepsilon}$ = 10 s^{-1} at temperature $T = 250°C$. Although, sudden increase in TCA ($\sigma_{y,t}/\sigma_{y,c}$) at strain rate $\dot{\varepsilon}$ = 10 s^{-1} suggests that certain combinations of $T - \dot{\varepsilon}$ have a role in tension-compression asymmetry after all. [41]

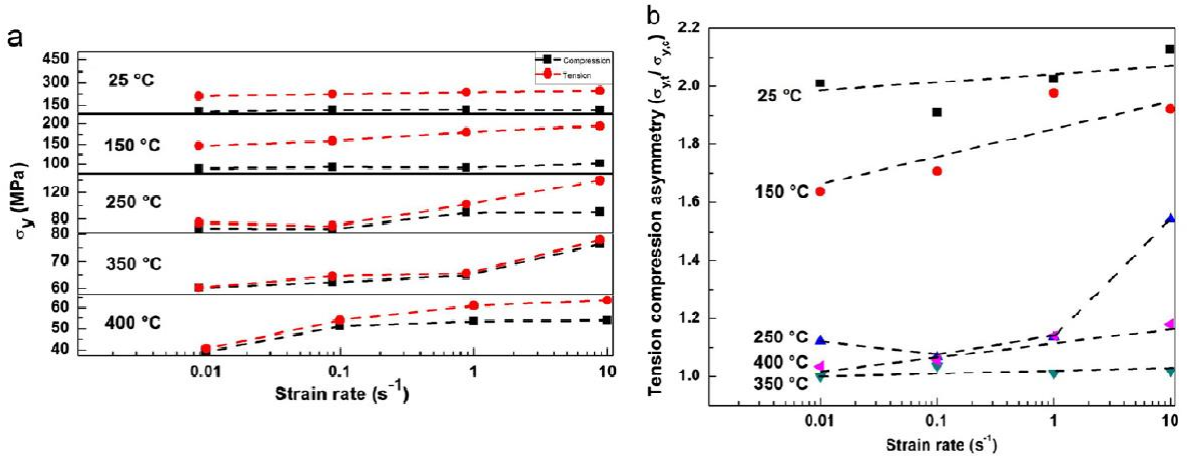

Figure 41 a) Change of tension and compression yield strength with strain rate ate different temperatures, and b) Tension-compression asymmetry as a function of strain rate [41]

To determine strain rate dependence of flow stress, strain rate sensitivity, m, was evaluated using following equation:

$$\sigma = K(\dot{\varepsilon})^m \quad [MPa]$$

Where K is a constant, $\dot{\varepsilon}$ is strain rate, m is strain rate sensitivity and σ is stress applied. Variants of m with changing temperature for tension and compression is noted in Figure 42 (strain rate used in these computations is $\dot{\varepsilon} = 10\%$). Maximum value of m is only ~0.1, which means that strain rate sensitivity in the AM30 magnesium alloy is rather low. Low values of strain rate sensitivity in magnesium alloys were already reported by Korla and Chonkshi [42], who were evaluating strain rate sensitivity from strain rate jump test during compression testing of AZ31. [41]

It is noteworthy that values of m increase with temperature in compression, starting with 0 at room temperature, while m decreases with temperature in tension. In both tension and compression values of m reach plateau at $T = 250°C$ [Figure 42]. [41]

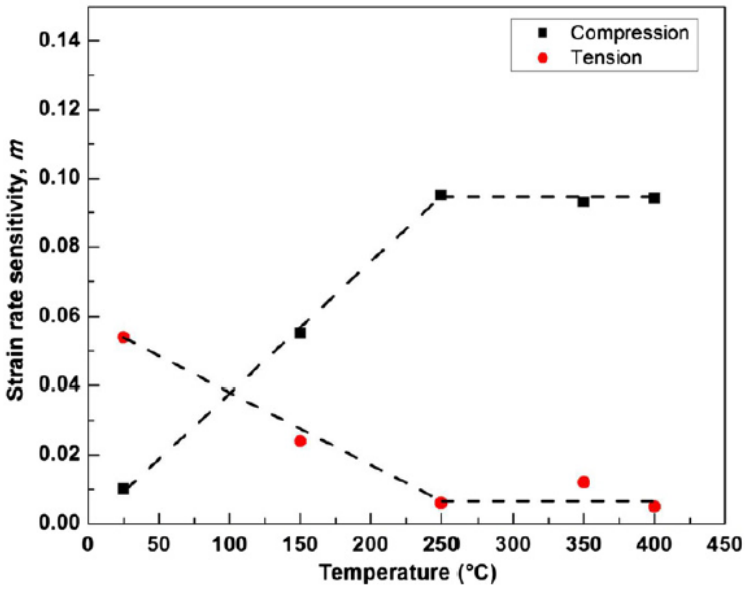

Figure 42 Variants of m (strain rate sensitivity) with changing temperature in tension and compression [41]

Results indicate that magnesium alloy AM30 displays quite significant tension-compression asymmetry that is sensitive to both temperature and strain rate for most of their combinations. It should be noted that these tests investigating TCA were performed just in extruded direction (ED), therefore in this case the effect of basal slip can be neglected due to low Schmidt factor on basal planes for both tension and compression.

Further analysis of microstructure suggested that bellow critical temperature $\sim 250°C$, prevalently $\{1\,0\,\bar{1}\,2\}$ twinning in combination with non-basal slip in tension, and $\{1\,0\,\bar{1}\,2\}$ twinning in compression occurs, leading to different microstructure. These deformation mechanisms are responsible for the presence of the significant TCA bellow critical temperature $\sim 250°C$. While above critical temperature $\sim 250°C$ significant recrystallization process occurs resulting in almost complete negation of TCA. Even at higher temperatures ($150°C$ and $250°C$ in this specific case) the TCA was significant at higher strain rates, suggesting that twin fractions created were strain rate dependent. [41]

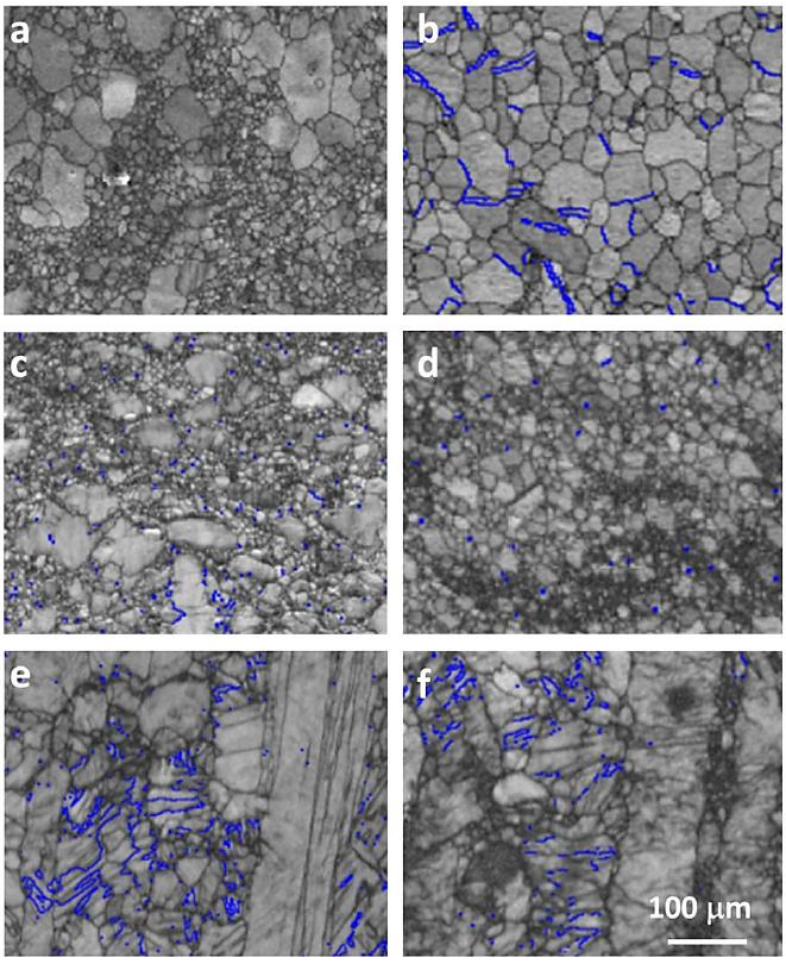

Figure 43 Image quality maps from tensile and compressive specimens deformed a) and b) at 400°C, c) and d) at 250°C, and e) and f) at 25°C, where specimens a), c) and e) were tested at $10^{-1}s^{-1}$ and b), d) and f) were tested at $10s^{-1}$ [41]

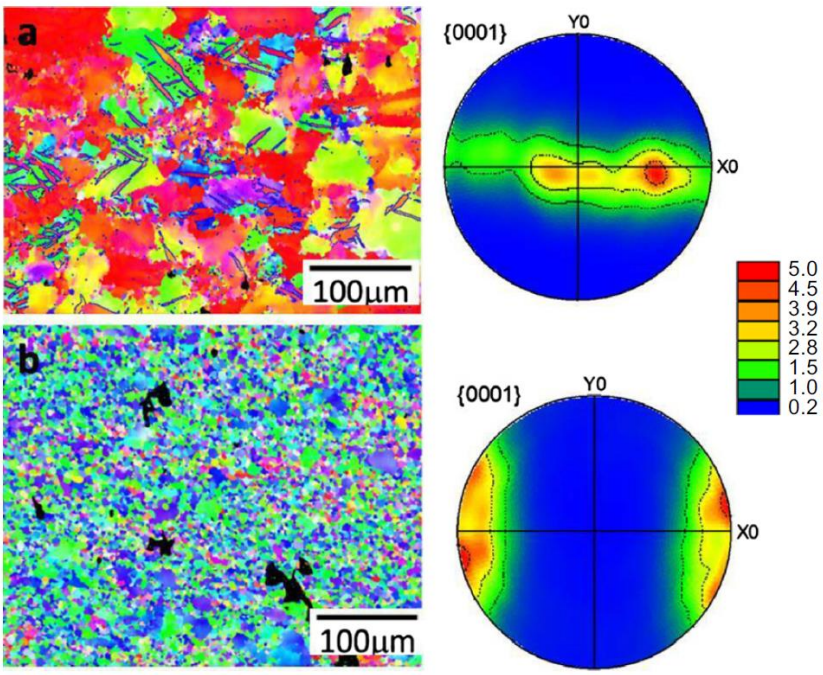

Figure 44 Inverse pole figure map and {0001} pole figure of the alloy after a) tensile and b) compressive testing at 350°C with strain rate $10^{-2}s^{-1}$ [41]

5.7 The effects of equal channel angular pressing on grain refinement

Magnesium alloys are due to their low density, high specific strength and good castability in high demand for industrial and technological applications (mainly in automobile and aerospace industries). However low ductility of magnesium and its alloys at room temperature somewhat limit their industrial applications. Effective way to improve mechanical properties of magnesium alloys is grain refinement. By using severe plastic deformation technique (SPD), ultrafine-grained materials can be produced. SPD technique is based on the principle of introducing extremely large strain during deformation process. One of the most widely used and most effective methods is equal channel angular pressing (ECAP), which can prepare magnesium alloys with excellent mechanical properties. [43]

5.7.1 Principles of equal channel angular pressing (ECAP)

During processing, the specimen, with cross-section and appropriate dimensions is extruded through an ECAP device consisting of input and output channels intersection at the angle Φ to form one solid extrusion channel. The outer shape of the intersection of input and output channels is described by the angle of curvature of the external arc Ψ. There are several ways of connecting both channels depending on the choice of angles Φ and Ψ, whose values affect the degree of deformation of the processed materials [Figure 45]. In case of high-strength materials, extrusion is carried out at higher temperatures. [46]

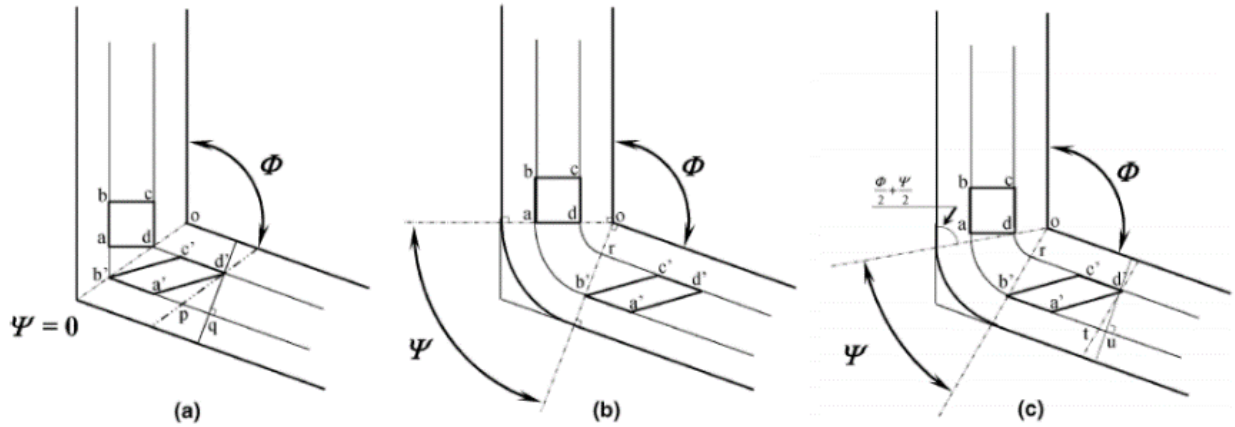

Figure 45 Different ways to connect an extrusion channel a) Ψ=0°, b) Ψ=Π-Φ, c) Ψ∈(0°;Π-Φ) [44]

During each pass, the specimen is subjected to shear strain. The magnitude of the strain can be analytically calculated using formulas which are closely related the configuration of the ECAP channel. Therefore, if the angle of curvature of the external arc is Ψ=0° and angle Φ is arbitrary, then for one pass of the specimen through the ECAP channel, the value of the shear strain increment is given by: [46]

$$\frac{F}{R_e} = \Delta\varepsilon_i = \frac{2}{\sqrt{3}} \cdot \cot\left(\frac{\Phi}{2}\right)$$

where F is force applied on the specimen and R_e is yield strength of the specimen. The value of the total equivalent strain after the Nth pass ε_N is:

$$\varepsilon_N = \frac{2N}{\sqrt{3}} \cdot \cot\left(\frac{\Phi}{2}\right)$$

A generalized formula for equivalent strain for variable angles Φ and Ψ of ECAP channels for N passes:

$$\varepsilon_N = \frac{N}{\sqrt{3}} \cdot \left[2\cot\left(\frac{\Phi}{2} + \frac{\Psi}{2}\right) + \Psi \operatorname{cosec}\left(\frac{\Phi}{2} + \frac{\Psi}{2}\right)\right]$$

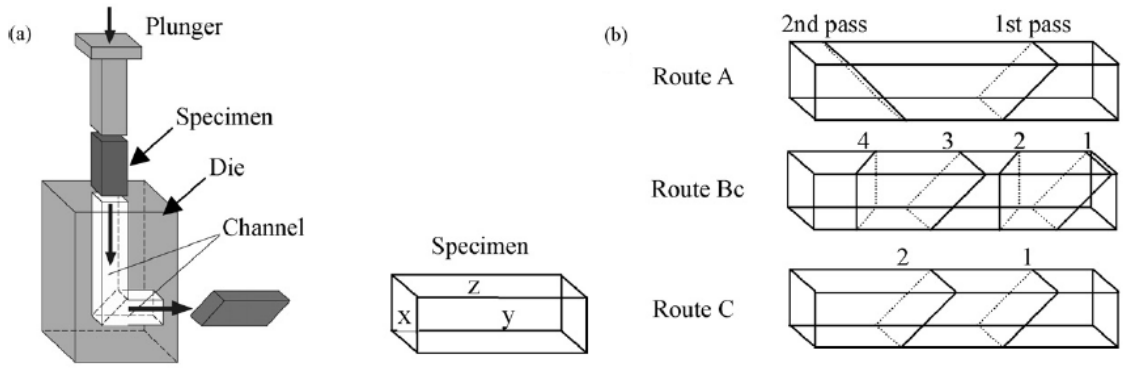

Figure 46 a) Schematic representation of ECAP process, b) ideal shear plane in different routes [43]

The advantage of the ECAP method is possibility of repeated passes of the processed specimens, which leads to higher strain and better grain refinement. Certain change of orientation of the specimens between individual passes has also an effect on resulting UFG (ultrafine-grained) structure. Therefore, four basic processing routes were developed [Figure 47]:

- Route A, the specimen is pressed without any rotation between passes.
- Route B_A, the specimen is rotated 90° in an alternate direction between passes.
- Route B_C, the specimen is rotated 90° in counter-clockwise between each pass.
- Route C, the specimen is rotated 180° between passes.

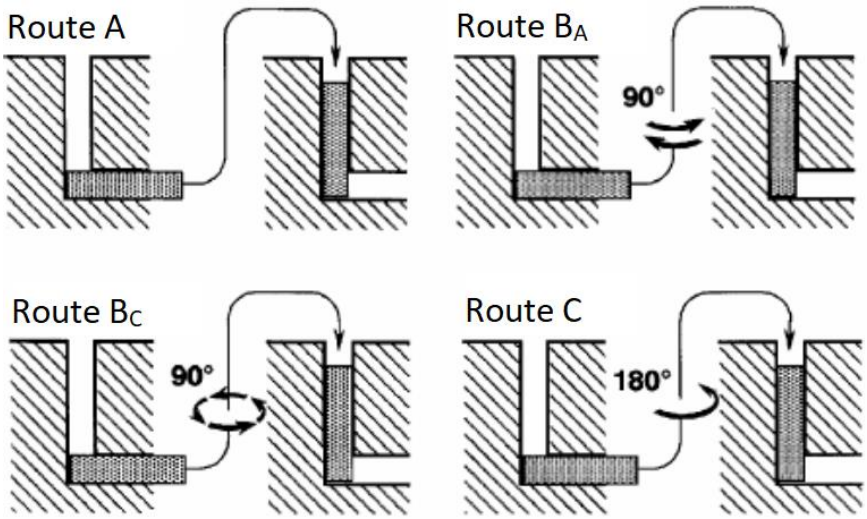

Figure 47 Four basic processing routes for ECAP [45]

5.7.2 Experimental determination of effects of the ECAP on magnesium alloy

The study performed by L.B. Tong et al., investigating the influence of different ECAP routes on microstructure and mechanical properties of magnesium alloy Mg-Zn-Ca alloy and concluded with these results: [43]

1. Use of different ECAP routes to process Mg-Zn-Ca alloy resulted in observation of different microstructures across used methods. Therefore, the quality of grain refinement depends on used ECAP route. Route B_C proved to be the most effective and Route A was shown to be the least effective in grain refinement (Table 8). [43]
2. Use of different ECAP routes resulted in texture evolution that can be derived from corresponding strain paths.

a. Route A induced a basal texture with most {0 0 0 2} planes parallel to the extrusion direction and transverse direction. [43]
b. Route B_C induced texture with maximum density of {0 0 0 2} pole figure locating at 36° to extrusion direction, the texture was rotated about 15° around the axis of shear direction. [43]
c. Route C induced the strongest texture with {0 0 0 2} plane inclining about 45° to extrusion direction. [43]

3. Use of Routes A and B_C resulted in increase of tensile yield strength, however, use of route C resulted in decrease of tensile yield strength compared to the unprocessed alloys. The decrease was a result of the clash between the strengthening effect from the grain refinement and texture softening effect. However, the effect of processing routes of ECAPed specimens on microhardness was not significant [Figure 48]. [43]

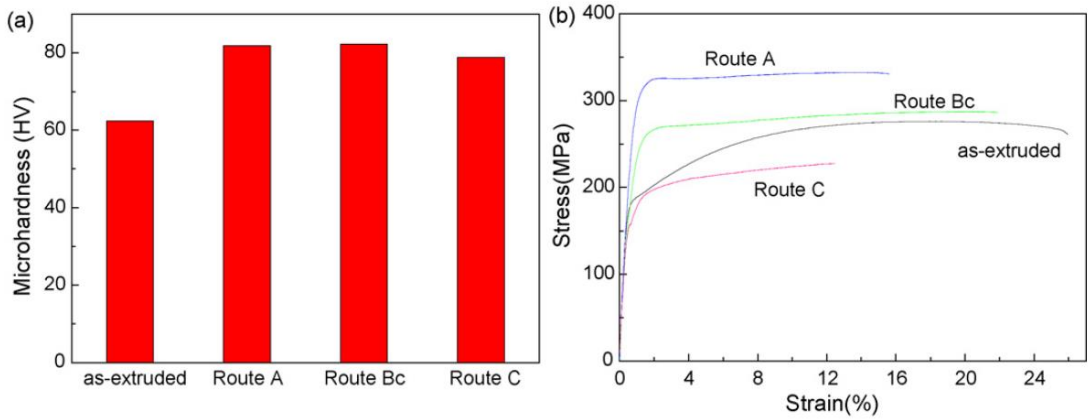

Figure 48 Comparison of mechanical properties of as-extruded and ECAPed Mg-Zn-Ca alloy a) microhardness and b) tensile stress-strain curves [43]

	Grain size [μm]	Tensile Yield strength [MPa]	Ultimate tensile strength [MPa]	Elongation [%]
As-extruded	3.9	178	276	25.9
ECAP-Route A	1.0	246	332	15.5
ECAP-Route B_C	0.7	180	287	21.9
ECAP-Route C	0.8	131	228	12.6

Table 8 Table of tensile properties of as-extruded and ECAPed Mg-Zn-Ca alloy [43]

6 Experimental determination of tension-compression asymmetry, results, and discussion

6.1 Metallographic examination

Samples were acquired from extruded AZ61 magnesium alloy rod in transverse and longitudinal section to better examine the microstructure created by the extrusion process. Samples were mounted into thermoset housing using metallographic press OPAL X-Press 2 [Figure 53] using following parameters:

Pressure	250 bar
Heating time	10 minutes
Heating temperature	180°C
Cooling time	4 minutes

Table 9 Parameters of sample mounting

Figure 49 Mounting press Opal X-press 2 [51]

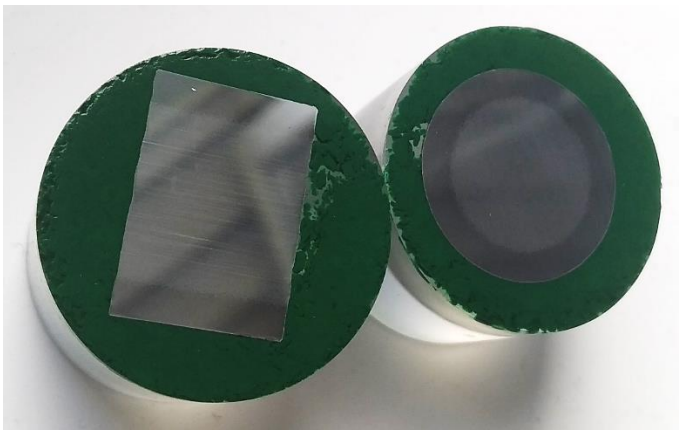

Figure 50 Mounted metallographic samples in L section (on the left), and T section (on the right)

Mounting process was followed by the grinding using Struers Pedemin grinding and polishing machine [Figure 55] on grinding papers with various surface roughness. As magnesium alloys are fairy soft, use of overly rough grinding papers was not necessary. Therefore, P800, P1200, P2400, P4000 grinding papers were used to prepare these samples. Each grinding phase lasted 2 minutes at 125 rpm, after which grinding paper was changed for finer one.

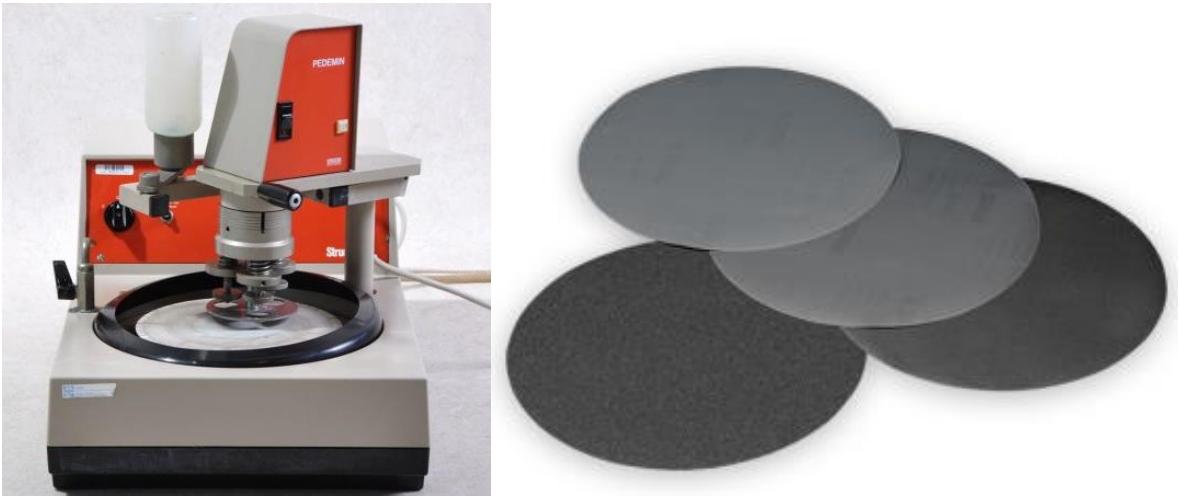

Figure 51 Struers Pedemin grinding and polishing machine (left) and Struers grinding papers (right) [52, 53]

Samples were polished using two polishing pads with surface roughness of $3\mu m$ and $1\mu m$, with appropriate diamond polishing paste, first in machine and then in hand to reach optimal and fine surface finish, both at 250 rpm

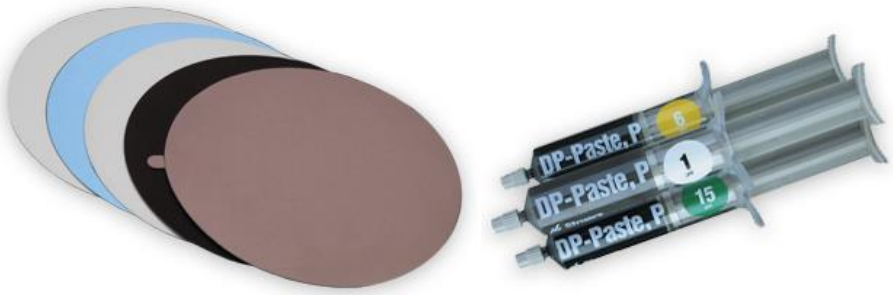

Figure 52 Struers polishing pads (left) and diamond polishing paste (right)

Samples were then etched using solution with following chemical composition:

Volume [ml]	Volume fraction [vol.%]	Component
1.0	1.0%	Nitric Acid
17.0	17.0%	Distilled Water
32.0	32.0%	Acetic Acid
50.0	50.0%	Ethylene Glycol

Table 10 Chemical composition of etching solution

Optical microscopy then revealed the difference in grain size between the edge and the core of the sample, with core having far finer grain. It also revealed some directionality of the microstructure in the longitudinal section caused by the extrusion process. That was noticeable from the overall distribution of grain and precipitates throughout the structure. [Figure 57] However, grains themselves did not indicate any form of directionality (deformed and elongated grains along the extrusion direction), which could be expected in extruded alloy. This was probably caused by the dynamic recrystallization during the extrusion process. Additionally, throughout the microstructure, the intermetallic phase $Mg_{17}Al_{12}$ was equally spread out on the edge of the grains. [Figure 53-60]

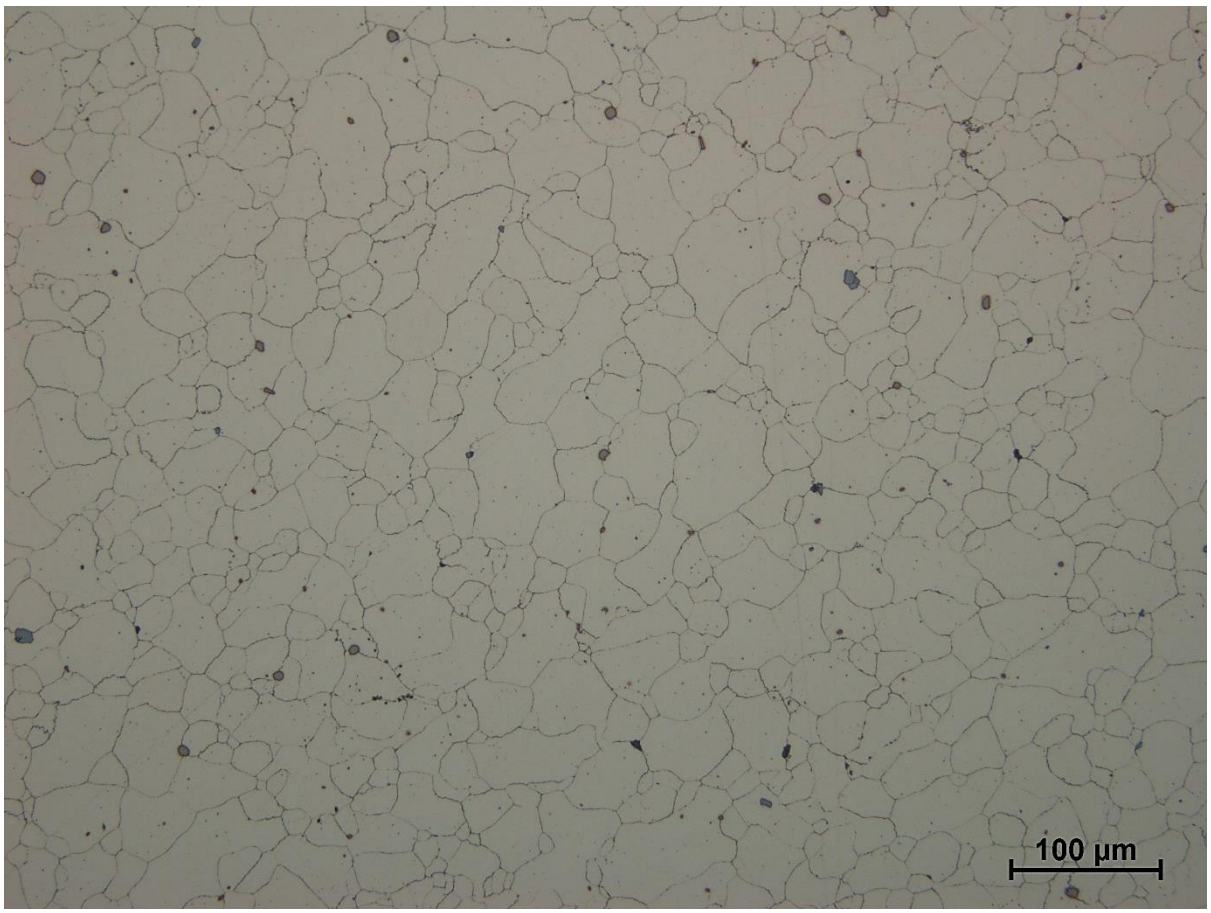

Figure 53 Microstructure of AZ61 in Transverse section at 200X magnification (edge of the sample, courser grain)

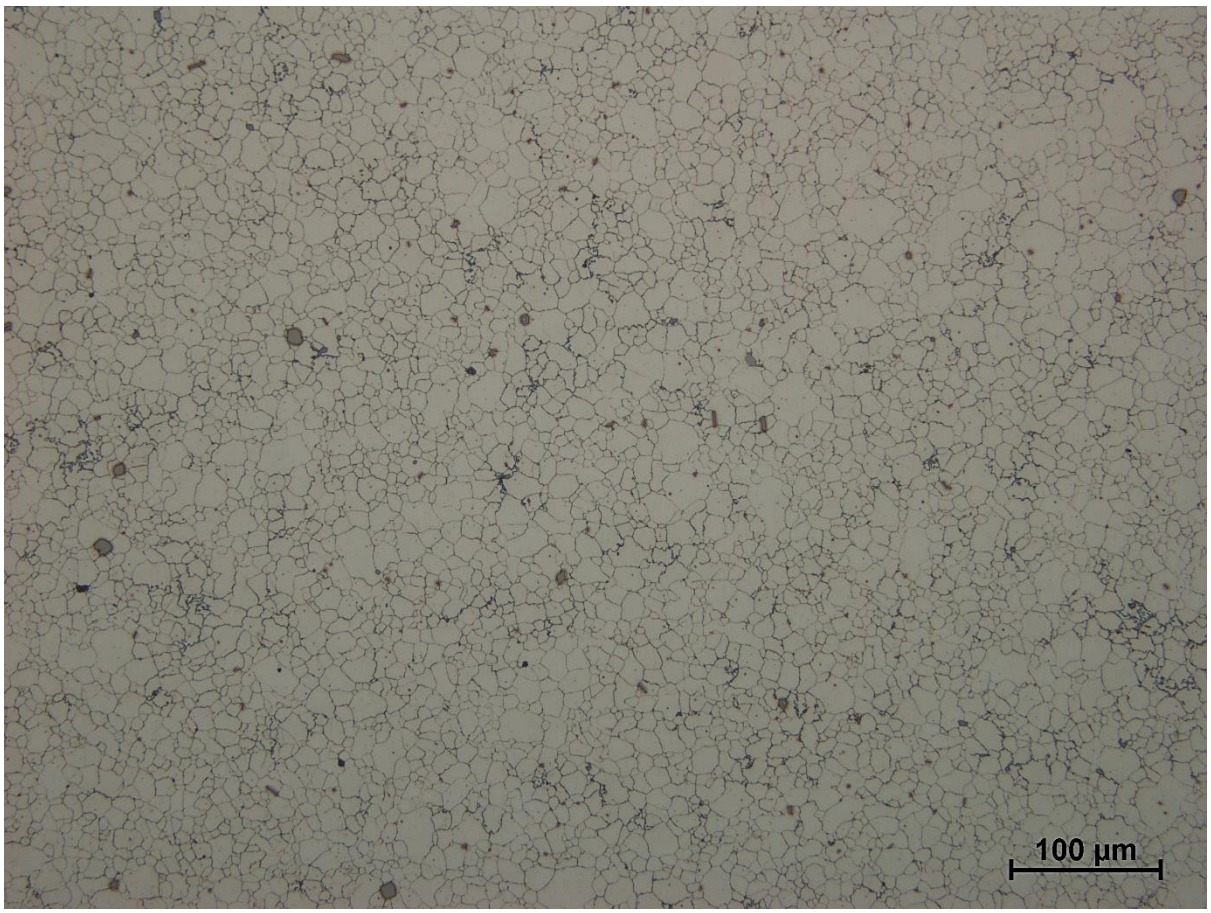

Figure 54 Microstructure of AZ61 in Transverse section at 200X magnification (middle of the sample, finer grain)

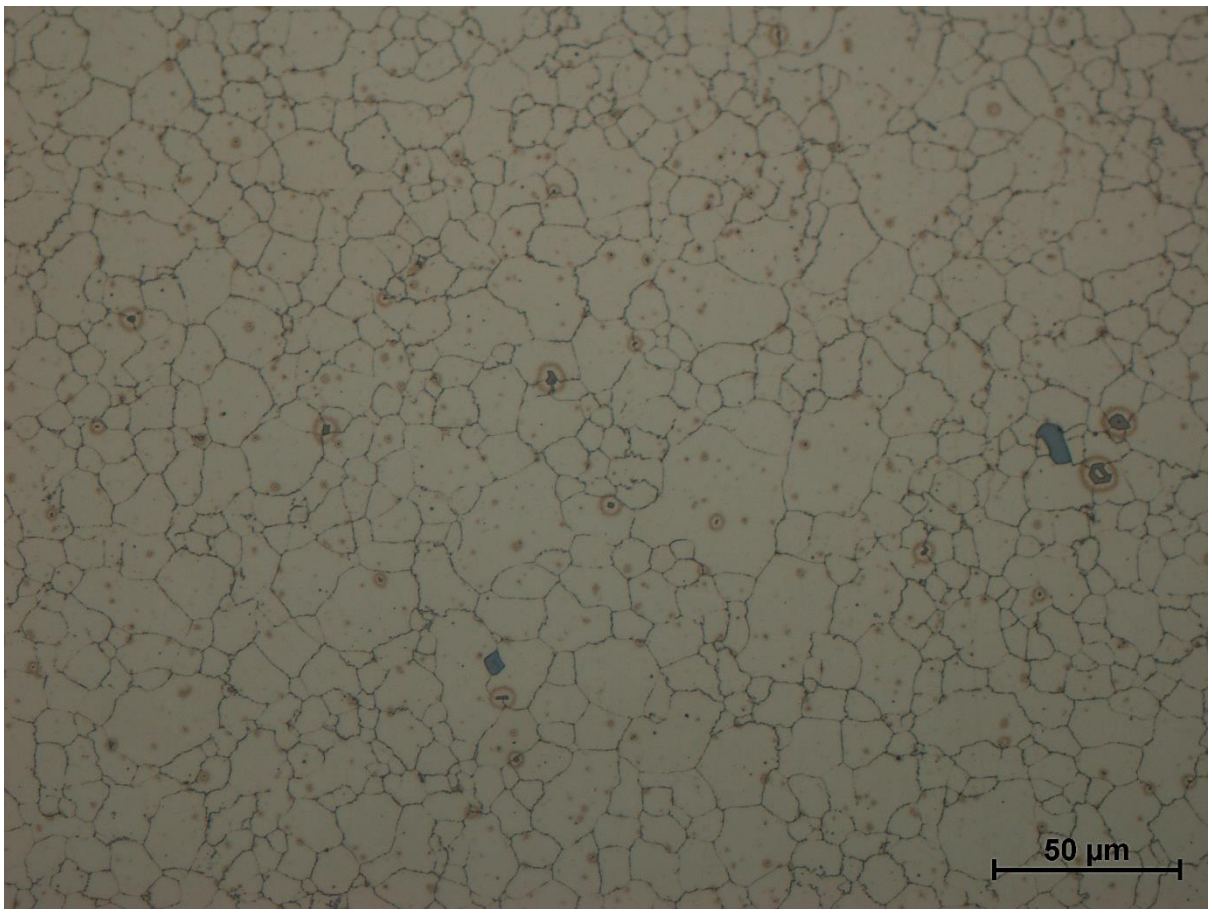

Figure 55 Microstructure of AZ61 in Transverse section at 500X magnification

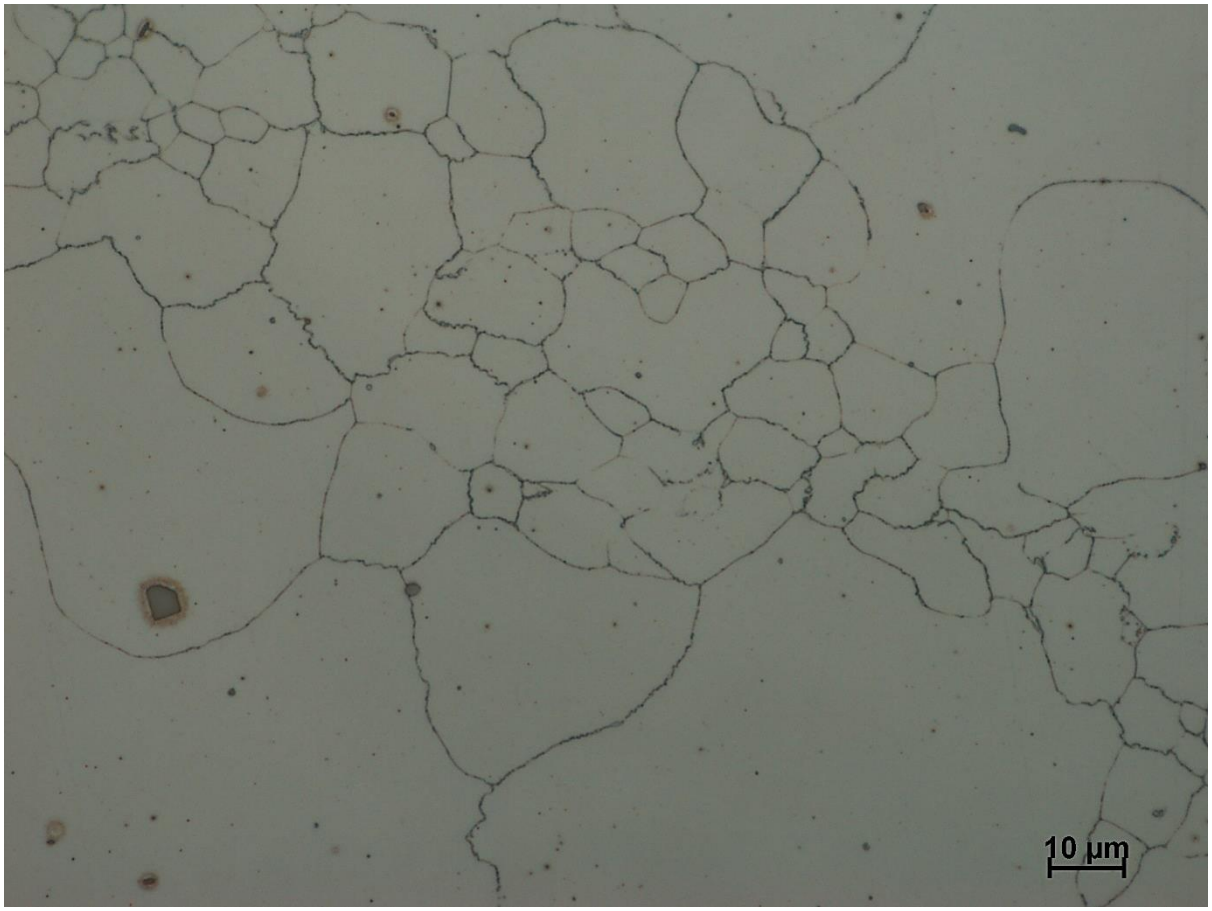

Figure 56 Microstructure of AZ61 in Transverse section at 1000X magnification

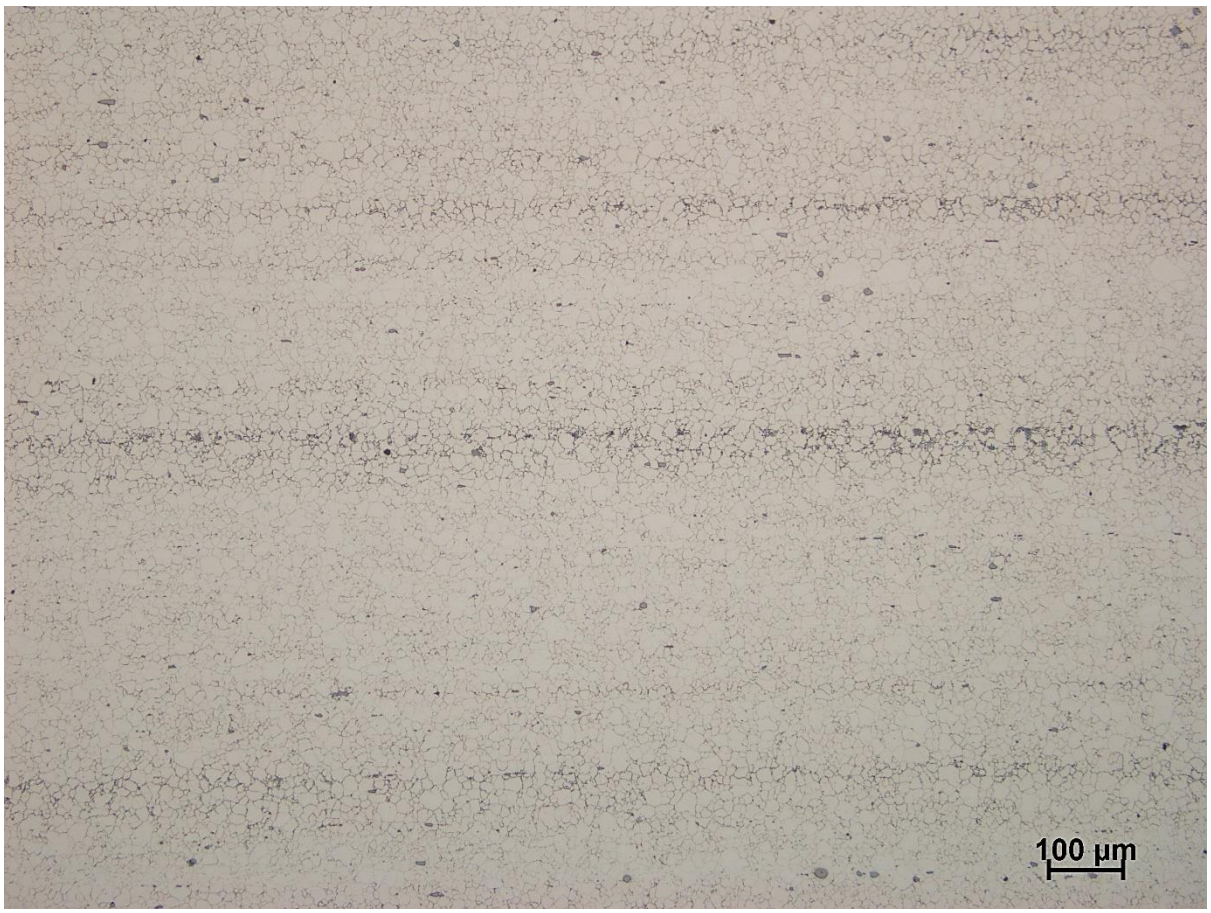

Figure 57 Microstructure of AZ61 in Longitudinal section at 100X magnification (obvious directionality of microstructure)

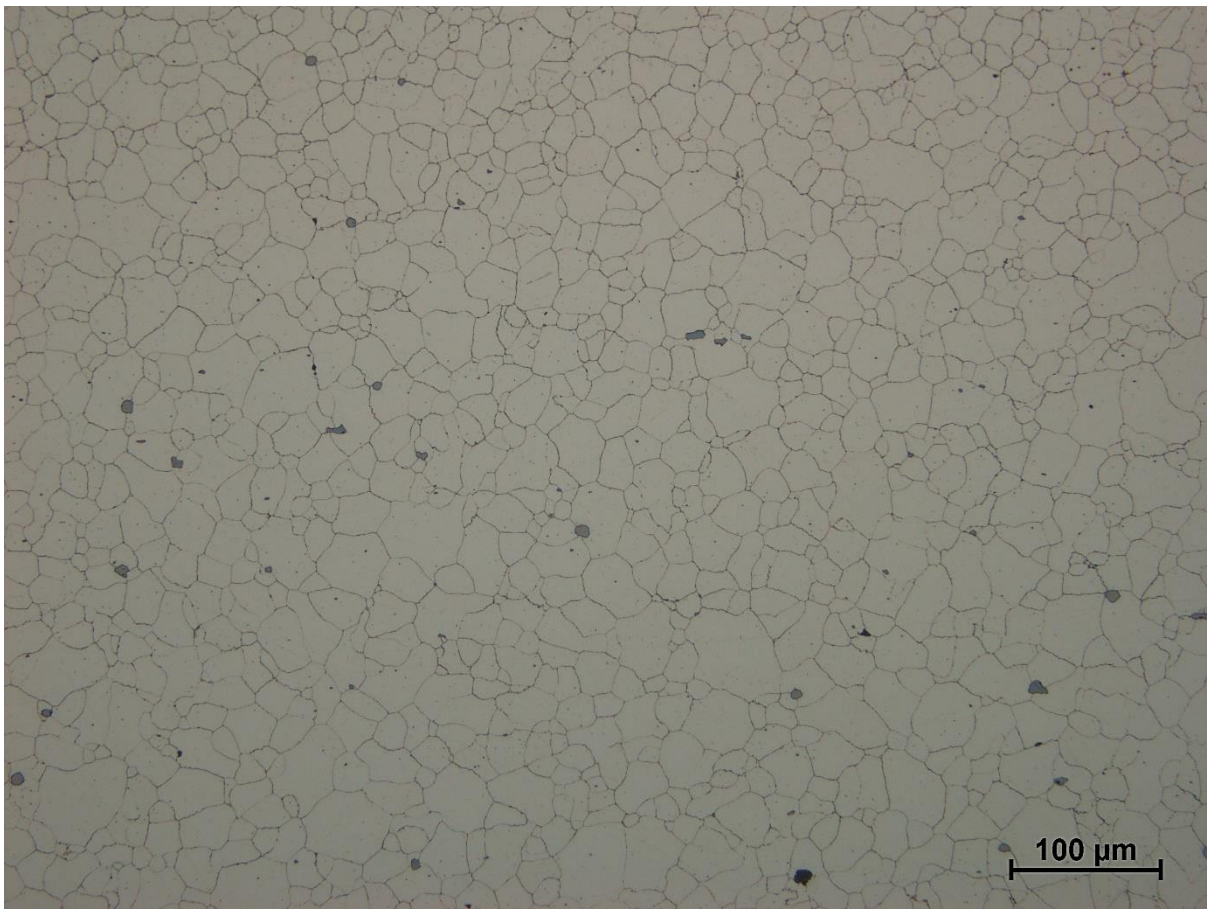

Figure 58 Microstructure of AZ61 in Longitudinal section at 200X magnification

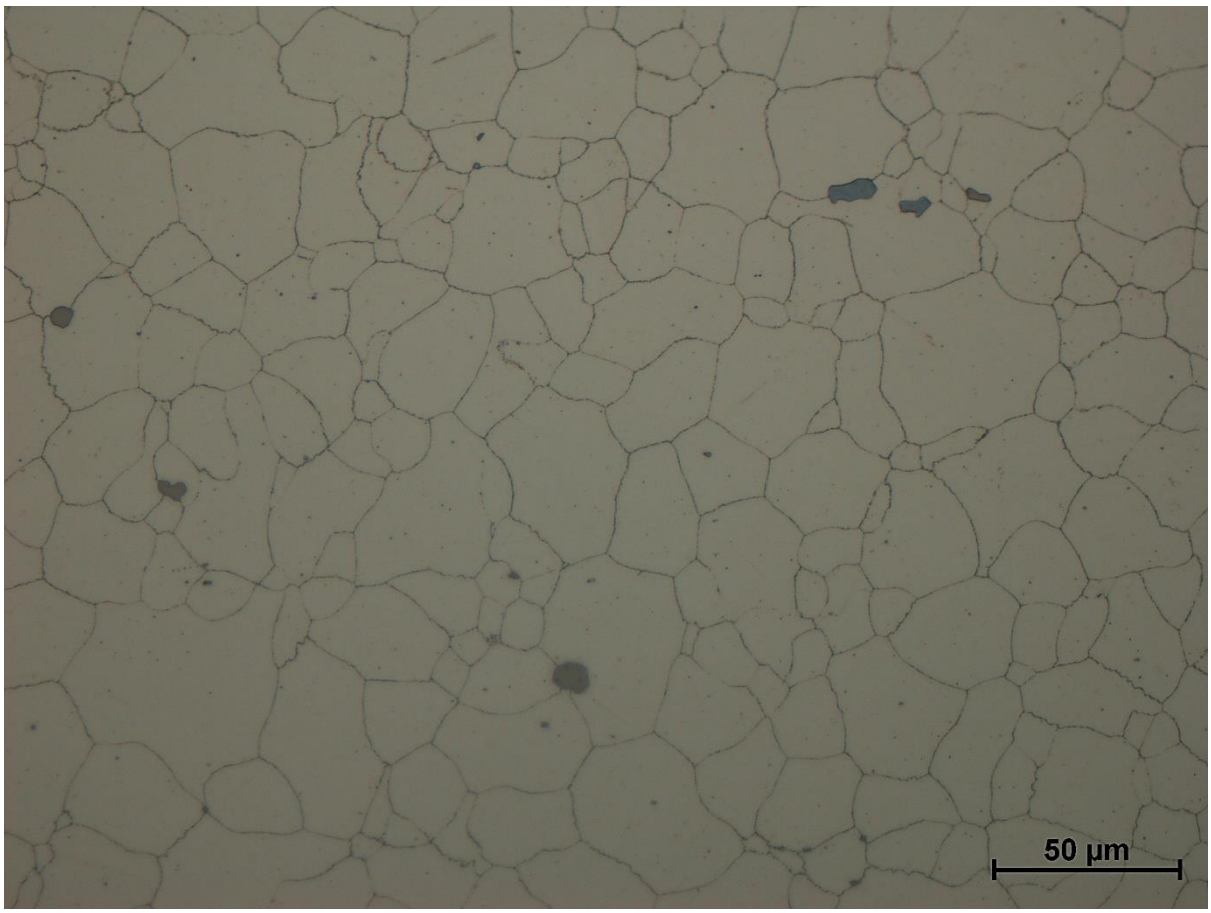

Figure 59 Microstructure of AZ61 in Longitudinal section at 500X magnification

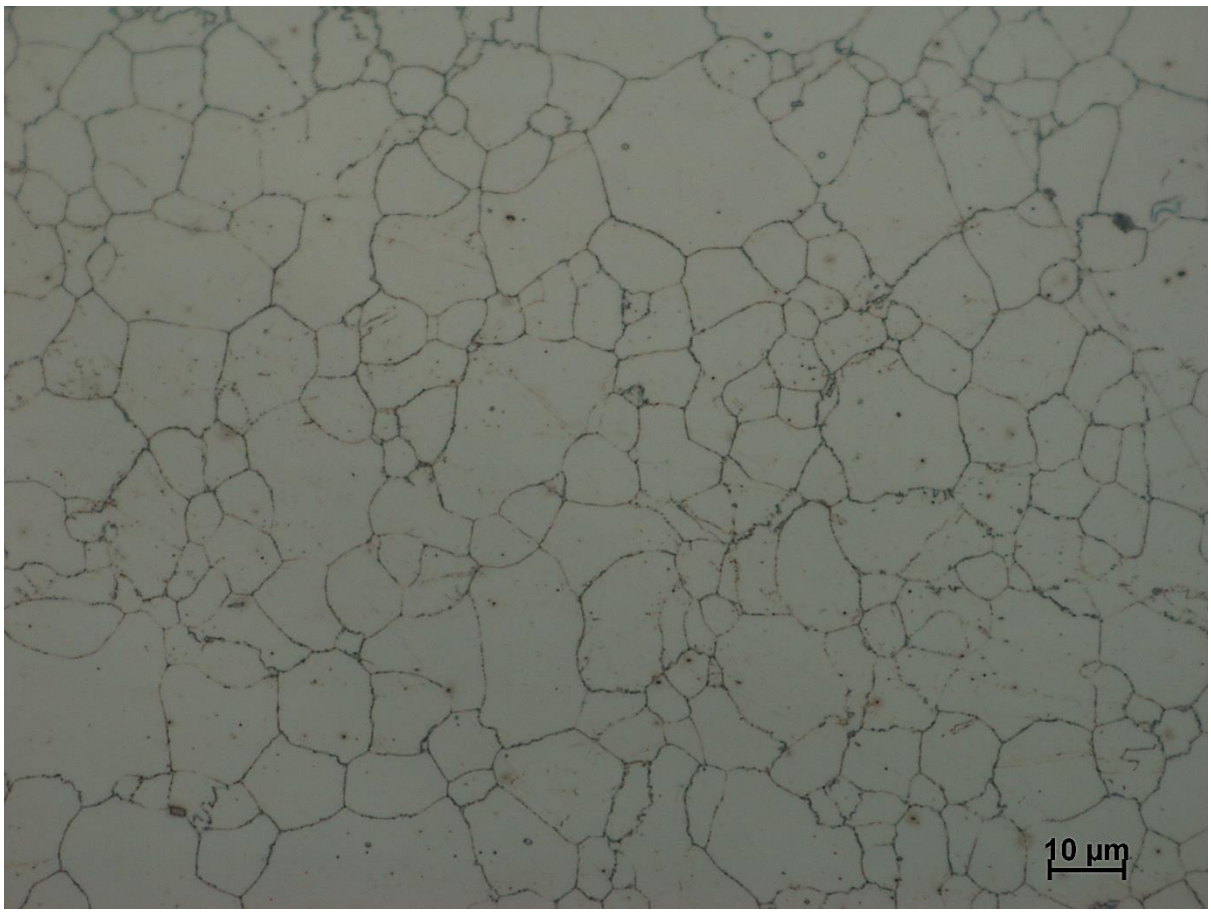

Figure 60 Microstructure of AZ61 in Longitudinal section at 1000X magnification

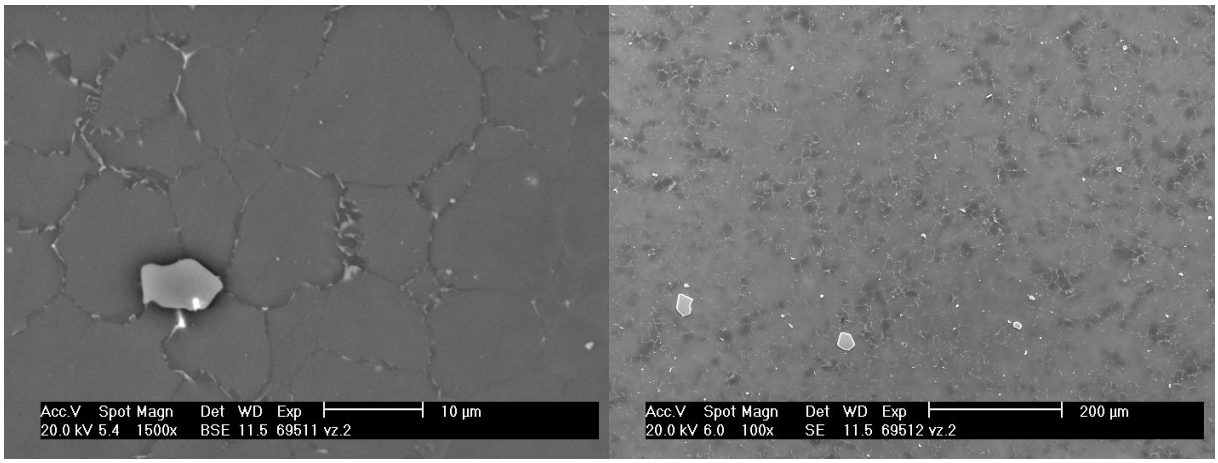

Figure 61 Microstructure of AZ61 in Transverse section SEM [54]

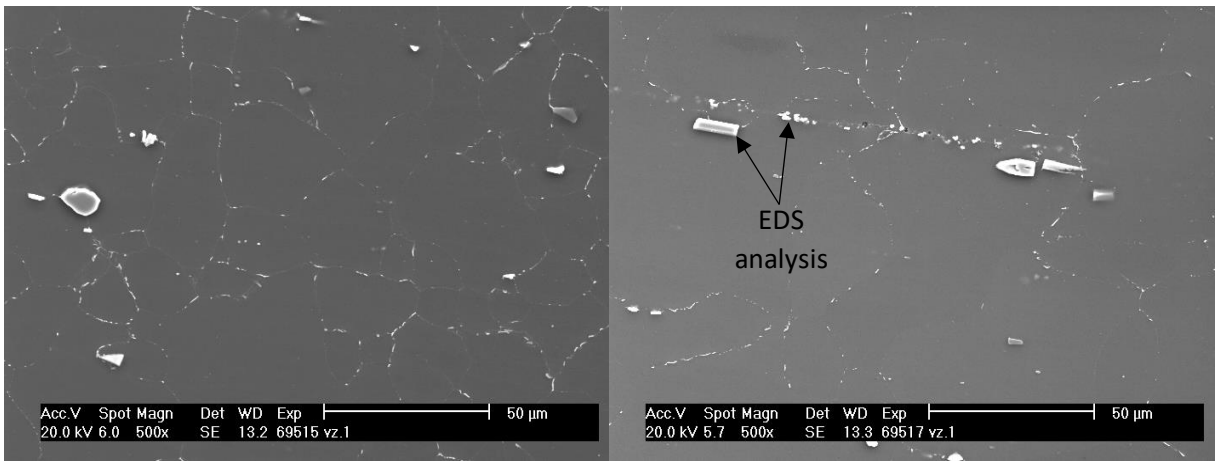

Figure 62 Microstructure of AZ61 in Longitudinal section SEM [54]

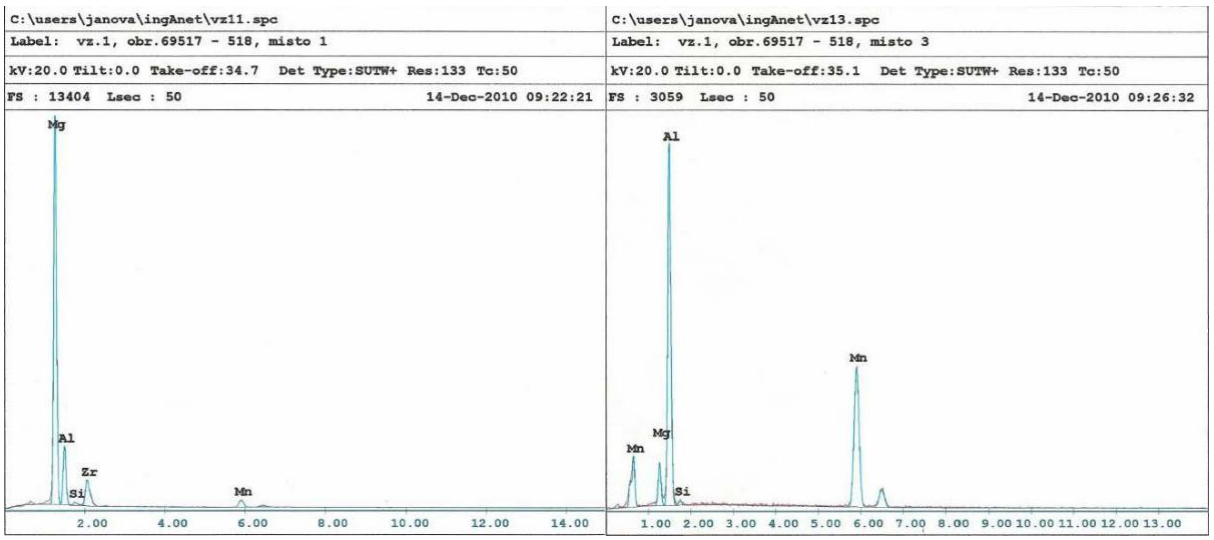

Figure 63 EDS analysis of precipitates [54]

6.2 Tensile and compressive testing

The experiment was carried out on the extruded AZ61 magnesium alloy, with following chemical composition:

Element [wt.%]	Al	Zn	Cu	Mn	Si	Fe	Ni	Sn	Pb	Zr	Ca
AZ61	6.1	0.61	0.00	0.27	0.00	0.004	0.00	0.00	0.00	0.00	0.000

Table 11 Table of chemical composition of tested material (extruded AZ61)

Compared to the chemical composition of AZ61 magnesium alloy according to the ASTM:

Element [wt.%]	Al	Zn	Mn	Si	Cu	Fe	Ni	Other
AZ61	5.8-7.2	0.04-1.5	0.15-0.5	max 0.1	max 0.05	max 0.005	max 0.005	max 0.3

Table 12 Chemical composition of AZ61 according to the ASTM

Tensile and compressive specimens were prepared from circular rod with original diameter $\emptyset = 22mm$, parallel to the extrusion direction. Tensile test specimen was machined according to DIN 50125 Form B with following dimensions: original diameter $d_0 = 6\,mm$, and original gauge length $L_0 = 35\,mm$ [Figure 61]

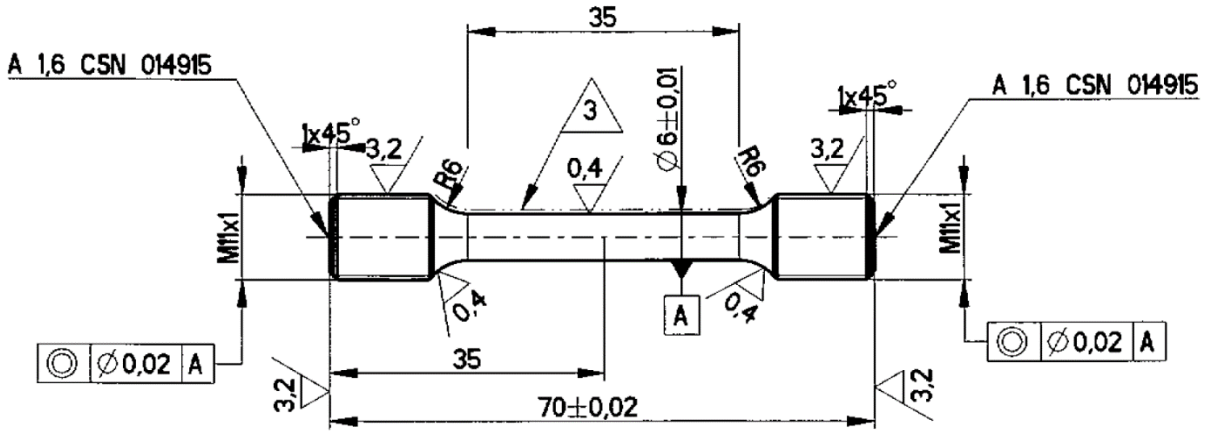

Figure 64 Drawing of prepared tensile test specimen [54]

And compressive test specimen was machined with these dimensions: original diameter $D_0 = 8\,mm$ and original height $H_0 = 12\,mm$. [Figure 62]

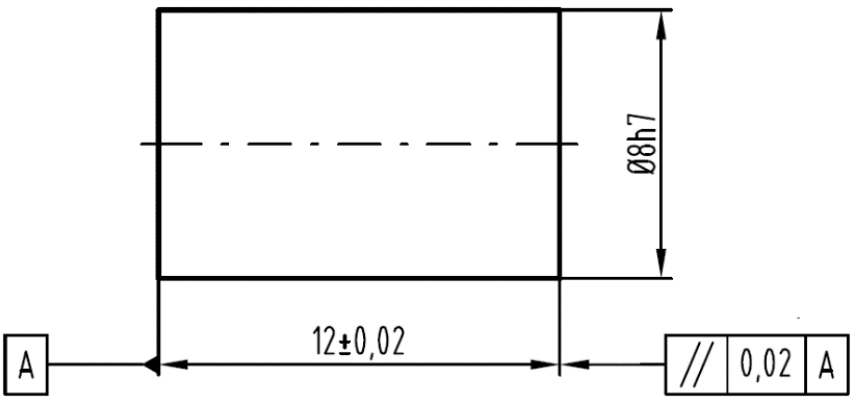

Figure 65 Drawing of compressive test specimen [54]

Tension and compression tests were then performed on universal electromechanical testing machine Zwick AllroundLine Z250 [Figure 63a], with up to 250kN of axial force, and universal servohydraulic testing machine Instron 8801 [Figure 63b], with up to 100kN of axial force.

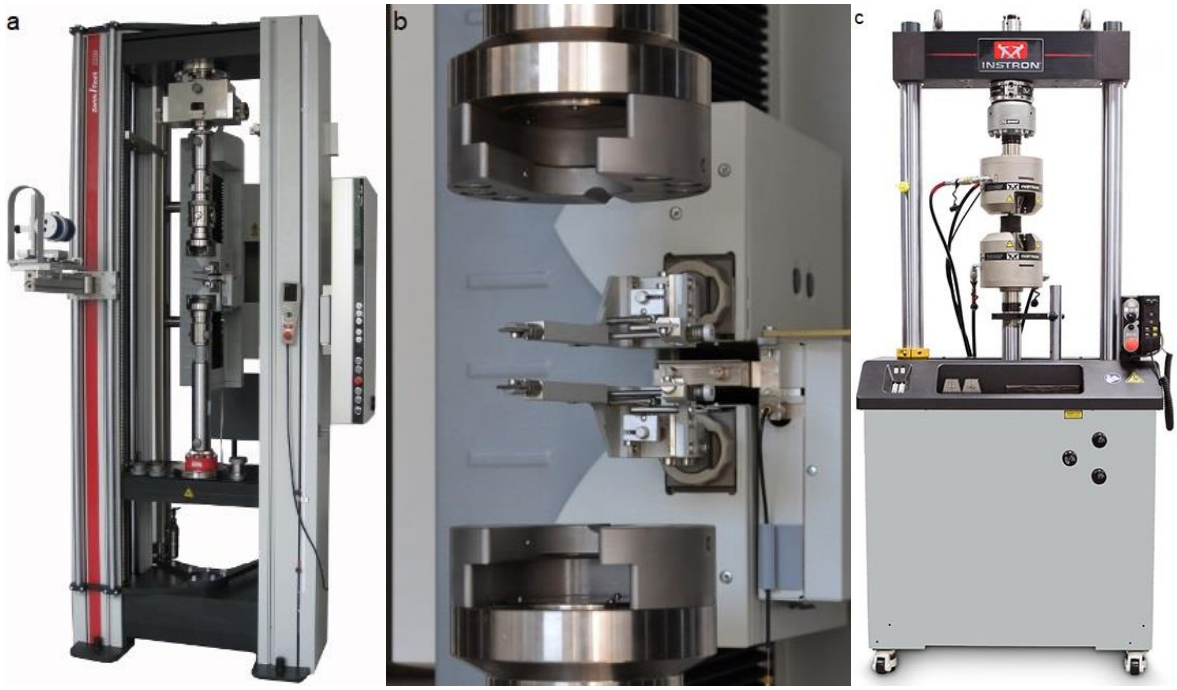

Figure 66 Universal testing machine Zwick AllroundLine Z250 (a, b) and universal testing machine Instron 8801 (c) [49, 50]

Obtained data on tensile and compressive responses of tested specimens were then recorded and marked in the stress-strain diagram [Figure 64].

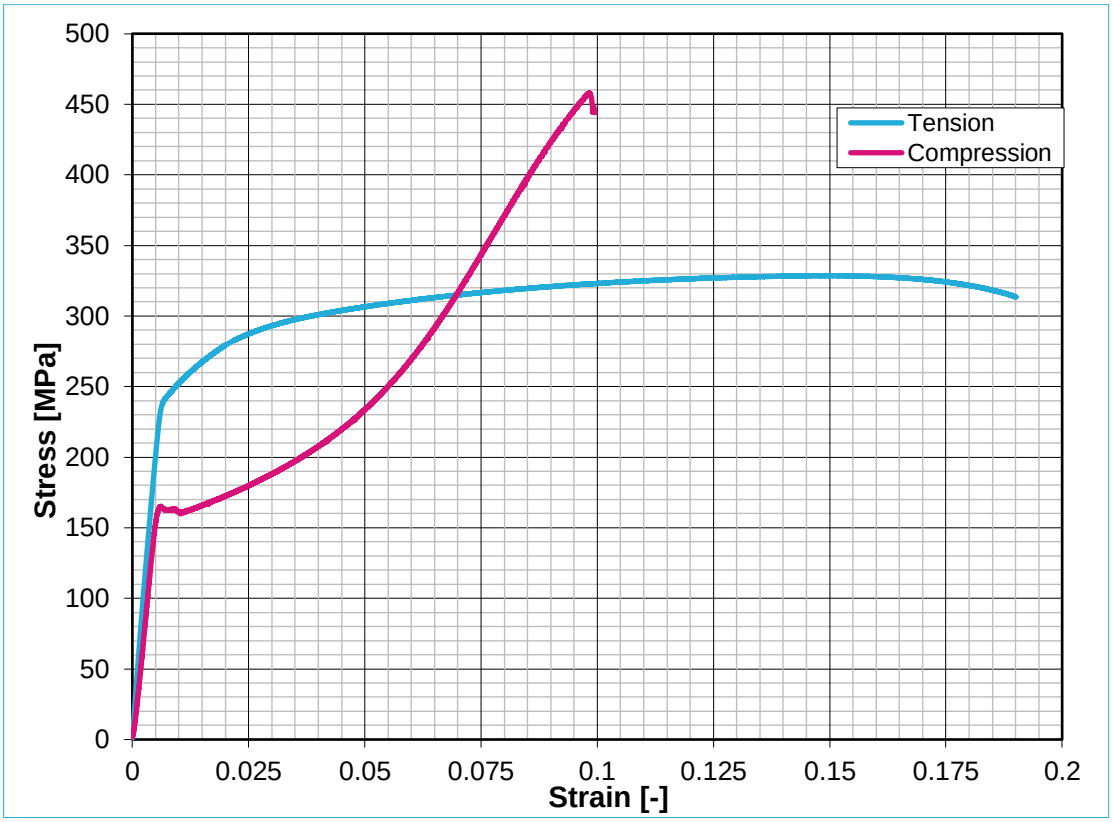

Figure 67 Stress-strain diagram of AZ61 magnesium alloy

Modulus of elasticity	E	44.82 GPa
Tensile yield stress	R_{et}	238 MPa
Offset yield stress	$R_{p0.2}$	255MPa
Ultimate tensile strength	R_m	341 MPa
Maximal force	F_m	9412.34 N
Fracture stress	R_f	302 MPa
Elongation at maximum force	A_g	13.1 %
Elongation	A	18.4 %
Reduction of area	Z	33.7 %

Table 13 Complex tensile properties

Compressive yield stress	R_{ec}	165 MPa
Offset yield stress	$R_{p0,2}$	164 MPa
Ultimate compressive strength	R_m	458 MPa
Maximal force	F_m	23020.08 N

Table 14 Complex compressive properties

The stress-strain diagram indicates the presence of rather significant tension-compression asymmetry, with CYS/TYS ratio being 0,69. This could be considered rather significant asymmetrical response. Values of yield stress in both tension and compression as well as the value of the asymmetry were marked in Table 15.

Tensile yield strength	238 MPa
Compressive yield strength	165 MPa
CYS/TYS	0.69

Table 15 Table listing tensile and compressive yield strength and tension-compression asymmetry

7 Discussion

- According to spectral analysis of AZ61 alloy, its chemical composition corresponds to the standardized chemical composition of AZ61 alloy according to ASTM.
- Metallographic analysis indicates that:
    - Bimodality of material was not detected.
    - Overall distribution of grain and precipitates confirm the extruded state of the alloy.
    - Grains do not indicate any directionality of the microstructure. No elongated or deformed grains were detected, probably due to dynamic recrystallization during the extrusion process.
    - Presence of MgMn and AlMn-based inclusions as well as intermetallic phase $Mg_{17}Al_{12}$, was detected. Their distribution on the grain boundaries in transverse section could be considered uniform. However, their distribution in longitudinal section is not uniform. Precipitates and inclusion form bands parallel to the extrusion direction (this can be typically observed in extruded materials)
    - At the edges of the metallographic sample courser grains were detected in contrast with the finer grain in the centre of the metallographic sample.
- Tension and compression tests confirmed the presence of the asymmetry. The extent of the asymmetry, or CYS/TYS equals to 0.69, which could be considered rather significant asymmetrical response to tensile and compressive loading.

The presence and the extent of the asymmetrical response to tensile and compressive testing of AZ61 is consistent with previously observed asymmetric behaviour of magnesium alloys from the theoretical part of this thesis. The asymmetrical response of this AZ61 could be attributed to the deformation twinning activated during deformation.

8 Conclusions

The first part of this thesis talked generally about tensile and compressive testing, analysis of various parameters of both test, specimens used for the testing, their standardized or non-standardized geometry and dimensions, and analysis of mechanical properties resulting from these tests.

The second part took a closer look at previously examined cases of tension-compression asymmetry of various magnesium alloys (AZ31, AZ61, AZ80, AM30 etc.), the main causes of the asymmetry in said alloys, possible quantifiability of the asymmetry using TCA parameter or CYS/TYS ratio, which determines the extent of the asymmetry in investigated alloy. Further it explored the possibility of lowering the extent of the asymmetry or even its complete elimination. From this we can determine several causes and parameters behind the occurrence of the tension-compression asymmetry in magnesium alloys:

- Tension-compression asymmetry has been shown to have strong dependence on load direction, demonstrated by the examination of various angles between load direction and extrusion axis. Further, the combined effect of load direction and grain size has been shown to have great effect on twinning in compression, and thus TCA as a whole.
- It has been suggested that not only grain size, but also precipitation of $Mg_{17}Al_{12}$ may have a similar effect on twinning process, and subsequently on TCA.
- It has been shown that multidirectional pre-compression can mitigate or even in some cases completely eliminate TCA.
- The occurrence of TCA can be in some specific case fairly sensitive to both strain rate and temperature for most of their combinations.
- Grain refinement using sever plastic deformation utilized in ECAP processing has proven to have an effect on tensile response of magnesium alloys, depending on the used method of processing (different ECAP routes).

The experimental part investigated tensile and compressive response of extruded AZ61 magnesium alloy, to determine presence of tension-compression yield asymmetry in this alloy. The presence of significant yield asymmetry was confirmed as can be seen in tensile and compressive stress-strain diagram. This asymmetrical response was then quantified using CYS/TYS ration or TCA parameter. Additionally, metallographic analysis of this alloy had for a task to determine grain size and crystal orientation, which could be further complemented by the EBSD, that would provide comprehensive map of crystal orientation. However due to unforeseen complication and current situation this was not accomplished. Nonetheless, metallographic analysis revealed slight directionality of microstructure, commonly observed in extruded materials, and variation of grain size between the edge and the centre of the sample.

References

[1] PTÁČEK, Luděk. *Nauka o materiálu II*. 2., opr. a rozš. vyd. Brno: CERM, c2002. ISBN 80-7204-248-3.

[2] AVEDESIAN, M., BAKER, H. ASM Speciality Handbook – Magnesium and magnesium alloys. Ohio, USA: ASM International, 1999. s. 314. ISBN 0871706571.

[3] ROUČKA, J. Metalurgie neželezných slitin. Brno: CERM, 2004. s. 148. ISBN 8021427906.

[4] DRÁPALA, Jaromír. *Hořčík, jeho slitiny a binární systémy hořčík – příměs = Magnesium, its alloys and Mg – admixture binary systems*. Ostrava: Vysoká škola báňská – Technická univerzita, 2004, s. 172. ISBN 80-248-0579-0.

[5] ISO 3116:2019: *Magnesium and magnesium alloys – Wrought magnesium and magnesium alloys*. 5th edition. Geneva: International Organization for Standardization, 2019.

[6] National Research Council. 1975. *Trends in Usage of Magnesium.* Washington, DC: The National Academies Press. https://doi.org/10.17226/21318.

[7] DJURDJEVIĆ, M. B., S. MANASIJEVIĆ, Z. ODANOVIĆ a N. DOLIĆ. *Calculation of Liquidus Temperature for Aluminum and Magnesium Alloys Applying Method of Equivalency*. Advances in Materials Science and Engineering [online]. Hindawi Publishing Corporation, 2013, (ID 170527), s. 8 [cit. 2020-06-14]. ISSN 1687-8442. Dostupné z: https://doi.org/10.1155/2013/170527

[8] MEZBAHUL-ISLAM, M., A. O. MOSTAFA a M. MEDRAJ. *Essential Magnesium Alloys Binary Phase Diagrams and Their Thermochemical Data.* Journal of Materials [online]. Hindawi Publishing Corporation, 2014, (ID 704283), 33s [cit. 2020-06-14]. Dostupné z: https://doi.org/10.1155/2014/704283

[9] HORYNOVÁ, M. *Únavové charakteristiky hořčíkové slitiny AZ31 po korozní degradaci* [online]. Brno, 2011 [cit. 2020-06-14]. Dostupné z: http://hdl.handle.net/11012/1974 . Diplomová práce. Vysoké učení technické v Brně. Fakulta strojního inženýrství. Ústav materiálových věd a inženýrství. Vedoucí práce Pavel Doležal.

[10] ROYLANCE, D. *Stress-Strain Curves* [online]. Department of Materials Science and Engineering, Massachusetts Institute of Technology, 2001, 14s [cit. 2020-06-14]. Dostupné z: http://web.mit.edu/course/3/3.11/www/modules/ss.pdf

[11] PTÁČEK, Luděk. *Nauka o materiálu I*. 2., opr. a rozš. vyd. Brno: CERM, c2003. ISBN 80-7204-283-1.

[12] *ČSN EN ISO 6892-1 Kovové materiály – Zkoušení tahem – Část 1: Zkušební metoda za pokojové teploty*. Praha: ÚNMZ, 2017.

[13] KUHN, H a D MEDLIN. ASM Handbook. Volume 8: Mechanical Testing and Evaluation. Materials Park, Ohio: ASM International, 2000, 8. ISBN 0871703890.

[14] KUMAR, KUNDAN, ARUN POOLEERY, K. MADHUSOODANAN, R.N SINGH, J K CHAKRAVARTTY, B K DUTTA a R.K. SINHA. Use of Miniature Tensile Specimen for Measurement of Mechanical Properties. *Procedia Engineering 86 (2014) 899 – 909* [online]. 2014, , 11 [cit. 2020-06-14]. Dostupné z: https://www.sciencedirect.com/science/article/pii/S1877705814020712

[15] KUMAR, kundan, arun POOLEERY, k. MADHUSOODANAN, R.N SINGH, Arnomitra CHATTERJEE, B.K. DUTTA a R.K. SINHA. Optimisation of thickness of miniature tensile specimens for evaluation of mechanical properties. *Materials Science & Engineering A 675 (2016) 32-43* [online]. 2016, , 12 [cit. 2020-06-14]. Dostupné z: https://www.sciencedirect.com/science/article/pii/S0921509316309455

[16] VELES, Pavol. *Mechanické vlastnosti a skúšanie kovov: celoštátna vysokoškolská učebnica pre hutnícke a strojárske fakulty vysokých škôl*. 2. vyd. Bratislava: Alfa, 1989. Edícia hutníckej literatúry.

[17] *ASTM E9 - 89a Standard Test Methods of Compression Testing of Metallic Materials at Room Temperature*. West Conshohocken PA: ASTM International, 2000.
[18] WRIGHT, R.N. Chapter 12 - Drawability and Breaks. *Wire Technology: Process Engineering and Metallurgy* [online]. 2016, **Second Edition**, 159-175 [cit. 2020-06-21]. Dostupné z: https://www.sciencedirect.com/science/article/pii/B9780128026502000121
[19] CHUA, C.K., C.H. WONG a W.Y. YEONG. Chapter Eight – Benchmarking for Additive Manufacturing. *Standards, Quality Control, and Measurement Sciences in 3D Printing and Additive Manufacturing* [online]. Singapore: Academic Press, 2017, , 181-212 [cit. 2020-06-21]. ISBN 978-0-12-813489-4. Dostupné z: https://www.sciencedirect.com/science/article/pii/B978012813489400088#s0050
[20] *Module 9 - Stability and Buckling* [online]. Massachusetts Institute of Technology, , 24 [cit. 2020-06-21]. Dostupné z: http://web.mit.edu/16.20/homepage/9_Buckling/Buckling_files/module_9_with_solutions.pdf
[21] LUBLINER, J. a P. PAPADOPOULOS. Elastic Stability and Buckling. *Introduction to Solid Mechanics* [online]. Springer, Cham, 2017, s. 441-471 [cit. 2020-06-21]. ISBN 978-3-319-18878-2. Dostupné z: https://doi.org/10.1007/978-3-319-18878-2_10
[22] MEGSON, T.H.G. Chapter 8 - Columns. *Introduction to Aircraft Structural Analysis (Third Edition)* [online]. 3dr edition. Butterworth-Heinemann, 2018, s. 269-310 [cit. 2020-06-22]. ISBN 978-0-08-102076-0. Dostupné z: https://www.sciencedirect.com/science/article/pii/B9780081020760000087
[23] KAŠUBA, Matúš. *Analýza výsledků zkoušek vykonaných na miniaturních zkušebních tělesech s různou geometrií* [online]. Brno, 2017 [cit. 2020-06-22]. Dostupné z: http://hdl.handle.net/11012/67726 Bakalářská práce. Vysoké učení technické v Brně. Fakulta strojního inženýrství. Ústav materiálových věd a inženýrství. Vedoucí práce Igor Moravčík.
[24] Young's Modulus of Elasticity. In: *Nuclear Power* [online]. [cit. 2020-06-22]. Dostupné z: https://www.nuclear-power.net/nuclear-engineering/materials-science/material-properties/strength/hookes-law/youngs-modulus-of-elasticity/
[25] FARIDMEHR, I., M.H. OSMAN, A.F. NEJAD, R. HODJATI a M. AZIMI. Correlation between Engineering Stress-Strain and True Stress-Strain Curve. *American Journal of Civil Engineering and Architecture* [online]. Science and Education Publishing, 2014, Vol. **2**(No. 1), s. 53-59 [cit. 2020-06-22]. Dostupné z: http://pubs.sciepub.com/ajcea/2/1/6/
[26] Compression Test on Mild Steel. In: *Virtual Labs* [online]. [cit. 2020-06-22]. Dostupné z: http://sm-nitk.vlabs.ac.in/exp15/index.html#
[27] KOSTRYZHEV, A.G. *Bauschinger effect in Nb and V microalloyed line pipe steels* [online]. Birmingham, 2009 [cit. 2020-06-22]. Dostupné z: https://core.ac.uk/download/pdf/40041921.pdf Dissertation. The University of Birmingham.
[28] JORDON, J.B., M.F. HORSTEMEYER, K. SOLANKI a Y. XUE. Damage and stress state influence on the Bauschinger effect in aluminum alloys. *Mechanics and Materials* [online]. October 2007, Volume **39**(Issue 10), s. 920-931 [cit. 2020-06-22]. ISSN 0167-6636. Dostupné z: https://www.sciencedirect.com/science/article/pii/S0167663607000579
[29] SONG, L., B. WU, L. ZHANG, X. DU, Y. WANG, C. ESLING a M.J. PHILIPPE. Detwinning-related Bauschinger effect of an extruded magnesium alloy AZ31B. *Materials Characterization* [online]. February 2019, Volume **148**, s. 63-70 [cit. 2020-06-22]. ISSN 1044-5803. Dostupné z: https://www.sciencedirect.com/science/article/pii/S1044580318325038

[30] Kassner, M.E., Geantil, P., Levine, L.E., Larson, B.C., 2008. Backstress, the Bauschinger Effect and Cyclic Deformation. Materials Science Forum Volume 604–605, s. 39–51. https://doi.org/10.4028/www.scientific.net/msf.604-605.39
[31] BROWN, L.M. *Orowan's explanation of the Bauschinger effect* [online]. February 1977, Volume **11**(Issue 2), s. 127-131 [cit. 2020-06-22]. ISSN 0036-9748. Dostupné z: https://www.sciencedirect.com/science/article/abs/pii/0036974877902915
[32] HOLAS, Jiří. *Bauschingerův efekt a cyklická plasticita u konstrukčních slitin hořčíku* [online]. Brno, 2012 [cit. 2020-06-22]. Dostupné z: http://hdl.handle.net/11012/16587 Bakalářská práce. Vysoké učení technické v Brně. Fakulta strojního inženýrství. Ústav materiálových věd a inženýrství. Vedoucí práce Josef Zapletal.
[33] Damage and stress state influence on the Bauschinger effect in aluminum alloys: A stress–strain curve that exhibits the Bauschinger effect for typical metallic alloys. In: *ICME* [online]. [cit. 2020-06-23]. Dostupné z: https://icme.hpc.msstate.edu/mediawiki/index.php/File:Bauschinger_effect_Stress-Strain_curve.jpg
[34] YIN, D.L., J.T. WANG, J.Q. LIU a X. ZHAO. On tension–compression yield asymmetry in an extruded Mg–3Al–1Zn alloy. *Journal of Alloys and Compounds* [online]. June 2009, Volume **478**(Issue 1-2), s. 789-795 [cit. 2020-06-23]. ISSN 0925-8388. Dostupné z: https://www.sciencedirect.com/science/article/pii/S0925838808022056
[35] Mechanical anisotropy of extruded Mg–6% Al–1% Zn alloy. *Materials Science and Engineering: A* [online]. August 2004, Volume **379**(Issue 1-2), s. 258-263 [cit. 2020-06-23]. ISSN 0921-5093. Dostupné z: https://www.sciencedirect.com/science/article/pii/S0921509304001893
[36] BARNET, M.R., Z. KESHAVARZ a X. MA. A Semianalytical Sachs Model for the Flow Stress of a Magnesium Alloy. *METALLURGICAL AND MATERIALS TRANSACTIONS A* [online]. July 2006, Volume **37A**, s. 2284-2293 [cit. 2020-06-23]. Dostupné z: https://link.springer.com/content/pdf/10.1007/BF02586147.pdf
[37] WANG, J.T., D.L. YIN, J.Q. LIU, Y.L. SU a X. ZHAO. Effect of grain size on mechanical property of Mg–3Al–1Zn alloy. *Scripta Materialia* [online]. July 2008, Volume **59**(Issue 1), s. 63-66 [cit. 2020-06-23]. ISSN 1359-6462. Dostupné z: https://www.sciencedirect.com/science/article/pii/S1359646208001565
[38] BROWN, D.W., S.R. AGNEW, T.M. HOLDEN, S.C. VOGEL a C.N. TOME. Internal strain and texture evolution during deformation twinning in magnesium. *Materials Science and Engineering: A* [online]. June 2005, Volume **399**(Issue 1-2), s. 1-12 [cit. 2020-06-23]. ISSN 0921-5093. Dostupné z: https://www.sciencedirect.com/science/article/pii/S0921509305001541
[39] LETZIG, D., J. SWIOSTEK, J. BOHLEN, P.A. BEAVEN a K.U. KAINER. *Wrought magnesium alloys for structural applications* [online]. 2008, Volume 24 (Issue 8), s. 991-996 [cit. 2020-06-23]. ISSN 1743-2847. Dostupné z: https://doi.org/10.1179/174328407X213080
[40] XU, S., T. LIU, H. CHEN, Z. MIAO, Z. ZHANG a W. ZENG. Reducing the tension–compression yield asymmetry in a hot-rolled Mg–3Al–1Zn alloy via multidirectional pre-compression. *Materials Science and Engineering: A* [online]. March 2013, Volume **565**(Issue 10), s. 96-101 [cit. 2020-06-23]. ISSN 0921-5093. Dostupné z: https://www.sciencedirect.com/science/article/pii/S0921509312017182
[41] ZACHARIAH, Z., S.S.V. TATIPARTI, S.K. MISHRA, N. RAMAKRISHNAN a U. RAMAMURTY. Tension–compression asymmetry in an extruded Mg alloy AM30: Temperature and strain rate effects. *Materials Science and Engineering: A* [online]. June 2013, Volume **572**(Issue 10), s. 8-18 [cit. 2020-06-23]. ISSN 0921-5093. Dostupné z: https://www.sciencedirect.com/science/article/pii/S092150931300169X

[42] KORLA, R. a A.H. CHOKSHI. Strain-rate sensitivity and microstructural evolution in a Mg–Al–Zn alloy. *Scripta Materialia* [online]. November 2010, Volume **63**(Issue 9), s. 913-916 [cit. 2020-06-23]. ISSN 1359-6462. Dostupné z: https://www.sciencedirect.com/science/article/pii/S1359646210004550
[43] TONG, L.B., M.Y. ZHENG, X.S. HU, K. WU, S. KAMADO a Y. KOJIMA. Influence of ECAP routes on microstructure and mechanical properties of Mg–Zn–Ca alloy. *Materials Science and Engineering: A* [online]. June 2010, Volume **527** (Issues 16-17), s. 4250-4256 [cit. 2020-06-23]. ISSN 0921-5093. Dostupné z: https://www.sciencedirect.com/science/article/pii/S0921509310003369
[44] IWAHASHI, Y., J. WANG, Z. HORITA, M. NEMOTO a T.G. LANGDON. Principle of equal-channel angular pressing for the processing of ultra-fine grained materials. *Scripta Materialia* [online]. July 1996, **35**(2), s. 143-146 [cit. 2020-06-23]. ISSN 1359-6462. Dostupné z: https://www.sciencedirect.com/science/article/pii/1359646296001078
[45] NAKASHIMA, K., Z. HORITA, M. NEMOTO a T.G. LANGDON. Development of a multi-pass facility for equal-channel angular pressing to high total strains. *Materials Science and Engineering: A* [online]. April 2000, Volume **281**(Issues 1-2), s. 82-87 [cit. 2020-06-23]. ISSN 0921-5093. Dostupné z: https://www.sciencedirect.com/science/article/pii/S0921509399007443
[46] JONÁK, Martin. *Metody přípravy jemnozrnných materiálů (ECAP)* [online]. Brno, 2008 [cit. 2020-06-23]. Dostupné z: http://hdl.handle.net/11012/2578. Bakalářská práce. Vysoké učení technické v Brně. Fakulta strojního inženýrství. Ústav materiálových věd a inženýrství. Vedoucí práce Libor Pantělejev.
[47] ČAPEK, J., M. KNAPEK, J. DITTRICH a K. MÁTHIS. Characterization of Deformation Mechanisms in Mg Alloys by Advanced Acoustic Emission Methods. *Metals - Open Access Metallurgy Journal* [online]. August 2018, **8**(8) [cit. 2020-06-23]. ISSN 2075-4701. Dostupné z: https://www.researchgate.net/publication/327066032_Characterization_of_Deformation_Mechanisms_in_Mg_Alloys_by_Advanced_Acoustic_Emission_Methods
[48] BALL, E.A. a P.B. PRANGNELL. Tensile-compressive yield asymmetries in high strength wrought magnesium alloys. *Scripta Metallurgica et Materialia* [online]. July 1994, Volume **31**(Issue 2), s. 111-116 [cit. 2020-06-23]. ISSN 0956-716X. Dostupné z: https://www.sciencedirect.com/science/article/pii/0956716X94901597
[49] Když se řekne ZWICK. FSInfo [online]. Brno: FSI VUT Brno, 2013 [cit. 2020-06-24]. Dostupné z: http://fsinfo.fme.vutbr.cz/index.php/casopis/fsi-zive/45-kdyz-se-reknezwick
[50] 8801 (100kN) Fatigue Testing Systems. INSTRON [online]. Norwood: Illinois Tool Works, 2017 [cit. 2020-06-24]. Dostupné z: http://www.instron.us/enus/products/testing-systems/dynamic-and-fatigue-systems/servohydraulicfatigue/8801-floor-model
[51] OPAL X-Press 2. In: *QATM* [online]. [cit. 2020-06-24]. Dostupné z: https://www.qatm.com/products/hot-mounting-presses/benchtop/opal-x-press/function-features/
[52] Struers Pedemin. In: *Gemini Lab* [online]. [cit. 2020-06-24]. Dostupné z: https://www.geminibv.com/labware/struers-pedemin-dap-7-grinding-and-polishing-machine/
[53] Struers grinding and polishing consumables. In: *Struers e-shop* [online]. [cit. 2020-06-24]. Dostupné z: https://www.struers.com/en/Products/Grinding-and-Polishing/Grinding-and-polishing-consumables#
[54] Data and documentation provided directly by the supervisor Ing. Jozef Zapletal Ph.D.

Symbols and Abbreviations

ρ	[kg/m^3]	Density
T	[°C, K]	Temperature
w_i	[wt.%]	Mass Fraction
R_{ms}	[MPa]	Shear Strength
K	[J]	Notch Toughness
E	[GPa]	Modulus of Elasticity
F	[N]	Force
L	[M]	Elongation/ Length
S_0	[m^2]	Original Cross-Section of a Testing Specimen
S_u	[m^2]	Minimal Cross-Section After Fracture
L_0	[m]	Original Gauge Length of a Testing Specimen
L_u	[m]	Final Gauge Length After Fracture
d_0	[m]	Original Diameter
R_u	[MPa]	Proportionality Limit
R_E	[MPa]	Elasticity Limit
R_e	[MPa]	Yield Strength
R_m	[MPa]	Ultimate Tensile Strength
R_{Pd}	[MPa]	Ultimate Compressive Strength
R_f	[MPa]	Fracture Strength
$R_{p0.2}$	[MPa]	Offset Yield Strength
ε_{pl}	[-]	Plastic Deformation
ε_{el}	[-]	Elastic Deformation
ε_c	[-]	Complete Deformation
R_{eH}	[MPa]	Upper Yield Point
R_{eL}	[MPa]	Lower Yield Point
F_{max}	[N]	Maximal Force Applied
A	[%]	Elongation
Z	[%]	Reduction of Area
$\dot{\varepsilon}$	[s^{-1}]	Strain Rate
$\dot{\varepsilon_s}$	[s^{-1}]	True Strain Rate
σ	[MPa]	Stress
K	[-]	Strengthening Coefficient (Material Constant)
$\bar{\varepsilon}$	[-]	Strain
n	[-]	Strain Hardening Exponent
h	[-]	Degree of Strain Hardening
k	[-]	Coefficient of Proportionality
ε_N	[-]	Equivalent strain

CYS	Compression Yield Stress
TYS	Tension Yield Stress
TCA	Tension-Compression Asymmetry
CYS/TYS	Extent of the Tension-Compression Asymmetry
HCP	Hexagonal Closely Packed
AZ31	Magnesium Alloy (3% Al, 1% Zn)
Z61	Magnesium Alloy (6% Al, 1% Zn)
AZ80	Magnesium Alloy (8% Al, up to 1% Zn)
ZK60	Magnesium Alloy (6% Zn, up to 1% Zr)
CSN	Česká Technická Norma (Czech Technical Standards)
ISO	International Organization for Standardization

ASTM	American Society for Testing and Materials
MP	Multidirectional pre-compression
MPA	Multidirectional pre-compression and anneal
RD	Rolling direction
TD	Transverse direction
ND	Normal direction
ED	Extrusion direction
ECAP	Equal channel angular pressing
EBSD	Electron backscatter diffraction